Doctoral Thesis

Study on Hematite Photoanodes for Photoelectrochemical Water Splitting

Dewangga Oky Bagus Apriandanu

2020DAA03

Department of Chemical and Environmental Engineering

Graduate School of Environmental Engineering

The University of Kitakyushu

2023

Abstract

Photoelectrochemical (PEC) water splitting is a strategy to decompose water into oxygen and hydrogen molecules with the utilization of light energy and semiconductor photoelectrodes. Hematite (α-Fe_2O_3) is a potential photoanode candidate for PEC water splitting owing to its inexpensive, high abundance in nature, and suitable band gap (~2.1 eV) under visible light irradiation. However, Fe_2O_3 still suffers from low PEC efficiency, mainly due to poor electrical conductivity and limited light absorption.

This thesis proposes methods for developing hematite photoanodes with improved PEC performance for water splitting. Firstly, additional annealing in argon atmosphere is employed to enhance the photocurrent response of the hematite photoanodes. Secondly, a macroporous conductive substrate with large surface areas is selected for fabricating hematite photoelectrodes. Finally, the porous hematite photoanode is developed as a membrane electrode assembly (MEA) for PEC water splitting in two-compartment cells.

Chapter 1 presents a general introduction to solar water splitting, semiconductor electrodes, and a brief overview of hematite photoanodes.

In Chapter 2, Ti^{4+}-doped Fe_2O_3 electrodes were prepared by hydrothermal treatment followed by annealing at 873 K in air and a second round of annealing at 473 K in argon. The two-step annealing process increased the PEC performance of Ti-doped Fe_2O_3 on a fluorine-doped tin oxide (FTO)-coated glass substrate (FTO/Ti-Fe_2O_3) for water oxidation in 0.1 mol L^{-1} NaOH solution. Ti^{4+} doping was achieved by using $TiCl_4$ ethanol solutions of various concentrations. The optimized Ti/Fe atomic ratio in the solution was 3%, which showed the highest photocurrent densities. The two-step annealed FTO/Ti-Fe_2O_3 generated a photocurrent density of 0.55 mA cm^{-2} at 1.50 V vs. reversible hydrogen electrode under simulated one-sun illumination, which was approximately three times higher than that of the photoanodes

annealed only in air. Four-point probe resistivity measurements revealed that the two-step annealing resulted in a higher electrical conductivity than that of the air-annealed samples. The conductivity improvements induced by the additional argon annealing at 473 K were ascribed to the increased donor density, which was confirmed by Mott–Schottky analysis and diffuse reflectance UV-visible–near-infrared spectra. The strategy of Ti^{4+} doping and two-step annealing successfully fabricated Fe_2O_3-based photoanodes with better photocurrent density due to high electrical conductivity.

In Chapter 3, three-dimensional (3D) titanium microfiber felt (Ti felt) was used as a conductive substrate. Compared to conventional two-dimensional (2D) substrates, such as FTO-coated glass and Ti sheets, the loading amount of Ti-doped Fe_2O_3 on Ti felt was 2–5 times higher in a similar substrate geometric area. However, the thickness of the Ti-doped Fe_2O_3 layer on Ti felt (0.6 μm) was less than that on the 2D substrates. The Ti-felt/Ti-Fe_2O_3 exhibits a higher photocurrent density than FTO/Ti-Fe_2O_3 and Ti-sheet/Ti-Fe_2O_3. Analyses of the incident photon-to-current conversion efficiency (IPCE) and Faradaic efficiency indicated that Ti-felt/Ti-Fe_2O_3 showed higher PEC activity for the oxygen evolution reaction than FTO/Ti-Fe_2O_3. The enhanced PEC activity is ascribed to the moderate thickness of the Fe_2O_3 layer, which contributes to a short electron transport distance. Furthermore, the high loading of Fe_2O_3 on Ti-felt substrate increased the photocurrent response at wavelengths near the band edge, even at low light intensities. This study provides new insights for preparing hematite photoanodes with higher PEC activity using a 3D porous substrate, rather than conventional 2D substrates.

Chapter 4 represents the successful fabrication of an MEA that incorporates the porous Fe_2O_3 photoanode integrated with an anion exchange membrane (AEM). The AEM-PEC system demonstrates water splitting under visible light irradiation, operating even under low-conductivity and near-neutral conditions (~1 mS/m and pH ~9), without the need for supporting electrolytes. The IPCE action spectrum confirms visible light responses extending up to 600

nm, surpassing that of previous reports on porous photoelectrodes with solid electrolyte membranes. Importantly, this AEM-PEC system differs from conventional PEC using liquid electrolytes, where hematite photoanodes are active only in strongly alkaline solutions. The combination of porous photoelectrodes and solid electrolyte membranes is significant for water-splitting reactions without the reliance on electrolyte solutions.

In summary (Chapter 5), this thesis explored alternative strategies for enhancing the PEC efficiency of hematite photoanodes. Additional annealing in an argon atmosphere improves the PEC properties by simultaneously increasing donor density and electrical conductivity. Furthermore, the use of 3D macroporous conductive substrates enables higher loading and thinner thickness of the hematite layer, resulting in enhanced PEC efficiency. Additionally, the AEM-PEC system achieves water splitting in pure water without supporting electrolytes, overcoming mass-transport limitations through the synergistic combination of a porous photoanode and a solid electrolyte membrane. This low-cost and straightforward device integration of porous hematite photoanodes with AEM exhibits promising potential for advancing sustainable energy production through PEC applications.

.

Contents

Contents

Contents

Contents

Contents

Contents

Chapter 1. General Introduction

1.1 Solar water splitting

The increased demand for clean energy has been the most challenging concern since the depletion of fossil fuels led to the alteration of climate and ecosystems worldwide. The discoveries of alternative renewable energy sources, such as solar, wind, hydropower, and geothermal, must be universally applied as a strategy for saving energy through the advancement of technology. Among them, sunlight is one of the inexhaustible energy sources with available solar power at the Earth's surface equal to 130 million 500 MW plant.[1] To date, solar energy is still one of the promising energy sources subjected to advanced renewable technology to provide clean and carbon-free sources since there is a limitation on the use of other renewable energy sources, for instance, water or hydropower. The utilization of harvested solar energy has attracted considerable attention as an alternative strategy to address the energy issue by producing oxygen and hydrogen through photoelectrochemical (PEC) water splitting.[2,3]

PEC water splitting was first introduced by Fujishima and Honda in 1972 by utilizing TiO_2 photoanode irradiated by UV light.[4] Since then, tremendous efforts have been made to design efficient and low-cost PEC water splitting reactions for practical applications. In conventional systems, PEC cells are designed in the configuration of the three-electrode cell by employing photoactive materials as working electrodes, reference electrodes, and counter electrodes, which are immersed in electrolyte solutions under light irradiation and associated with the external circuit. Specifically, the reaction of oxidation (O_2 evolution) takes place in the anode, while reduction (H_2 evolution) occurs in the cathode, as shown in Figure 1. To promote the formation of H_2 and $½O_2$ from water splitting reaction, the standard free energy ($\Delta G°$) is required as 237.2 kJ mol^{-1}, which is equal to the electrolysis cell voltage ($\Delta E°$) of 1.23 V for

one electron transfer according to the Nernst equation. In general, water splitting reactions operate under acidic or alkaline conditions, depending on the nature of the photoelectrode, for instance, the stability properties used when immersing in the electrolyte solution. In a PEC cell under acidic medium, the oxygen evolution reaction (OER) and hydrogen evolution reaction (HER) are given, as follows.

Cathode: $2H^+ + 2e^- \longrightarrow H_2$ (1.1)

Anode : $2H_2O \longrightarrow O_2 + 4H^+ + 4e^-$ (1.2)

In the case of alkaline conditions, the hydroxyl species are involved in the reactions of reduction and oxidation, which can be expressed in the following reactions;

Cathode: $2H_2O + 2e^- \longrightarrow H_2 + 2OH^-$ (1.3)

Anode : $4OH^- \longrightarrow O_2 + 2H_2O + 4e^-$ (1.4)

Therefore, the overall reaction for PEC water splitting is written as follows;

$2H_2O \longrightarrow 2H_2 + O_2, \Delta E°$=1.23 V (1.5)

According to both reactions under acidic or alkaline media, two electrons are required to generate H_2 molecules as hydrogen evolution reaction (HER) in the cathode part, while, four electrons are required to oxidize water to form O_2 molecules as oxygen evolution reaction (OER) in the anode part.

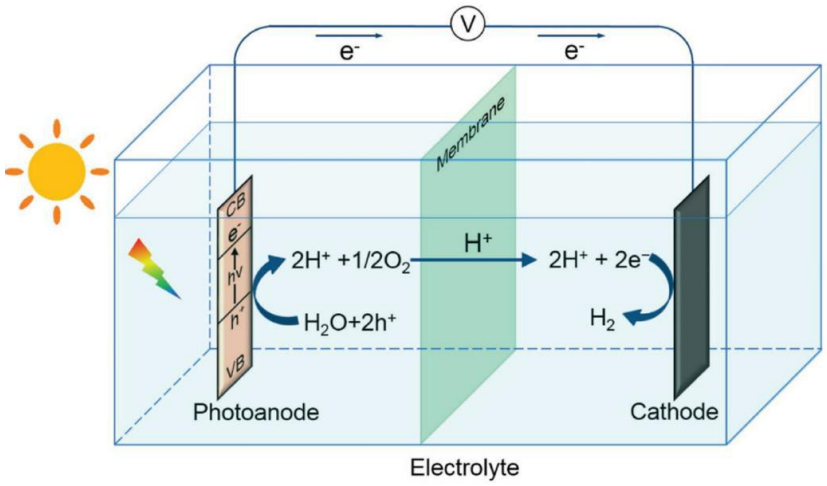

Figure 1.1: Schematic of PEC cell with an n-type semiconductor photoanode and metallic cathode for basic water splitting reaction. Reproduced under Creative Commons Attribution License CC BY[5]. Willey's Open Access.

1.2 Semiconductor electrode

Among other semiconductors, metal oxides show advantages such as low-cost and earth-abundance materials. Importantly, their appropriate band gap energy is still relatively in the range of UV and visible spectrum required for PEC water splitting reaction. As described previously, a photoelectrode should provide a minimum energy of 1.23 V per electron from absorbing the photon to split water. Band gap is the first parameter to determine the ability of semiconductor electrodes to harvest light. For this reason, semiconductor materials need to have a suitable band gap energy required to promote a water splitting reaction. Therefore, semiconductors should be responsible for absorbing light with energy larger than their band gap energy. Semiconductors with narrow band gap energy can harvest visible light, which is a large part of solar light energy. Murphy and coworkers studied that the optimum band gap energy for ideal semiconductors is in the range of 1.9 and 2.4 eV.[6] Therefore, it is important to employ the narrow band gap semiconductor as photoelectrodes in the PEC water splitting applications.

The second parameter for semiconductor electrodes is their band edge positions. Typically, the top level of the valence band (VB) should be more positive than the oxidation potential of O_2/H_2O, so the holes can be transferred from the photoelectrode to the solution to oxidize water molecules. In a similar way, to induce the reduction reaction, the bottom level of the conduction band (CB) should be more negative than the reduction potential of H^+/H_2.[3]

Thirdly, the semiconductor must be categorized into inexpensive materials and has a high abundance in nature considering the sustainability in the practical implementation in the future. Lastly, the stability of semiconductor electrodes in extremely acidic or alkaline environments

is another requirement, which should be considered regarding the used electrolyte solutions. Generally, this condition is attributed to the corrosion property or the performance degradation of the semiconductor electrode that can perturb their efficiency for PEC water splitting. Thus, it is essential to consider the choice of semiconductor electrodes concerning their physical and chemical properties in PEC application.

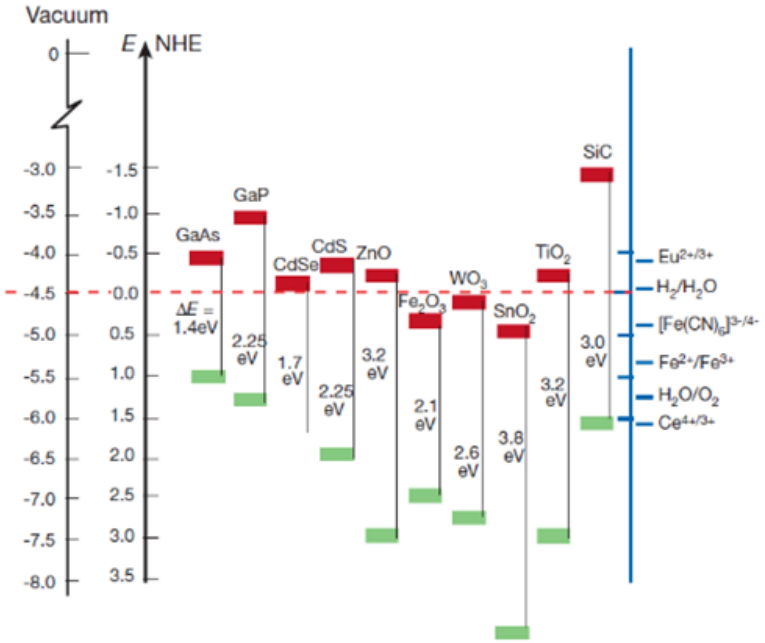

Figure 1.2: Band gap values for various semiconductor electrodes at pH 1. Red and green colors indicate the bottom level of CB and the top level of VB, respectively. The energy scale is in electron volts using the normal hydrogen electrode (NHE) or the vacuum level as a reference. Reproduced with permission[7].Copyright 2001, Springer Nature.

1.3 Hematite (Fe_2O_3) photoanode

In PEC water splitting applications, semiconductors must be photoactive materials that absorb light. It can be an n-type or p-type semiconductor. In the n-type, the semiconductor has many electrons, whereas the majority of charge carriers in the p-type semiconductor are holes. Therefore, the photoanode is typically an n-type semiconductor for OER and the photocathode is a p-type semiconductor for HER. Several metal oxides (WO_3, $BiVO_4$, Fe_2O_3, TiO_2)[8–11] have

been widely investigated as n-type semiconductors for photoanodes, primarily due to their general stability in aqueous solutions and comparatively inexpensive materials. Figure 2 shows the band edge positions for various semiconductors. Among them, Fe_2O_3 is one of the most promising photoanode candidates due to its high photochemical stability, specifically under alkaline conditions.[12] Also, it is well-known as a natural abundance and low-cost material. The narrow band gap energy (Eg = ~2.1 eV) allows Fe_2O_3 to absorb visible light, which dominates the spectrum of solar energy on the Earth.[13,14] Moreover, the upper VB of Fe_2O_3 is more positive than the oxidation potential of O_2/H_2O, which is beneficial for water oxidation reactions. Unfortunately, Fe_2O_3 still has serious drawbacks in the PEC performance, mostly, due to poor electrical conductivity (~10^{-2} cm^2 V^{-1} s^{-1}), low absorption coefficient, and short carrier diffusion length.[15–17] These disadvantages lead to the retarded water oxidation kinetics associated with the electron-hole pairs recombination, affecting a low PEC efficiency. Therefore, to address these limitations, it is necessary to develop Fe_2O_3 photoanodes, thereby obtaining a better performance of the PEC water splitting.

1.3.1 Carrier diffusion length

The carriers diffusion length in a semiconductor is defined by the average distance of electrons or holes traveling before they reach the interface. The schematic is presented in Figure 1.3. Fe_2O_3 suffers from a long penetration depth of visible light (α^{-1} = 118 nm at λ = 550 nm) due to its indirect band gap.[16] Consequently, the majority of photogenerated carriers are generated very far from the interface of semiconductor-liquids in the PEC water splitting reaction system. Moreover, the minority charge carrier has only a diffusion length of 2 – 4 nm, which limits the performance of Fe_2O_3 photoanodes.[13] Therefore, the photogenerated electron–hole is easily recombined before reaching the semiconductor–substrate interface. Only a few holes near the interface are involved in the oxygen evolution reaction. With regard to this, the

thin layer of Fe_2O_3 is crucial to overcome the recombination of photogenerated electron–hole pairs. However, when the thickness of Fe_2O_3 decreases, the light is also low-absorbed. The light absorption efficiency and the carriers diffusion length become a trade-off, which affects an immense concern in the poor PEC efficiency of Fe_2O_3 photoanodes.[18,19] A considerable strategy has been made to address this limitation by modifying the thickness of the Fe_2O_3 layer to provide a shorter travel distance to attain the semiconductor-liquid interface. Tuning suitable thickness of the photoelectrode layer should be performed concerning sufficient light absorption. Accordingly, the thickness of the Fe_2O_3 layer is appropriately adjusted to the carrier diffusion length to achieve efficient PEC water splitting.

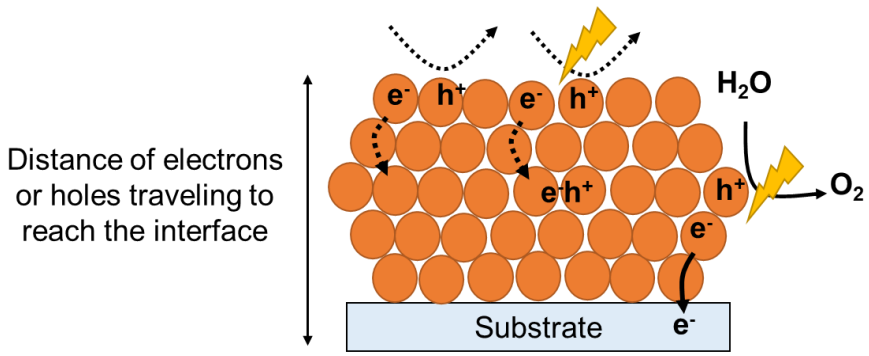

Figure 1.3: Schematic for the carriers diffusion length of the Fe_2O_3 photoanodes.

1.3.2 Doping

As discussed in section 1.3, Fe_2O_3 suffers from a low electrical conductivity, mainly due to poor carrier concentrations. Elemental doping is a frequent strategy to enhance the PEC performance of Fe_2O_3 photoanodes by improving the electron concentration, thereby increasing photocurrent density. The electrical conductivity is proportional to the carrier density, in which the number of charge carriers affects the carrier mobility. The higher carrier density escalates the motion of charge carriers, thus the electrical conductivity is enhanced.[16] Since Fe_2O_3 is categorized as an n-type semiconductor, the impurity dopant with tetravalent cations is necessary to increase the donor level, leading to the improvement of charge carriers. The Fe_2O_3

uptakes electrons from elemental donors such as Ti^{4+} and Sn^{4+}, which is presented by Kröger−Vink notation,[20,21] as shown in Eq. 1 and 2.

$$2TiO_2 \xrightarrow{Fe_2O_3} 2Ti_{Fe}^{\bullet} + 2e' + 3O_O^{\times} + \frac{1}{2}O_2 \quad (1.6)$$

$$2SnO_2 \xrightarrow{Fe_2O_3} 2Sn_{Fe}^{\bullet} + 2e' + 3O_O^{\times} + \frac{1}{2}O_2 \quad (1.7)$$

where e' is the electron, $O_O^{\times}$ is the lattice O^{2-}, $Ti_{Fe}^{\bullet}$ is the Ti^{4+} species in the Fe^{3+} site, and $Sn_{Fe}^{\bullet}$ is the Sn^{4+} species in Fe^{3+} site.

Several metal dopants (Ti^{4+}, Sn^{4+}, $Si^{4+,}$ and Zr^{4+}) have been typically used to increase the PEC performance of Fe_2O_3. Ti^{4+} doping treatment diminished bulk recombination in Fe_2O_3 photoanode, resulting in the improvement of photocurrent response for iodine ion oxidation and water oxidation.[14] Sn doping has been reported on the Fe_2O_3 nanostructures as a photoanode for PEC water splitting. Sn^{4+} substitution at the Fe^{3+} site in Fe_2O_3 improved the photoactivity due to their role as electron donors to increase carrier density.[22] Kim and coworkers fabricated Zr^{4+}-doped Fe_2O_3 with enhanced photocurrent density. The dopant plays an important role in donating electrons to the parent photoanodes, thereby enhancing the donor density.[23] The photocurrent response of nanocrystalline α-Fe_2O_3 has been increased by doping with Si^{4+}. The existence of Si^{4+} dopant decreases the grain size, which increases the specific surface area of the photoanode. Thus, the high number of active surface sites per unit of substrate area leads to enhanced water oxidation efficiency.[24] The heavily doped semiconductor affects an increased absorption in the visible−near-infrared (UV−vis−NIR) region due to the intraband transition, which is the transition of electrons in the conduction band as shown in Figure 1.4.[25,26] This enhancement of absorption is proportional to the improved carrier density.

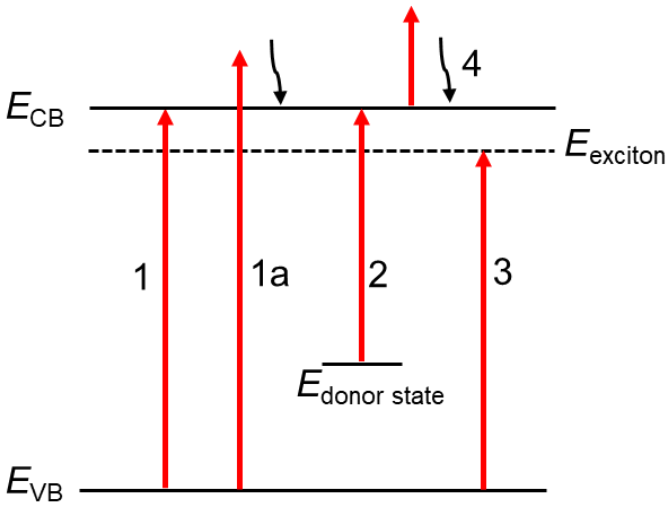

Figure 1.4: Optical transition in semiconductor. Redrawn from[26].

1.3.3 Conductive substrate

The conductive substrate is one of the essential components since it plays the role of a charge collector in the PEC water splitting. The type of conductive layer for the photoanode influences the efficiency of PEC water splitting.[27] For the conventional cell, a two-dimensional (2D) conductive substrate has been mainly employed due to its transparency toward visible light, thus they only absorb light shorter than 400 nm. Additionally, the excellent conductivity of the substrate is another important requirement to be considered. As mentioned in section 1.3.2, most metal oxide semiconductors suffer from the limited diffusion length for the charge carriers due to insufficient conductivity. A polymeric carbon nitride photoanode has been tested on a transparent conductive oxide substrate for PEC water oxidation. However, the photocurrent density was low due to the poor charge mobility of the conductive substrate and insufficient contact between photoanodes and the conductive substrate.[27] Traditional conductive substrates such as fluorine-doped tin oxide (FTO), indium tin oxide (ITO) glass, and titanium sheets have been widely selected for photoelectrode preparation. Nevertheless, the PEC performance still has limitations owing to the small surface area. Recently, three-dimensional (3D) macroporous conductive substrates, such as carbon microfiber felt and

sintered titanium microfiber felt, have been paid much attention.[10,19] Ti felt conductive substrate has high porosity (66.7%) and microporous structure, which are effective for mass-transport-limited reactions. Additionally, it presents a high calculated specific surface area (444 cm^2 g^{-1}) compared to that of 2D Ti sheet conductive substrates (45 cm^2 g^{-1}) at the same thickness.[10,18] For the preparation of photoelectrodes, this characteristic provides benefits with a larger surface of semiconductor–substrate and the layer of film diminishes at a similar loading amount.[18] Moreover, the loading amount increases on the conductive substrate with a larger surface area, which is beneficial for the enhanced photoabsorption.[28]

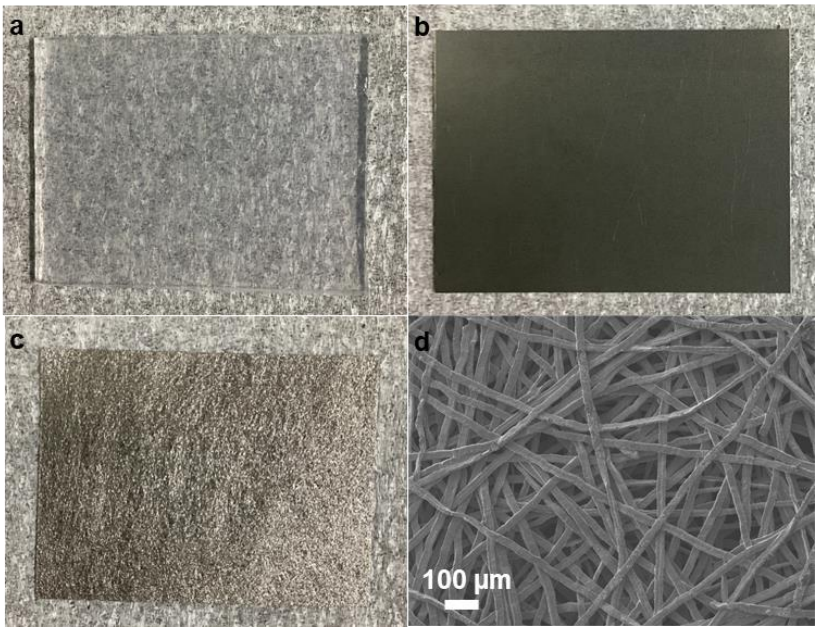

Figure 1.5: Photograph of (a) FTO-glass, (b) Ti sheet, (c) Ti felt conductive substrates, and FESEM images of Ti felt.

1.3.4 Passivation layer

The passivation layer on the semiconductor electrode plays an important role in preventing the consumption of photogenerated, thereby increasing the efficiency of PEC water splitting.[29] For instance, hematite suffers from the drawback due to its severe surface trap, which influences the recombination of photogenerated electron-hole pairs. The surface modification

with the passivation layer diminishes the surface recombination, which decreases the electron back to the interface of hematite/conductive substrates.[30] Various materials with very thin layers, such as Ga_2O_3, Al_2O_3, Nb_2O_5, and TiO_2, have been introduced in the hematite photoelectrodes by the atomic layer deposition (ALD) method to passivate the surface defects.[30–34] This method provides a benefit in controlling the thickness of the passivation layer easily. Figure 1.6a illustrates the presence of surface defects on semiconductor photoelectrodes. Without passivation layer, the photogenerated electrons can easily travel back to the interface due to the surface defect. In the case of the photoanode with a passivation layer, the surface defect can be passivated, thus the recombination of photogenerated electron-hole pairs is suppressed for enhanced water oxidation efficiency, as shown in Figure 1.6b. The ultra-thin Ga_2O_3 underlayer increased the photocurrent density of the Fe_2O_3 photoanode by hindering the electron injection from Fe_2O_3 to the interface of the semiconductor-substrate.[32] The integration of Nb_2O_5 and TiO_2 underlayer improved the PEC efficiency of hematite photoelectrodes due to the synergetic effect of underlayers in enhancing the charge separation and light absorption of the ultrathin hematite photoanodes.[30] Recently, the Al_2O_3 layer demonstrated a passivation effect on the surface state of Fe_2O_3, thus diminishing the photogenerated charge carriers and increasing the efficiency of PEC water oxidation.[33]

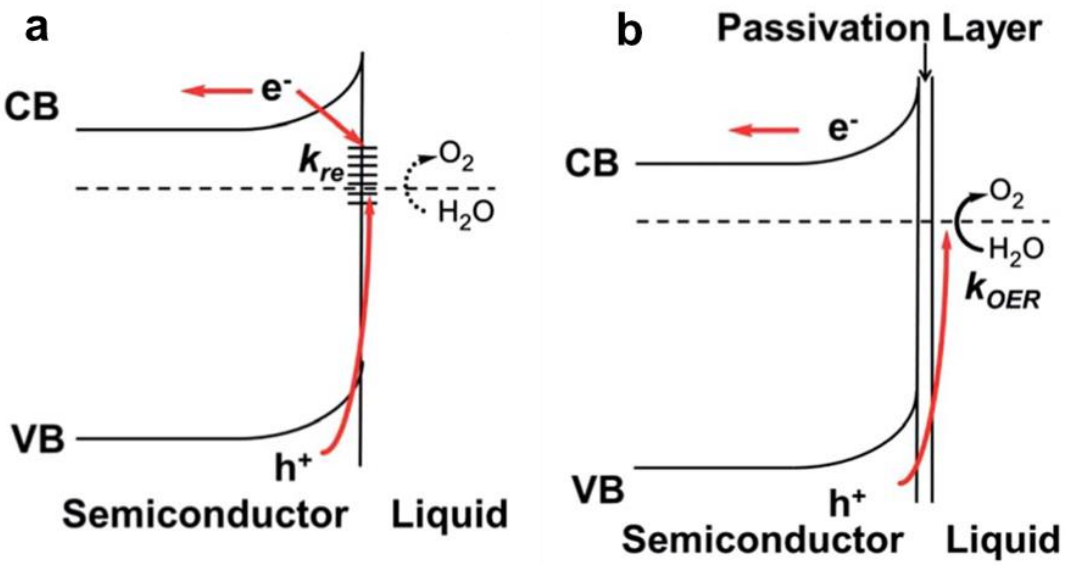

Figure 1.6: Schematic of the band structure for n-type semiconductor (a) without passivation, and (b) with passivation layer. Reproduced with permission[29]. Copyright 2014, Royal Society Chemistry.

1.3.5 Cocatalyst

The PEC efficiency for water oxidation can be improved by an efficient separation and the transfer of photogenerated charge carriers. One of the drawbacks of the PEC performance of hematite photoanode is a sluggish kinetic rate of oxygen evolution reaction (OER). Generally, a cocatalyst for OER has been applied to enhance the PEC efficiency by accelerating the hole transfer, which leads to an increase in water oxidation kinetic. Figure 1.7a exhibits the role of the cocatalyst layer in the n-type semiconductor. The cocatalyst facilitates the hole transfer before reaching the electrolyte and oxidizing water, thereby enhancing the photoanodic performance of the OER reaction.[29] Modification with CoO_x cocatalyst improved the performance of Fe_2O_3 photoanodes for solar water splitting, as shown in Figure 1.7b. The cocatalyst layer cathodically shifted the photocurrent onset due to the suppression of surface recombination and enhancement of water oxidation kinetics, thus PEC properties increased.[31] The CoPi layer presented the improvement of PEC water oxidation over Fe_2O_3 photoanodes. The introduction of this cocatalyst can provide the hole pathway for the water oxidation reaction, which influences facile hole transfer, thus enhancing PEC efficiency.[35] The photoelectrodepostion was observed as an efficient method to deposit the CoPi layer on Fe_2O_3 photoanodes compared to electrodeposition and wet-impregnation methods.[36] Under photo-assisted electrodeposition conditions, CoPi was uniformly deposited on Fe_2O_3 without the formation of nodules over the entire surface.

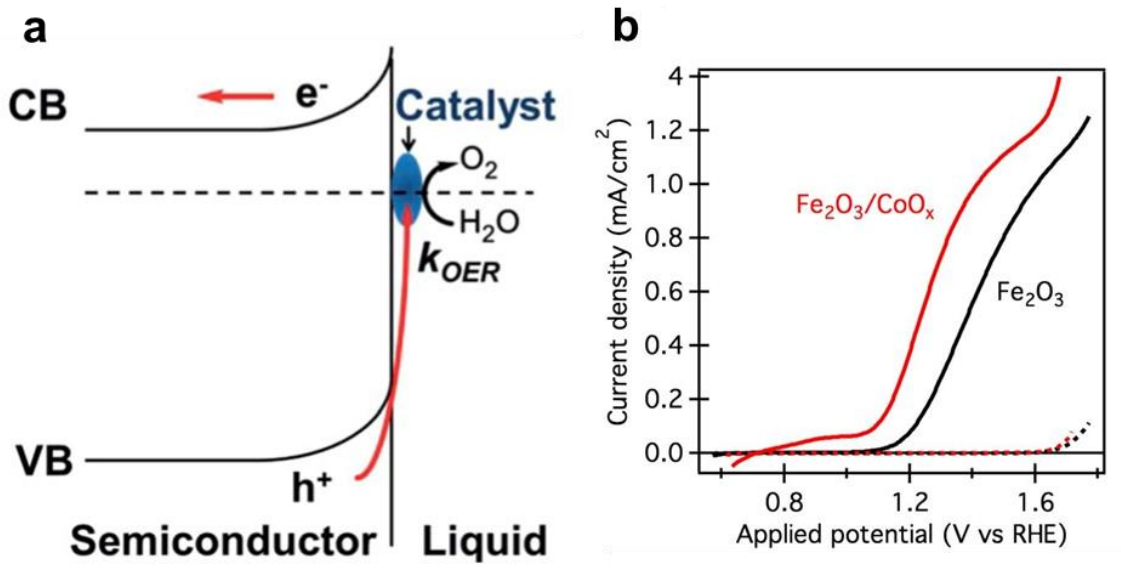

Figure 1.7: Schematic of the band structure for n-type semiconductor (a) with cocatalyst layer.[29] (b) current-potential curve of hematite photoanode with and without cocatalyst. Reproduced with permission[31]. Copyright 2014, Royal Society Chemistry.

1.3.6 Porous photoelectrodes

To date, porous photoelectrodes have attracted immense attention in the PEC water splitting application due to their porosity that enables vapor-fed and mass-transport-limited reactions.[10,11,37–41] Additionally, some researchers used three-dimensional (3D) microporous conductive substrates instead of the conventional two-dimensional (2D) conductive substrates due to their higher specific surface area. As mentioned in section 1.3.3, such property provides the benefits of better PEC efficiency. Several semiconductor photoelectrodes (Cu_2O, WO_3, TiO_2, $CuInS_2$ and $SrTiO_3$) have been prepared on the 3D porous substrates such as Ti felt, Ti-web and carbon felt.[10,11,18,19,37–41] Moreover, WO_3, TiO_2 and $SrTiO_3$ porous photoanodes were successfully investigated in the presence of proton exchange membrane (PEM) as solid electrolyte membrane for PEC water splitting in gas-phase.[10,38,39,42] The membrane contributes to facilitating proton transfer and detaching the anode and cathode sides in the PEC device. Another discovery, the design of the PEC system has been developed as an efficient strategy

for the practical implementation of PEC water splitting. Previous work investigated the PEC hydrogen production in the gas-electrolyte-solid phase boundary as shown in Figure 1.8.[37] This system improved not only the incident photon-to-current conversion efficiency (IPCE) but also the Faraday efficiency (FE). Importantly, this provides a new concept for the combination of porous photoelectrode with the solid electrolyte membrane as membrane electrode assembly (MEA).

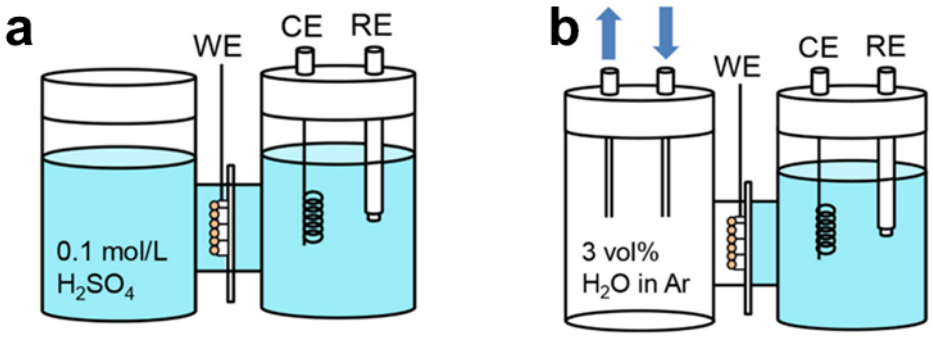

Figure 1.8: Schematic illustrations for the design of PEC cells in the system of (a) "liquid | solid | liquid" interfaces and (b) "gas | solid | liquid" interfaces. Reproduced under Creative Commons Attribution License CC BY 4.0[37]. Frontier's Open Access.

In contrast, there are few reports on the preparation of porous hematite as narrow bandgap photoanodes for PEC applications. Recently, Fe_2O_3 photoanode was fabricated on an FTO-coated transparent porous conducting substrate (TPCS) as shown in Figure 1.9.[41] However, this work necessitated further modification on the FTO-glass using consecutive thermal annealing and APCVD. Moreover, there is no demonstration of the PEC water splitting with the use of a solid electrolyte membrane. Accordingly, the porous hematite photoanode could be developed as MEA for the PEC configuration system, which facilitates mass-transport-limited reactions.

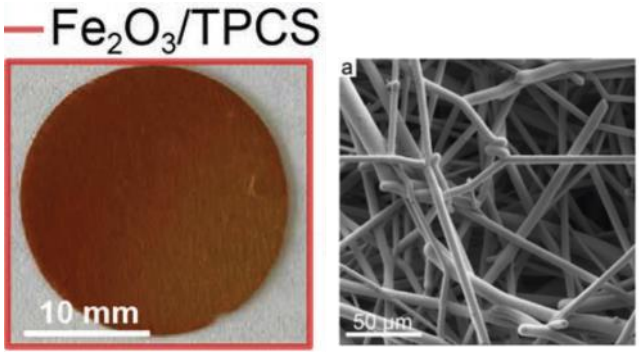

Figure 1.9: Photograph and SEM image of Fe_2O_3/TPCS. Reproduced with permission[41]. Copyright 2023, Wiley.

1.4 Thesis motivation

In this thesis, a hematite photoanode is developed for PEC water splitting application. Fe_2O_3 is one of the most promising photoanode candidates due to its inexpensive and natural abundance material. Additionally, the narrow band gap energy (Eg = ~2.1 eV) is suitable for the PEC water splitting under visible light irradiation. However, Fe_2O_3 still suffers from low PEC efficiency, mainly due to poor electrical conductivity and low light absorption as described in section 1.3. Therefore, it requires some alternative strategies to prepare hematite photoanodes with better and more efficient PEC efficiency.

In Chapter 2, hematite photoanode was studied on FTO-coated glass via a hydrothermal method in the presence of $TiCl_4$ with the assistance of two-step annealing under two different conditions: air calcination at 873 K and subsequent annealing under argon at 473 K. The additional annealing in argon with low temperature was investigated in the preparation of hematite photoanode for the first time. The effect of the two-step annealing treatment was assessed on the PEC properties of the hematite photoanode. As a result, the higher photocurrent response of hematite photoanode was found due to additional annealing in argon atmosphere. In this study, a two-step annealing treatment was highlighted as a strategy to obtain a hematite photoanode with better PEC properties for water oxidation reaction.

In Chapter 3, hematite photoanode was prepared on the different conductive substrates using a hydrothermal method followed by a two-step annealing treatment as discussed in Chapter 2. Even though the fabrication of photoelectrodes on 3D conductive substrates to improve their PEC performance has been described in numerous studies, few have considered the use of Ti microfibers for the fabrication of Fe_2O_3 photoanodes. Importantly, there is no comparison of the PEC performance with 2D conventional substrates and specifically for Fe_2O_3 electrodes. A comparison of PEC properties of hematite photoanode prepared on the different conductive substrates was studied for the first time. As a result of this study, the photoanodes on the 3D macroporous Ti felt produced a higher photocurrent response than that on the 2D conventional FTO-glass.

In Chapter 4, porous hematite photoanodes prepared on the 3D conductive substrates as described previously were further developed for PEC water splitting in two-compartment cells, separating the anode and cathode sides using a solid electrolyte membrane integrated with the membrane electrode assembly (MEA). Anion exchange membrane (AEM) was used as a solid membrane due to its conformity with the alkaline properties of Fe_2O_3. Taking inspiration from the MEA, which separates the anode and cathode in the PEC system, the reaction was demonstrated in pure water without supporting electrolytes under near-neutral conditions. As a result, porous hematite-based photoanodes have succeeded in the AEM-PEC water splitting reaction under visible light irradiation for the first time. By developing a simple and low-cost device, the integration of porous hematite photoanodes with AEM holds great promise for PEC application advancing sustainable energy production in the near future.

References

1. Walter, M. G. *et al.* Solar Water Splitting Cells. *Chem. Rev.* **110**, 6446–6473 (2010).

2. Sivula, K., Le Formal, F. & Grätzel, M. Solar Water Splitting: Progress using Hematite (α-

Fe_2O_3) Photoelectrodes. *ChemSusChem* vol. 4 432–449 (2011).

3. Gan, J., Lu, X. & Tong, Y. Towards Highly Efficient Photoanodes: Boosting Sunlight-Driven Semiconductor Nanomaterials for Water Oxidation. *Nanoscale* **6**, 7142–7164 (2014).
4. A. Fujishima; K. Honda. Electrochemical Photolysis of Water at a Semiconductor Electrode. *Nature* **238**, 37 (1972).
5. Xu, X. T., Pan, L., Zhang, X., Wang, L. & Zou, J. J. Rational Design and Construction of Cocatalysts for Semiconductor-Based Photo-Electrochemical Oxygen Evolution: A Comprehensive Review. *Adv. Sci.* **6**, (2019).
6. Murphy, A. B. *et al.* Efficiency of Solar Water Splitting using Semiconductor Electrodes. *Int. J. Hydrogen Energy* **31**, 1999–2017 (2006).
7. Gratzel, M. Photoelectrochemical Cells. *Nature* **414**, 338–344 (2001).
8. Ta, C. X. M., Akamoto, C., Furusho, Y. & Amano, F. A Macroporous-Structured WO_3/Mo-Doped $BiVO_4$ Photoanode for Vapor-Fed Water Splitting under Visible Light Irradiation. *ACS Sustain. Chem. Eng.* **8**, 9456–9463 (2020).
9. Duret, A. & Grätzel, M. Visible Light-Induced Water Oxidation on Mesoscopic α-Fe_2O_3 Films Made by Ultrasonic Spray Pyrolysis. *J. Phys. Chem. B* **109**, 17184–17191 (2005).
10. Amano, F. *et al.* Vapor-Fed Photoelectrolysis of Water at 0.3 V using Gas-Diffusion Photoanodes of $SrTiO_3$ Layers. *Sustain. Energy Fuels* **4**, 1443–1453 (2020).
11. Stoll, T. *et al.* Visible-Light-Promoted Gas-Phase Water Splitting using Porous WO_3/$BiVO_4$ Photoanodes. *Electrochem. commun.* **82**, 47–51 (2017).
12. Pourbaix, M. Atlas of Electrochemical Equilibria in Aqueous Solutions. *NACE* (1966).
13. Kay, A., Cesar, I. & Grätzel, M. New Benchmark for Water Photooxidation by Nanostructured α-Fe_2O_3 Films. *J. Am. Chem. Soc.* **128**, 15714–15721 (2006).
14. Amano, F., Ohtani, B. & Yoshida, H. Role of Doped Titanium Species in The Enhanced Photoelectrochemical Properties of Iron Oxide Films: Comparison between Water Oxidation and Iodide Ion Oxidation. *J. Electroanal. Chem.* **766**, 100–106 (2016).
15. Brillet, J., Gra, M., Sivula, K. & Fe, P. Decoupling Feature Size and Functionality in Electrodes for Solar Water Splitting. *Nano Lett.* **10**, 4155–4160 (2010).

16. Cesar, I., Sivula, K., Kay, A., Zboril, R. & Grätzel, M. Influence of Feature Size, Film Thickness, and Silicon Doping on The Performance of Nanostructured Hematite Photoanodes for Solar Water Splitting. *J. Phys. Chem. C* **113**, 772–782 (2009).

17. Kraushofer, F. *et al.* Atomic-Scale Structure of The Hematite α-Fe_2O_3(11-02) 'r-Cut' Surface. *J. Phys. Chem. C* **122**, 1657–1669 (2018).

18. Amano, F., Uchiyama, A., Furusho, Y. & Shintani, A. Effect of Conductive Substrate on The Photoelectrochemical Properties of Cu_2O Film Electrodes for Methyl Viologen Reduction. *J. Photochem. Photobiol. A Chem.* **389**, 1–8 (2020).

19. Homura, H., Tomita, O., Higashi, M. & Abe, R. Fabrication of $CuInS_2$ Photocathodes on Carbon Microfiber Felt by Arc Plasma Deposition for Efficient Water Splitting Under Visible Light. *Sustain. Energy Fuels* **1**, 699–709 (2017).

20. Amano, F., Nakata, M., Vequizo, J. J. M. & Yamakata, A. Enhanced Visible Light Response of TiO_2 Codoped with Cr and Ta Photocatalysts by Electron Doping. *ACS Appl. Energy Mater.* **2**, 3274–3282 (2019).

21. Amano, F., Tosaki, R., Sato, K. & Higuchi, Y. Effects of Donor Doping and Acceptor Doping on Rutile TiO_2 Particles for Photocatalytic O_2 Evolution by Water Oxidation. *J. Solid State Chem.* **258**, 79–85 (2018).

22. Ling, Y., Wang, G., Wheeler, D. A., Zhang, J. Z. & Li, Y. Sn-Doped Hematite Nanostructures for Photoelectrochemical Water Splitting. *Nano Lett.* **11**, 2119–2125 (2011).

23. Kim, S. *et al.* A Systematic Study of Post-Activation Temperature Dependence on Photoelectrochemical Water Splitting of One-Step Synthesized FeOOH CF Photoanodes with Erratically Loaded ZrO_2. *Sustain. Energy Fuels* **5**, 3414–3427 (2021).

24. Cesar, I., Kay, A., Martinez, J. A. G. & Grätzel, M. Translucent Thin Film Fe_2O_3 Photoanodes for Efficient Water Splitting by Sunlight: Nanostructure-Directing Effect of Si-Doping. *J. Am. Chem. Soc.* **128**, 4582–4583 (2006).

25. Amano, F., Nakata, M., Yamamoto, A. & Tanaka, T. Effect of Ti^{3+} Ions and Conduction Band Electrons on Photocatalytic and Photoelectrochemical Activity of Rutile Titania For Water Oxidation. *J. Phys. Chem. C* **120**, 6467–6474 (2016).

26. R Memming. Semiconductor Electrochemistry. *Wiley* vol. 27 (1988).

27. Fang, Y., Commandeur, D., Lee, W. C. & Chen, Q. Transparent Conductive Oxides In Photoanodes for Solar Water Oxidation. *Nanoscale Adv.* **2**, 626–632 (2020).

28. Wang, Y. *et al.* A 3D Nanoporous Ni-Mo Electrocatalyst with Negligible Overpotential for Alkaline Hydrogen Evolution. *ChemElectroChem* **1**, 1138–1144 (2014).

29. Liu, R., Zheng, Z., Spurgeon, J. & Yang, X. Enhanced Photoelectrochemical Water-Splitting Performance of Semiconductors by Surface Passivation Layers. *Energy Environ. Sci.* **7**, 2504–2517 (2014).

30. Hisatomi, T. *et al.* Enhancement in the Performance of Ultrathin Hematite Photoanode For Water Splitting By An Oxide Underlayer. *Adv. Mater.* **24**, 2699–2702 (2012).

31. Barroso, M. *et al.* Dynamics of Photogenerated Holes In Surface Modified α-Fe_2O_3 Photoanodes for Solar Water Splitting. *Proc. Natl. Acad. Sci. U. S. A.* **109**, 15640–15645 (2012).

32. Hisatomi, T. *et al.* A Ga_2O_3 Underlayer aAs An Isomorphic Template for Ultrathin Hematite Films Toward Efficient Photoelectrochemical Water Splitting. *Faraday Discuss.* **155**, 223–232 (2012).

33. Zhang, S., Liu, Z., Chen, D. & Yan, W. An Efficient Hole Transfer Pathway on Hematite Integrated by Ultrathin Al_2O_3 Interlayer and Novel CuCoOx Cocatalyst for Efficient Photoelectrochemical Water Oxidation. *Appl. Catal. B Environ.* **277**, (2020).

34. Yang, X. *et al.* Improving Hematite-Based Photoelectrochemical Water Splitting with Ultrathin TiO_2 by Atomic Layer Deposition. *ACS Appl. Mater. Interfaces* **6**, 12005–12011 (2014).

35. Carroll, G. M. & Gamelin, D. R. Kinetic Analysis of Photoelectrochemical Water Oxidationby Mesostructured Co-Pi/α-Fe_2O_3 Photoanodes. *J. Mater. Chem. A* **4**, 2986–2994 (2016).

36. Zhong, D. K., Cornuz, M., Sivula, K., Grätzel, M. & Gamelin, D. R. Photo-Assisted Electrodeposition of Cobalt-Phosphate (Co-Pi) Catalyst on Hematite Photoanodes for Solar Water Oxidation. *Energy Environ. Sci.* **4**, 1759–1764 (2011).

37. Amano, F., Shintani, A., Mukohara, H., Hwang, Y. M. & Tsurui, K. Photoelectrochemical Gas-Electrolyte-Solid Phase Boundary for Hydrogen Production from Water Vapor. *Front. Chem.* **6**, 1–10 (2018).

38. Amano, F., Mukohara, H., Shintani, A. & Tsurui, K. Solid Polymer Electrolyte-Coated Macroporous Titania Nanotube Photoelectrode for Gas-Phase Water Splitting. *ChemSusChem* **12**, 1925–1930 (2019).

39. Amano, F. *et al.* Photoelectrochemical Homocoupling of Methane under Blue Light Irradiation. *ACS Energy Lett.* **4**, 502–507 (2019).

40. Amano, F., Shintani, A., Tsurui, K. & Hwang, Y. M. Fabrication of Tungsten Trioxide Photoanode with Titanium Microfibers as A Three Dimensional Conductive Back Contact. *Mater. Lett.* **199**, 68–71 (2017).

41. Caretti, M. *et al.* Transparent Porous Conductive Substrates for Gas-Phase Photoelectrochemical Hydrogen Production. *Adv. Mater.* **35**, (2023).

42. Zafeiropoulos, G., Johnson, H., Kinge, S., Van De Sanden, M. C. M. & Tsampas, M. N. Solar Hydrogen Generation from Ambient Humidity Using Functionalized Porous Photoanodes. *ACS Appl. Mater. Interfaces* **11**, 41267–41280 (2019).

Chapter 2. Preparation of Ti-doped Fe_2O_3 photoanodes by two-step annealing treatment

2.1 Introduction

Over several decades, photoelectrochemical (PEC) water splitting has been spotlighted as a central investigation focus in the field of photocatalysis to generate hydrogen. The discovery of various materials and the development techniques as preferential strategies to produce an effective outcome in water-splitting applications has been reported in literature through significant research. Hematite (α-Fe_2O_3) has been introduced as an n-type semiconductor electrode candidate owing to its narrow bandgap (~2.1 eV), high chemical stability, and cost-effectiveness.[1–3] However, several drawbacks have been reported for the modest PEC efficiency of Fe_2O_3 photoanodes, such as rapid a recombination of photo-generated electron–hole pairs, narrow hole diffusion length (2–4 nm), poor conductivity (~10^{-2} cm^2 V^{-1} s^{-1}), and slow kinetics.[4–7]

Many researchers have attempted to cope with the limitations of Fe_2O_3 photoanodes, both chemically and physically, for their application as photoanode materials. Efforts to improve the PEC properties of Fe_2O_3 have been classified into four major strategies: i) surface modification, ii) elemental doping, iii) heterojunction, and iv) nanostructuring.[8,9] Among them, elemental doping is commonly considered a facile and effective method to improve electrical conductivity [10]. Several impurity dopants have been investigated for the enhanced photoactivity of Fe_2O_3, such as Si^{4+}, Ti^{4+}, Sn^{4+}, Ni^{2+}, Pt^{4+}, and Mn^{4+}.[11–15] It has been reported that Ti^{4+} doping from titanium tetraisopropoxide increases the photocurrent level of Fe_2O_3.[1] Specifically, the doping of higher valence cations (M^{4+}) compared to the parent Fe^{3+} has been reported to improve the electrical conductivity of Fe_2O_3, which leads to an enhanced photocurrent density.

[16] The Fe_2O_3 uptakes electrons from elemental donors such as Ti^{4+} and Sn^{4+}, which is presented by Kröger−Vink notation,[17] as shown in Eq. 1 and 2.

$$2TiO_2 \xrightarrow{Fe_2O_3} 2Ti_{Fe}^{\bullet} + 2e' + 3O_O^{\times} + \frac{1}{2}O_2 \quad (2.1)$$

$$2SnO_2 \xrightarrow{Fe_2O_3} 2Sn_{Fe}^{\bullet} + 2e' + 3O_O^{\times} + \frac{1}{2}O_2 \quad (2.2)$$

where e' is the electron, $O_O^{\times}$ is the lattice O^{2-}, $Ti_{Fe}^{\bullet}$ is the Ti^{4+} species in the Fe^{3+} site, and $Sn_{Fe}^{\bullet}$ is the Sn^{4+} species in the Fe^{3+} site.

Fe_2O_3 photoanodes have been prepared using several methods, such as electrodeposition, anodization, hydrothermal reaction, spin coating, and chemical vapor deposition.[10,18–21] Hydrothermal synthesis has become a prevalent procedure for fabricating Fe_2O_3 owing to its simplicity, low cost, and scalability.[19] However, post-treatment conditions have been reported to rectify the physicochemical properties of hydrothermally prepared Fe_2O_3. A post-annealing treatment has been introduced to increase the crystallinity of Fe-doped ZnO thin films.[22] Specifically, two-step annealing is performed because it plays an essential role in improving the PEC properties.[23–26] Kim and coworkers reported the preparation of wormlike hematite films by two-step annealing at 823 K and 1073 K.[27] However, this investigation applied high temperature in the second annealing and there was no clear explanation for the effect of the two-step annealing on the PEC properties. It is noted that the second annealing of rutile TiO_2 in a nitrogen atmosphere boosts the donor density and PEC efficiency for water oxidation.[28] Additionally, Makimizu and coworkers reported that annealing in argon improved the PEC properties of Fe_2O_3 because the formed oxygen vacancies improved the electrical conductivity.[29] However, there are no reports on Fe_2O_3 films subjected to sequential annealing in air and argon atmospheres.

The emergence of both electrons and oxygen vacancies by annealing in a non-oxidizing atmosphere can be explained by Eq. 3, as expressed by Kröger−Vink notation;[1,30]

$$Fe_2O_3 \xrightarrow{Fe_2O_3} 2Fe_{Fe}^{\times} + 2e' + 2O_O^{\times} + V_O^{\bullet\bullet} + \frac{1}{2}O_2 \quad (2.3)$$

where $V_O^{\bullet\bullet}$ is an oxygen vacancy with a double positive charge. However, $V_O^{\bullet\bullet}$ can also act as a recombination center, leading to decreased efficiency.[16]

Herein, Ti-doped Fe_2O_3 films were hydrothermally prepared on fluorine-doped tin oxide (FTO)-coated glass substrates, followed by two-step annealing treatments in air at 873 K and argon at 473 K. The Ti^{4+} doping was sourced from titanium (IV) chloride solution ($TiCl_4$) in ethanol solution with various volumes of 0, 100, 150, and 200 μL, which are further denoted as Ti-0, Ti-100, Ti-150, and Ti-200, respectively. These findings explore the effect of two-step annealing in a non-oxidizing atmosphere on the PEC properties of Ti-doped Fe_2O_3 on FTO-coated glass (FTO/Ti-Fe_2O_3). Several characterizations of the prepared photoanodes were investigated to elucidate the effect of the second annealing in an argon atmosphere at 473 K on the PEC properties for water oxidation in an alkaline solution. Argon was employed as inert gas for non-oxidizing conditions.

2.2 Experimental section

2.2.1 Preparation of FTO/Ti-Fe_2O_3

FTO-coated glass sheets with a thickness of 1.8 mm were purchased from AGC Fabritech Co., Ltd. Iron (III) nitrate nonahydrate ($Fe(NO_3)_3$•$9H_2O$, 99.9%), $TiCl_4$ (16–17% as Ti), and $NaNO_3$ (99.9%) were obtained from Wako Pure Chemical Industries, Ltd. All chemical reagents were of analytical grade and were employed without purification.

The hydrothermal preparation was performed by following the synthesis reported in previous studies.[1] FTO glass with a size of 3 cm × 3 cm (length × width) was cleaned with

acetone and deionized water. To prepare an aqueous solution of 0.10 mol L^{-1} $Fe(NO_3)_3$ and 1.0 mol L^{-1} $NaNO_3$, 0.808 g of $Fe(NO_3)_3 \cdot 9H_2O$ and 1.70 g $NaNO_3$ were dissolved in 20 mL of deionized water while stirring for 30 min. At the same time, 0.053 mol L^{-1} $TiCl_4$ in ethanol solution at volumes of 100, 150, and 200 μL was incorporated into the mixture and stirred for 30 min. The Ti/Fe ratio of Ti-100, Ti-150, and Ti-200 in feed is consistent with 0.27, 0.40, and 0.53 at.%, respectively. Afterward, the solution was transferred to a 50 mL stainless-steel Teflon-lined autoclave. The FTO glass was placed vertically into the vessel for a hydrothermal reaction at 393 K for 10 h. The hydrothermally prepared samples were cleaned with ethanol and deionized water and then dried at 373 K for 10 min. This sample was denoted as FTO/Ti-Fe_2O_3(hyd).

The FTO/Ti-Fe_2O_3(hyd) samples were calcined at 873 K for 2 h in air and denoted as FTO/Ti-Fe_2O_3(air). Finally, the air-calcined sample was annealed at 473 K for 2 h under an argon stream of 100 mL min^{-1} at 0.1 MPa. 2h has been adopted as sufficient annealing time. The sample after both heat treatments, which is called "two-step annealing," is denoted as FTO/Ti-Fe_2O_3(two-step). The sample without Ti doping is denoted as Ti-0. For the sample with necking treatment, Ti-0 was drop cast by 0.05 mol L^{-1} $TiCl_4$ in ethanol (10 μL) five times. The drop-casting sample was calcined at 873 K for 2 h in air and further annealed at 473 K for 2 h in argon.

2.2.2 Characterization

The loading of Fe_2O_3 on the substrates was measured with X-ray fluorescence (XRF, NEX CG, Rigaku). The structure of the samples was analyzed by X-ray diffraction (XRD, SmartLab diffractometer, Rigaku) at 2θ of 20°–70° with Cu Kα radiation at 45 kV and 200 mA. Scanning electron microscopy (SEM, JSM-7800F, JEOL) with an acceleration voltage of 10.0 kV, which was connected to an energy-dispersive X-ray spectrometer (EDS, JED-2300, JEOL), was

employed to investigate the morphology and elemental composition of the photoanodes. The optical properties were observed using a UV-visible–near-infrared (NIR) diffuse reflectance spectrophotometer (UV-2600, Shimadzu) in the wavelength range of 200-1400 nm. Raman spectra were obtained using a confocal Raman microscope (XploRA PLUS, Horiba) with a laser wavelength of 532 nm. X-ray photoelectron spectroscopy (XPS) was conducted using an X-ray photoelectron spectrometer (JPS-9010MX, JEOL) with Mg Kα radiation. The binding energies were calibrated by C 1s at 285.0 eV. Belsorp-mini II (MicrotracBEL) was used to measure the nitrogen adsorption and desorption isotherm. Before the measurement, the samples were evacuated at 473 K for 2 h. The specific surface area was analyzed by Brunauer–Emmet–Teller (BET) method. The pore size distribution was estimated according to the Barret–Joyner–Halenda (BJH) method.

2.2.3 Photoelectrochemical measurements

PEC properties were tested in a 1 mol L^{-1} NaOH solution (pH = 13.6) at a temperature range of 295–300 K in air. A three-electrode system in a one-compartment cell was used with a Hg/HgO reference electrode, a platinum wire counter electrode, and a working electrode of FTO/Ti-Fe_2O_3 with a geometrical area of 1.0 cm^2. Photoirradiation was sourced from a solar simulator (XES-40S1, San-ei Electric) at AM 1.5 G one-sun with an irradiance of 100 mW cm^{-2}. The spectral distribution of the solar simulator is presented in Figure 2.1. Linear sweep voltammetry was conducted at a sweep rate of 50 mV s^{-1} from −0.5 to 1.2 V vs. Hg/HgO. The measured potential was converted to the reversible hydrogen electrode (RHE) using the following Nernst equation:

$$E\ [\text{V vs. RHE}] = E\ [\text{V vs. Hg/HgO}] + 0.059\ \text{pH} + E^{\circ}(\text{Hg/HgO}), \quad (2.4)$$

where $E°$(Hg/HgO) is +0.098 V vs. the standard hydrogen electrode. In chronoamperometry, the photocurrent density was measured at 1.50 V vs. RHE for 900 s under on/off light conditions.

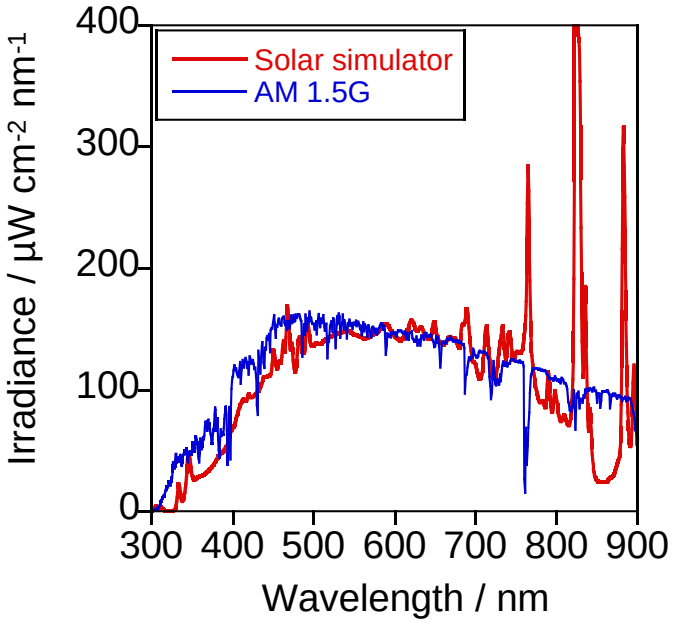

Figure 2.1: Spectral distributions of a solar simulator (San–ei Electric XES–40S1) and the standard air mass 1.5 global (AM 1.5G) solar spectrum (100 mW cm^{-2}).

The action spectrum of the incident photon-to-current conversion efficiency (IPCE) was investigated using a 300-W xenon lamp (MAX-303, Asahi Spectra) with bandpass filters. The IPCE, which is the ratio of the number of electrons of the photocurrent to the number of incident photons, was calculated using the following equation:

$$\mathrm{IPCE} = \frac{J_{\mathrm{photo}}}{I_0} \times \frac{1240}{\lambda} \tag{2.5}$$

where J_{photo}, I_0, and λ are the photocurrent density [mA cm^{-2}], incident light intensity [mW cm^{-2}], and wavelength [nm], respectively. I_0 was quantified using an optical power meter (3664, Hioki).

The Mott–Schottky measurement was conducted at a frequency of 1 kHz with an applied sinusoidal amplitude of 10 mV in the dark. The imaginary part of the electrochemical impedance, assuming a series capacitor–resistor model, was employed to measure the capacitance of the space charge layer (C). The donor density (N_D) and flat-band potential (E_{fb}) were determined by plotting $1/C^2$ versus the applied potential (E) using the following Mott–Schottky equation, assuming that an ideal semiconductor model was appropriate:

$$\frac{1}{C^2}=\frac{2}{q\varepsilon\varepsilon_0 N_D}\left(E-E_{fb}-\frac{kT}{q}\right) \tag{2.6}$$

where q is the elementary electric charge, ε is the dielectric constant (taken as 12 for Fe_2O_3), ε_0 is the permittivity of vacuum, k is Boltzmann's constant, and T is the temperature.

The sheet resistance (R_s) of the photoanodes was measured using a four-point probe associated with a digital multimeter (3441A, Agilent). Electrochemical impedance spectroscopy (EIS) was performed using a potentiostat (VersaSTAT 3, Princeton applied research) at a frequency range from 100 kHz to 0.1 Hz and an amplitude of 10 mV.

2.3 Results and discussion

2.3.1 Characterization of FTO/Ti-Fe_2O_3

The weight of bare FTO was ~0.45 g on a 1 cm^2 area. The weight of FTO/Ti-Fe_2O_3 samples was ~0.48 g cm^{-2}, indicating the loading of Ti-Fe_2O_3 is ~30 mg cm^{-2}. Table 2.1 summarizes the results of XRF analysis for FTO/Ti-Fe_2O_3(air) and FTO/Ti-Fe_2O_3(two-step) at various Ti doping levels. The two-step annealed samples were first calcined at 873 K and subsequently annealed in argon at 473 K. No significant change in the loaded Fe (at.%) was observed after additional annealing in argon. The ratio between Ti and Fe loading (Ti/Fe ratio) for Ti-Fe_2O_3 of Ti-100, Ti-150, and Ti-200 increased with an increase in the amount of $TiCl_4$ in the

hydrothermal synthesis solution. The existence of Sn, Ca, and Si was due to tin oxide and soda-lime glass. No other impurities were observed on the FTO substrate.

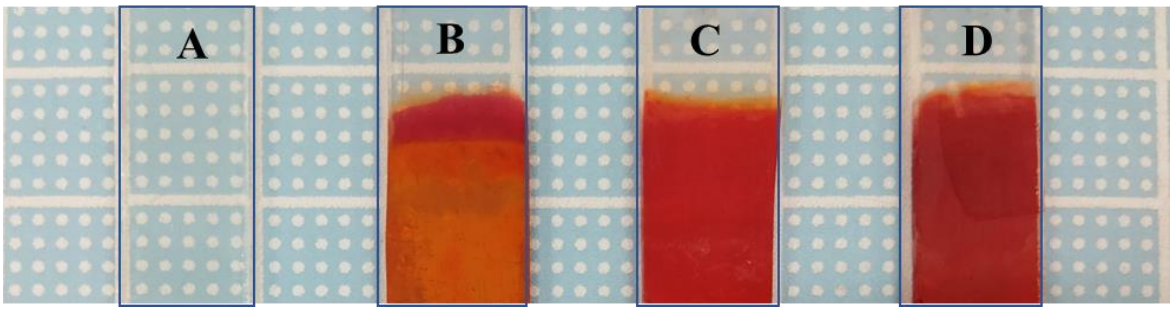

Figure 2.2: Digital image of (A) bare FTO, (B) FTO/Ti-Fe_2O_3(hyd), (C) FTO/Ti-Fe_2O_3(air), and (D) FTO/Ti-Fe_2O_3(two-step) of Ti-150.

Table 2.1. XRF analysis of the loading amount (mass%) of Fe_2O_3 composition of bare FTO, FTO/Ti-Fe_2O_3(air) [a], and FTO/Ti-Fe_2O_3(two-step) [b]

Sample	Ca (mass%)	Si (mass%)	Sn (mass%)	Fe (mass%)	Ti (mass%)	Ti/Fe ratio
Bare FTO	58.3	39.5	2.15	0.00	0.00	—
Ti-100 [a]	43.4	26.9	2.30	26.3	1.08	0.048
Ti-150 [a]	45.3	25.0	2.47	25.8	1.41	0.064
Ti-200 [a]	53.1	24.7	1.95	19.0	1.26	0.077
Ti-100 [b]	42.2	27.4	2.04	27.3	1.14	0.049
Ti-150 [b]	49.1	53.6	1.39	24.5	1.38	0.066
Ti-200 [b]	53.4	24.2	3.73	17.4	1.25	0.084

[a] FTO/Ti-Fe_2O_3(air) was prepared by the hydrothermal method with different $TiCl_4$ amounts (100, 150, and 200 μL), which are denoted as Ti-100, Ti-150, and Ti-200, and after calcination in air at 873 K.
[b] FTO/Ti-Fe_2O_3(two-step) was obtained after annealing in argon at 473 K.

Figure 2.2 shows photographic images of FTO/Ti-Fe_2O_3 after being hydrothermally treated, calcined in air, and annealed in argon. The color of the FTO/Ti-Fe_2O_3 film was reddish-orange. This result is similar to that reported in the literature.[3] Figure 2.3 shows the UV-visible–NIR

spectra of FTO/Ti-Fe_2O_3 before and after the two-step annealing. The photoabsorption edges of the FTO/Ti-Fe_2O_3 samples were observed at approximately 600–700 nm. It is noted that there was a broad absorption in the NIR region compared with the bare FTO glass. FTO/Ti-Fe_2O_3(hyd) exhibits the lowest NIR absorption. In addition, the NIR absorption of FTO/Ti-Fe_2O_3(two-step) was higher than that of FTO/Ti-Fe_2O_3(air) calcined in air. NIR absorption is attributed to the electron transition in shallow traps and the conduction band.[30,31] The shallow traps act as donors to enhance the conductivity of the n-type semiconductors. It is noteworthy that two-step annealing enhanced the electron concentration in FTO/Ti-Fe_2O_3. For further evaluation of the optical bandgap, Tauc analysis of all samples is presented in Figure 2.3B. Principally, FTO/Ti-Fe_2O_3 samples exhibited a bandgap value of 2.05 eV in all treatments. The bandgap of FTO was 3.87 eV (Fig.2.3C). It can be concluded that the effect of air and two-step annealing was negligible for the bandgap but significant for photoabsorption in the NIR region.

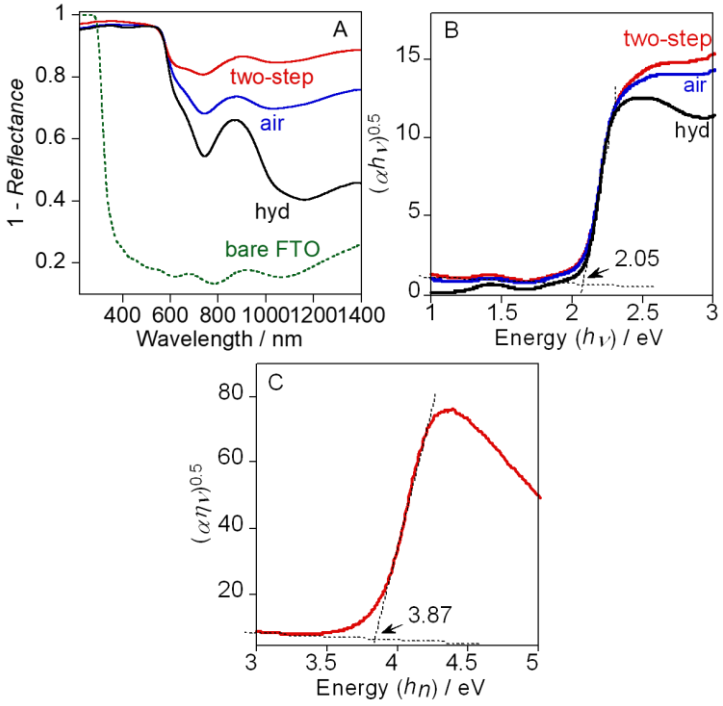

Figure 2.3: (A) Diffuse reflectance UV-visible–NIR spectra; (B) Tauc plots of FTO/Ti-Fe_2O_3(hyd), FTO/Ti-Fe_2O_3(air), and FTO/Ti-Fe_2O_3(two-step) of Ti-150 and (C) FTO-coated glass.

Figure 2.4 shows XRD patterns of FTO/Ti-Fe_2O_3(air) and FTO/Ti-Fe_2O_3(two-step). It can be seen that the peaks at 26.5°, 33.8°, 37.9°, 51.5°, 54.5°, 61.6°, and 65.7° correspond to the diffraction pattern of the SnO_2 standard (PDF 01-077-0452). For the XRD pattern of all FTO/Ti-Fe_2O_3 samples, eight major peaks at 24.2°, 33.1°, 35.6°, 40.8°, 49.5°, 54.0°, 62.4°, and 63.9° were detected, which are attributed to the hematite (α-Fe_2O_3, PDF 01-089-0596) of R-3c space group. The XRD pattern exhibits that no FeOOH was formed in FTO/Ti-Fe_2O_3(hyd). Further, there was the formation of hematite with very low-intensity peaks at 24.2°, 33.1°, and 35.6°in FTO/Ti-Fe_2O_3(hyd). Hematite was completely formed by calcination in air at 873 K. No peak shifts or impurities were observed for FTO/Ti-Fe_2O_3(two-step). This result indicates that there was no structural alteration by the argon treatment at 473 K.

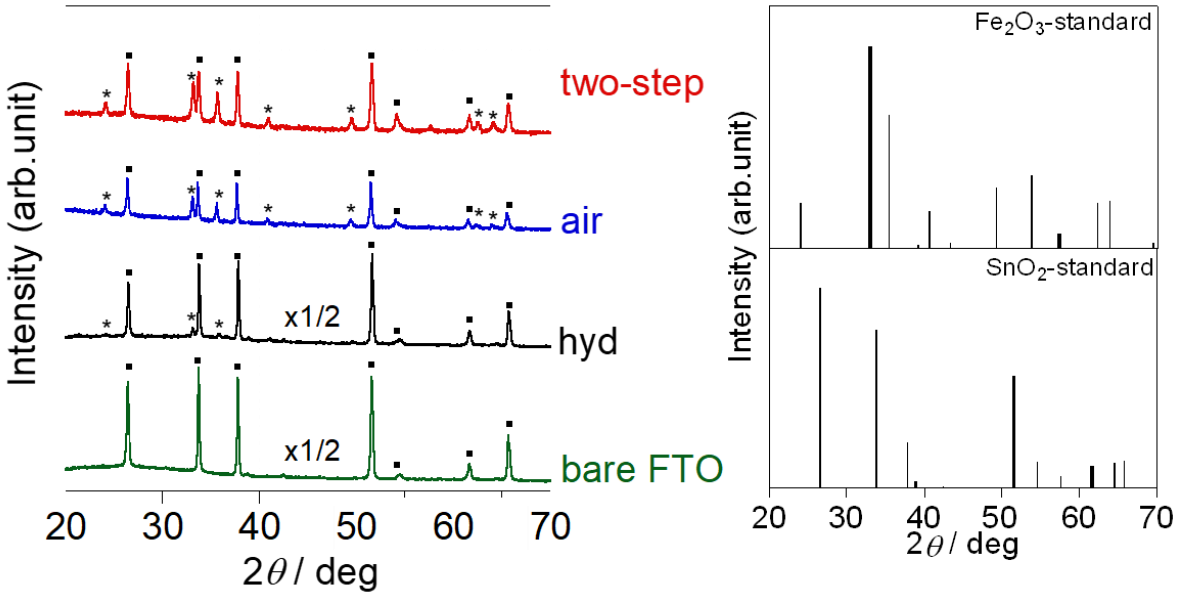

Figure 2.4: X-ray diffraction patterns of bare FTO substrate, FTO/Ti-Fe_2O_3(hyd), FTO/Ti-Fe_2O_3(air), and FTO/Ti-Fe_2O_3(two-step) of Ti-150 (left). The signs of asterisk and square correspond to the characteristic of α-Fe_2O_3 and SnO_2, respectively. Powder Diffraction File data of SnO_2 (ICDD 01-077-0452) and trigonal α-Fe_2O_3 (ICDD 01-089-0596) (right).

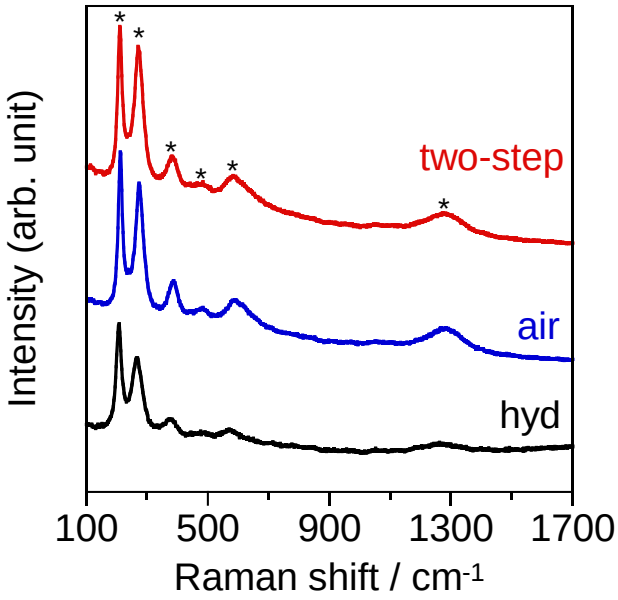

Figure 2.5: Raman spectra of FTO/Ti-Fe_2O_3(hyd), FTO/Ti-Fe_2O_3(air), and FTO/Ti-Fe_2O_3(two-step) of Ti-150.

The Raman spectra of FTO/Ti-Fe_2O_3(hyd), FTO/Ti-Fe_2O_3(air), and FTO/Ti-Fe_2O_3(two-step) are presented in Figure 2.5. All samples presented several bands at 209, 270, 382, 483, 582, and 1271 cm^{-1}, which are assigned to hematite (α-Fe_2O_3).[32] FTO/Ti-Fe_2O_3(hyd) exhibits the lowest band intensity. FeOOH was not present in FTO/Ti-Fe_2O_3(hyd). This result is in good agreement with the XRD results. The bandwidth of FTO/Ti-Fe_2O_3(air) was lesser than that of FTO/Ti-Fe_2O_3(hyd), indicating an increase in the Fe_2O_3 crystallinity.[1] The increased band intensity can be attributed to the improved crystallinity by calcination in air at 873 K.

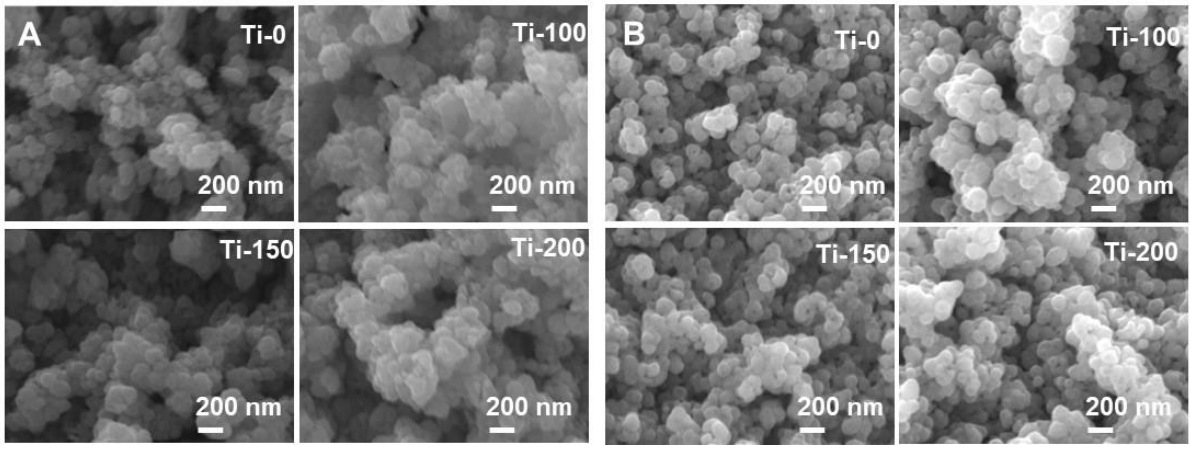

Figure 2.6: (A) SEM images of FTO/Ti-Fe_2O_3(air) and (B) FTO/Ti-Fe_2O_3(two-step) at various Ti doping levels.

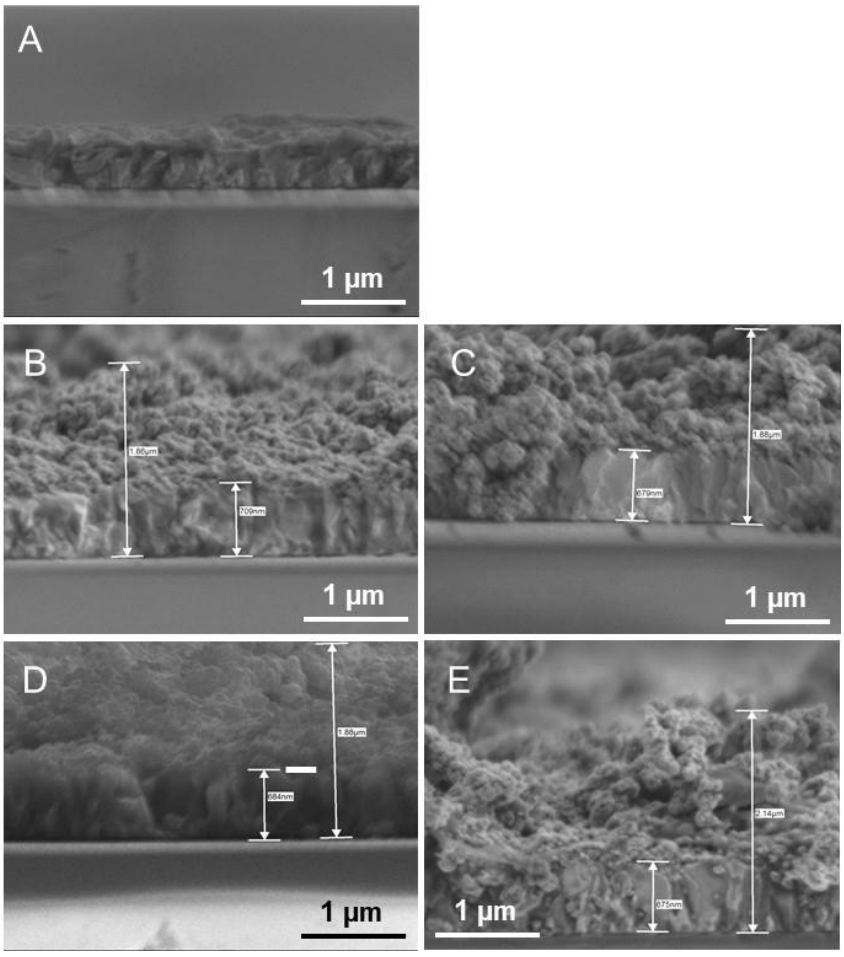

Figure 2.7: Cross-sectional side view SEM images of (A) Bare FTO-coated glass and FTO/Ti-Fe_2O_3(two-step) at various Ti doping levels: (B) Ti-0, (C) Ti-100, (D) Ti-150, and (E) Ti-200.

Figure 2.6A shows the SEM images of FTO/Ti-Fe_2O_3(air) prepared at various Ti doping levels. The morphologies of all samples were similar, with a spherical shape and agglomerated particles. For FTO/Ti-Fe_2O_3(two-step), the morphology is also spherical as shown in Figure 2.6B. Additionally, it is confirmed that the diameter of the Fe_2O_3 particles was in the range of 75–90 nm for FTO/Ti-Fe_2O_3(air) at all Ti doping levels. After two-step annealing, the particle size was also in the range of 70–90 nm. This result suggests that argon treatment at 473 K did not influence the particle size of Fe_2O_3 on the FTO substrate. Cross-sectional side-view SEM images of bare FTO and FTO/Ti-Fe_2O_3 are presented in Figure 2.7. The thickness of the Fe_2O_3 layer was in the range of 1–1.5 μm, and the thickness of the FTO layer was ~0.7 μm. SEM–

Table 2.2 SEM–EDS quantitative analysis of the elemental composition of FTO/Ti-Fe_2O_3(two-step) at various Ti doping levels

Sample	Ti (at.%)	Fe (at.%)	Sn (at.%)	Ti/Fe ratio
Ti-0	Not detected	25.42	74.58	—
Ti-100	1.01	47.85	51.14	0.021
Ti-150	1.62	53.50	44.88	0.030
Ti-200	1.91	46.98	51.11	0.041

EDS elemental mapping images are shown in Figure 2.8. It can be seen that all constituent atoms composed of Ti, Fe, and Sn were uniformly distributed on the surface. Table 2.2 summarizes the EDS elemental composition of the FTO/Ti-Fe_2O_3 photoanodes at various Ti doping levels. The ratio between Ti and Fe loading (Ti/Fe ratio) for Ti-Fe_2O_3 of Ti-100, Ti-150, and Ti-200 were shown to be 0.021, 0.030, and 0.041, respectively. This result suggests that the Ti/Fe ratio is enhanced with an increase in the amount of $TiCl_4$ in the hydrothermal synthesis solution.

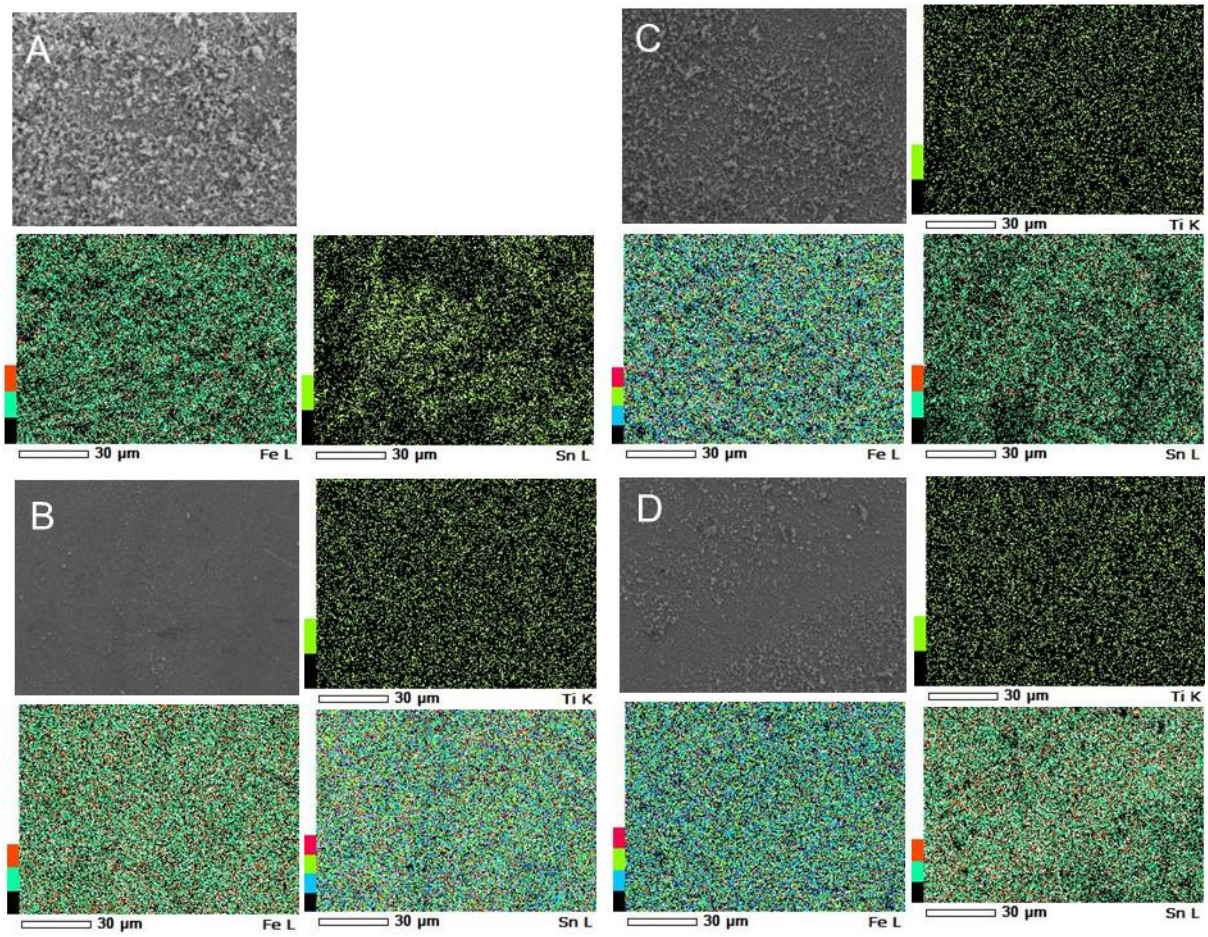

Figure 2.8: SEM-EDS elemental mapping of FTO/Ti-Fe_2O_3(two-step) at various Ti doping levels: (A) Ti-0, (B) Ti-100, (C) Ti-150, and (D) Ti-200.

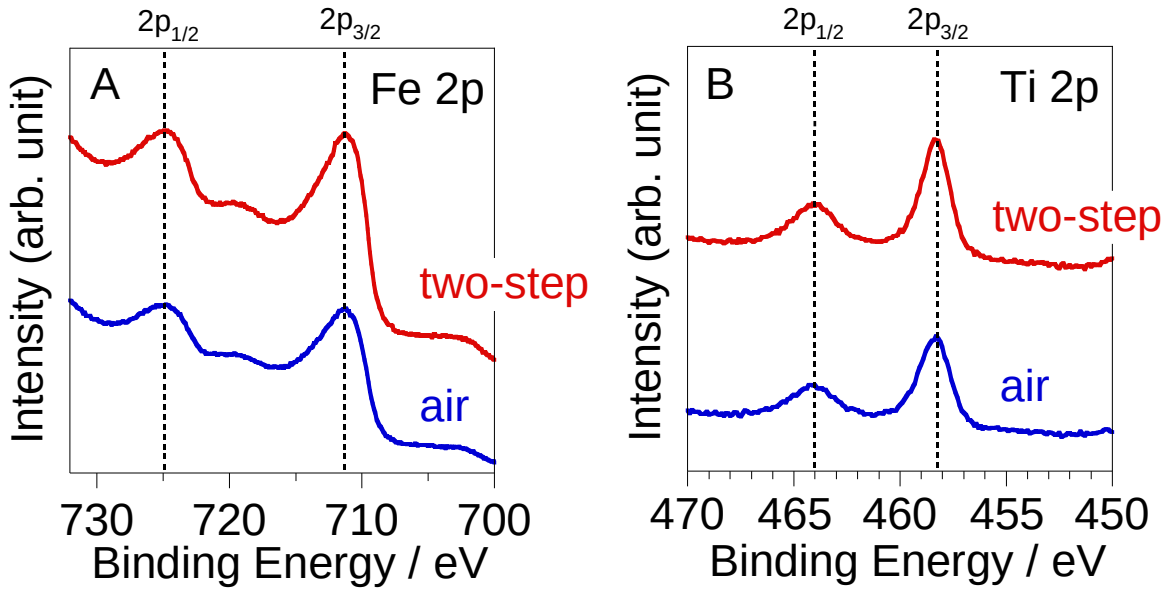

Figure 2.9: X-ray photoelectron spectra of (A) Fe 2p and (B) Ti 2p of FTO/Ti-Fe_2O_3 (Ti-150).

XPS measurements were performed to validate the presence of Ti species on the surfaces of the FTO-Fe_2O_3 films. Figure 2.9 shows the XPS spectra of FTO/Ti-Fe_2O_3(air) and FTO/Ti-Fe_2O_3(two-step) of Ti-150. This result suggests that the electron density of the FTO-Fe_2O_3 films could be increased by the two-step annealing treatment. The binding energy of Fe $2p_{3/2}$ at 711.3 eV (Figure 2.9A) is assigned to Fe^{3+} in Fe_2O_3, indicating that the Fe species exists as Fe^{3+}.[1] The binding energy of Ti $2p_{3/2}$ at 458.3 eV (Figure 2.9B) is in good agreement with Ti^{4+}.[1] This result suggests that the doped Ti species in the FTO-Fe_2O_3 thin film was Ti^{4+}. The two-step annealing treatment exhibited no significant disparity in the Fe 2p and Ti 2p spectra. The atomic ratio of Ti/Fe was calculated to be around 0.11, indicating that Ti^{4+} species are rich on the surface. Additionally, the samples after Ar etching treatment (700V, 14 mA) for 60 sec were assessed (Figure 2.10). The binding energy of Ti $2p_{3/2}$ at 458.1 eV is assigned to Ti^{4+}. This result suggests that the Ti species doped in the bulk are similar to the Ti^{4+} species on the surface. The atomic ratio of Ti/Fe decreased to around 0.020. The presence of Ti^{4+} in the bulk was lower than that on the surface, indicating that the doped Ti^{4+} species were segregated near the surface.

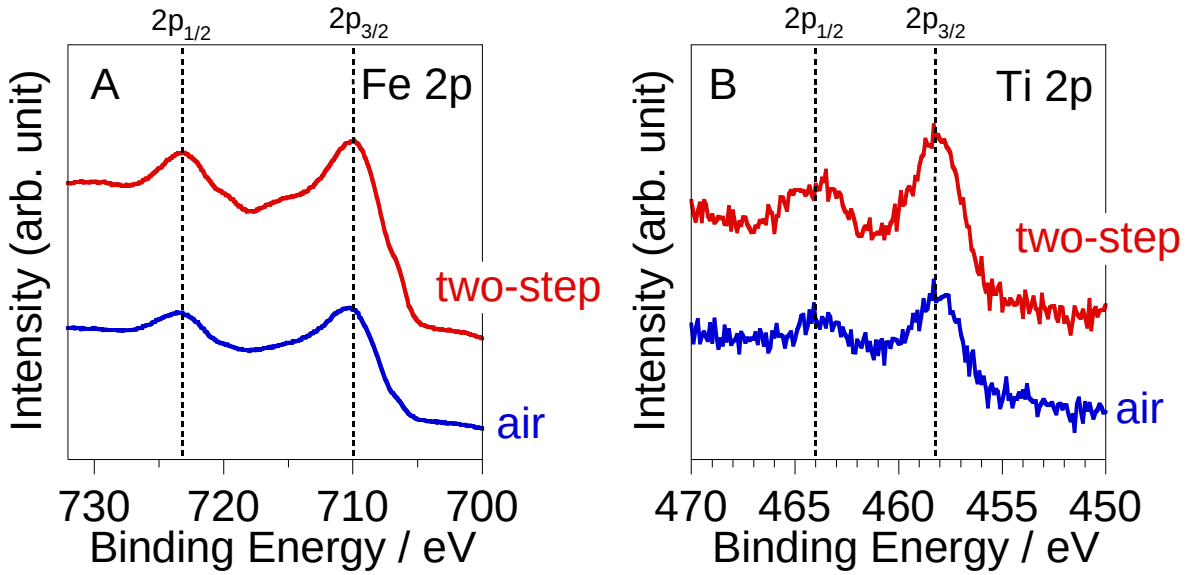

Figure 2.10: X-ray photoelectron spectra of (A) Fe 2p and (B) Ti 2p of FTO/Ti-Fe_2O_3 (Ti-150) after Ar ion etching treatment at 700 kV and 14 mA for 60 sec.

Next, the specific surface area (SSA) of Ti-Fe_2O_3 powder prepared with a similar condition for Ti-150(two-step) was analyzed. BET method was used to analyze the N_2 adsorption isotherm (Figure 2.11). The SSA of Ti-Fe_2O_3 (two-step) was found to be 25.2 m^2 g^{-1}. The pore size distribution is shown in Fig. S7B. The pore volume Ti-Fe_2O_3 (two-step) calculated by the Barret-Joyner-Halenda (BJH) method was 0.33 cm^3 g^{-1}. The pore size distribution was mainly observed in the range of 5–100 nm, indicating the presence of mesopores in Fe_2O_3 particles. The high SSA and large pore volume would be beneficial for the photoelectrochemical activity of Fe_2O_3.

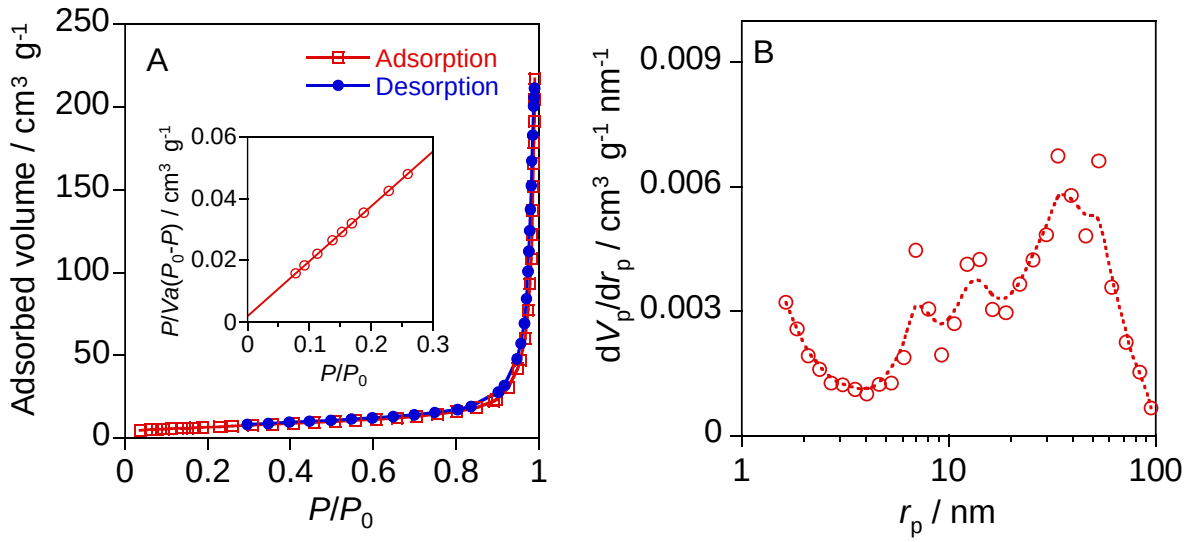

Figure 2.11: (A) N_2 adsorption and desorption curves and (B) Pore size distribution of Ti-150 (two-step) powder (inset: BET plot).

2.3.2 Photoelectrochemical properties

The PEC water-splitting performance of FTO/Ti-Fe_2O_3(air) and FTO/Ti-Fe_2O_3(two-step) was measured in a 1 mol L^{-1} NaOH solution. Figure 2.12 shows the effect of Ti doping on the linear sweep voltammogram under 1 sun irradiation (I_0 = 100 mW cm^{-2}). The anodic

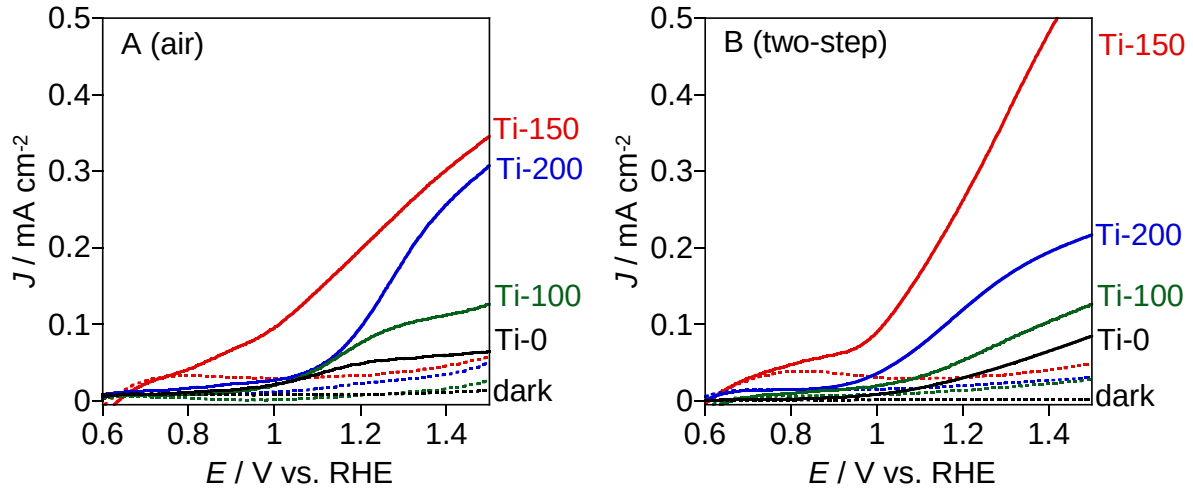

Figure 2.12: Current–potential curves of (A) FTO/Ti-Fe_2O_3(air) and (B) FTO/Ti-Fe_2O_3(two-step) with various Ti dopant amounts in 1 mol L^{-1} NaOH solution under AM 1.5G illumination (100 mW cm^{-2}). The dashed curves were obtained without irradiation.

photocurrent is attributed to the oxidation of water. Increasing the Ti doping concentration from 0 to 150 µL resulted in an increased photocurrent density of FTO/Ti-Fe_2O_3(air) (Figure 2.12A). However, the photocurrent response decreased slightly for Ti-200 and Ti-150 exhibited the highest photocurrent density. The onset potential of the photocurrent response was located at ~0.8 V vs. RHE, which is consistent with the onset potential reported for Fe_2O_3 photoanodes.[33] For FTO/Ti-Fe_2O_3(two-step), the same trend was observed for the dependence of photocurrent density on the Ti doping amount (Figure 2.12B). The highest photoresponse was obtained for Ti-150 of FTO/Ti-Fe_2O_3(two-step). Note that FTO/Ti-Fe_2O_3(hyd) showed no photoresponse, indicating that calcination at 873 K is necessary to enhance the charge separation. Additionally, Figure 2.13 shows the effect of temperatures (423, 473, and 523 K)

of argon annealing on the photocurrent density of Ti-150(two-step). The highest photocurrent density was obtained by subsequent annealing in argon at 473 K. When the two-step annealing at 773 K was performed, the sample color was changed to black. This suggests that Fe_2O_3 is reduced in argon at high temperatures.

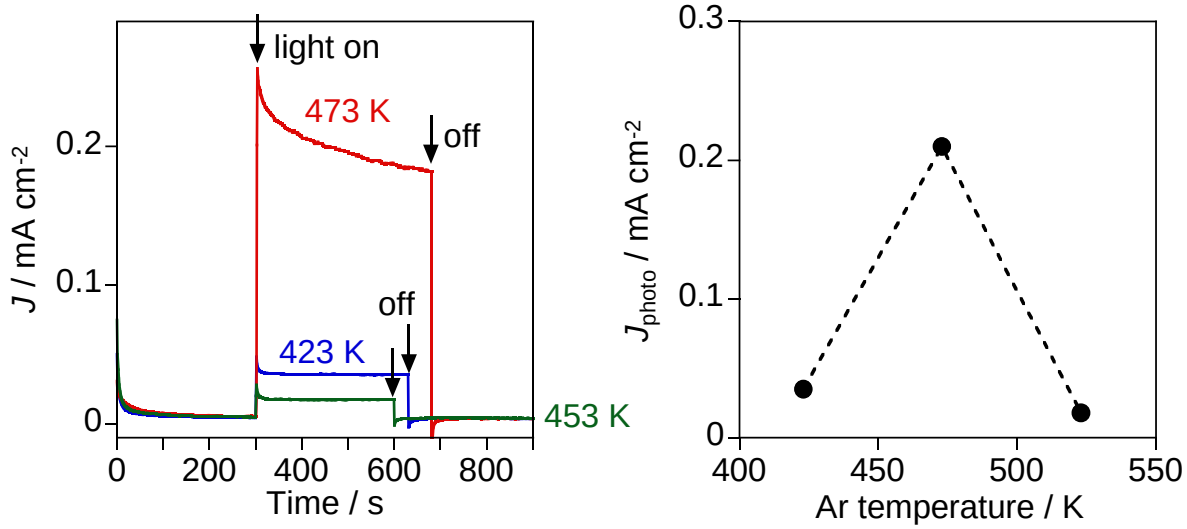

Figure 2.13: Effect of temperature of argon annealing on the photocurrent response of FTO/Ti-Fe_2O_3(Ti-150) in 1 mol L^{-1} NaOH solution.

Figure 2.14 shows current–time curves at 1.50 V vs. RHE under 1 sun irradiation (300–600 s, I_0 = 100 mW cm^{-2}). The J_{photo} of Ti-Fe_2O_3(air) with Ti doping of 100, 150, and 200 µL were shown to be 0.05, 0.18, and 0.09 mA cm^{-2}, respectively (Figure 2.13A). In case of the sample without $TiCl_4$, the photocurrent response was only 0.02 mA cm^{-2}. This result is in good agreement with the previous report, stating that the low $TiCl_4$ concentration enhances the photocurrent density and the absence of $TiCl_4$ addition produced a poor photocurrent response. [32] The result trends are in line with the result of linear sweep voltammetry measurements (Figure 2.12A).

Subsequently, the PEC properties of FTO/Ti-Fe_2O_3 after two-step annealing were evaluated. Figure 2.14B shows that the FTO/Ti-Fe_2O_3(two-step) exhibits a higher photocurrent density than that of FTO/Ti-Fe_2O_3(air). Surprisingly, an increase in photocurrent response was

observed on Ti-150 of FTO/Ti-Fe_2O_3(two-step), which was 0.55 mA cm^{-2} at 1.50 V vs. RHE and approximately three times higher than that of calcined in the air (0.18 mA cm^{-2} at 1.50 V vs. RHE). It should be noted that the two-step annealing treatment leads to an enhancement in the photocurrent density of the hydrothermally prepared Ti-Fe_2O_3.

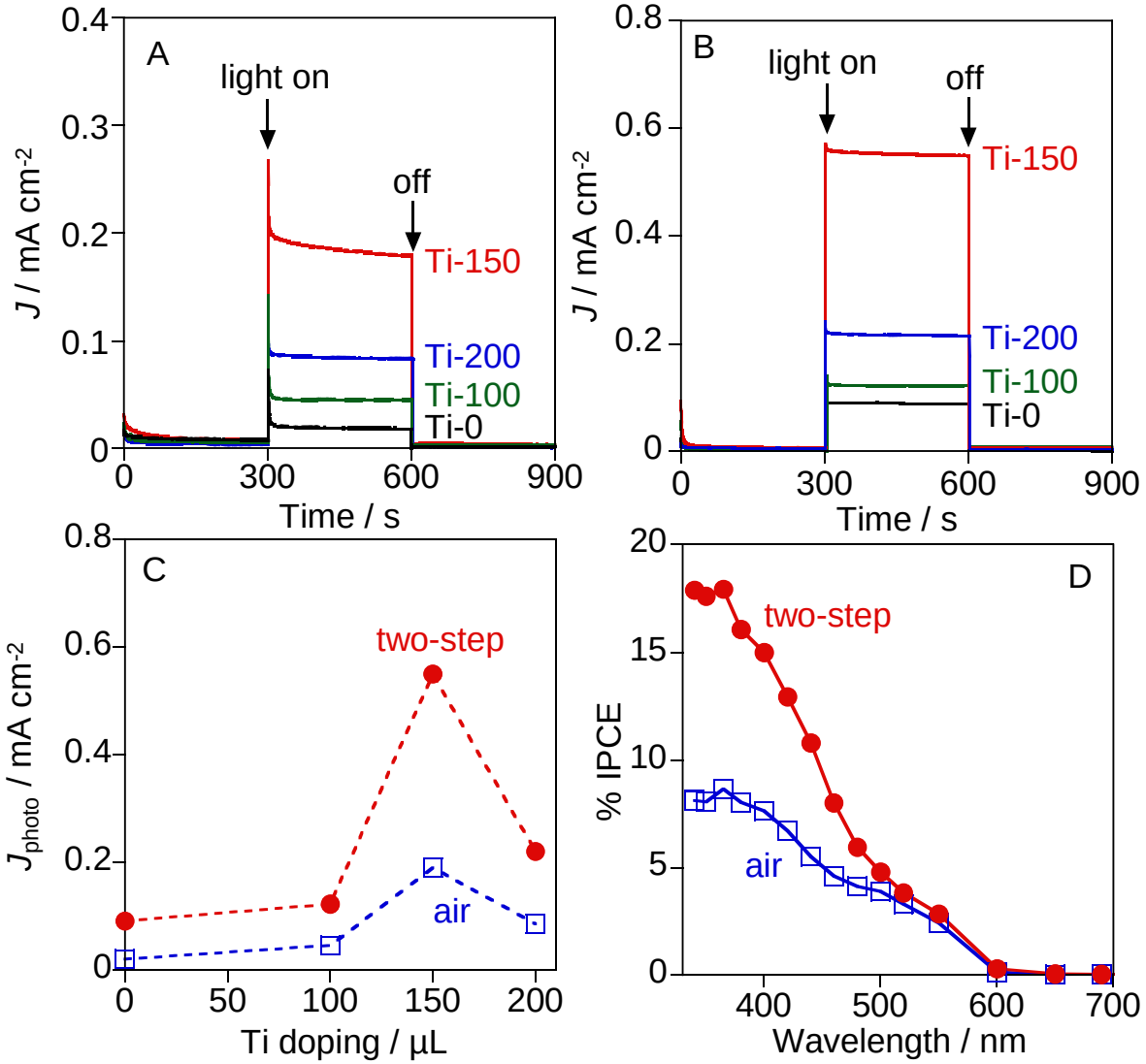

Figure 2.14: Current–time curves of (A) FTO/Ti-Fe_2O_3(air) and (B) FTO/Ti-Fe_2O_3(two-step) in 1 mol L^{-1} NaOH solution at 1.50 V vs. RHE under AM 1.5G illumination (300–600 s, 100 mW cm^{-2}). (C) Effect of Ti dopant amount on the photocurrent density. (D) IPCE action spectra of FTO/Ti-Fe_2O_3(air) and FTO/Ti-Fe_2O_3(two-step) of Ti-150 at 1.50 V vs. RHE.

Figure 2.14C summarizes the effect of the two-step annealing treatment on the J_{photo} of FTO/Ti-Fe_2O_3 with various Ti doping levels. By two-step annealing, an enhanced J_{photo} was observed for all FTO/Ti-Fe_2O_3 samples. The optimized Ti doping concentration was 150 μL. A previous study reported that the Ti^{4+} dopant incorporated into Fe_2O_3 suppressed the recombination of photoexcited carriers.[30] From the measurements of two different two-step annealed samples with various Ti doping (Figure 2.15), this reproducibility indicates that Ti-150 still showed the highest photocurrent density. In contrast, a negligible increase in the photocurrent density was observed for FTO/Fe_2O_3 without Ti doping. These results suggest that the two-step annealing treatment is effective for Ti-Fe_2O_3 to produce an increased PEC efficiency.

To further evaluate the PEC properties, the IPCE action spectra of the optimized Ti-150 were measured at 1.50 V vs. RHE, as displayed in Figure 2.14D. In both calcination in air and two-step annealing, FTO/Ti-Fe_2O_3 exhibited IPCE onset at approximately 600 nm, which corresponds to the bandgap value of Fe_2O_3 (~2.05 eV). In addition, the Ti-Fe_2O_3(two-step) exhibited a higher IPCE value than that of Ti-Fe_2O_3(air) over the same wavelength in both the UV and visible regions. Specifically, the IPCE reached its highest value (~22.5%) at 365 nm for Ti-Fe_2O_3(two-step). An improved IPCE value was observed in the visible region of 400–500 nm. This result suggests that FTO/Ti-Fe_2O_3 exhibits a good photoresponse under visible-light irradiation.

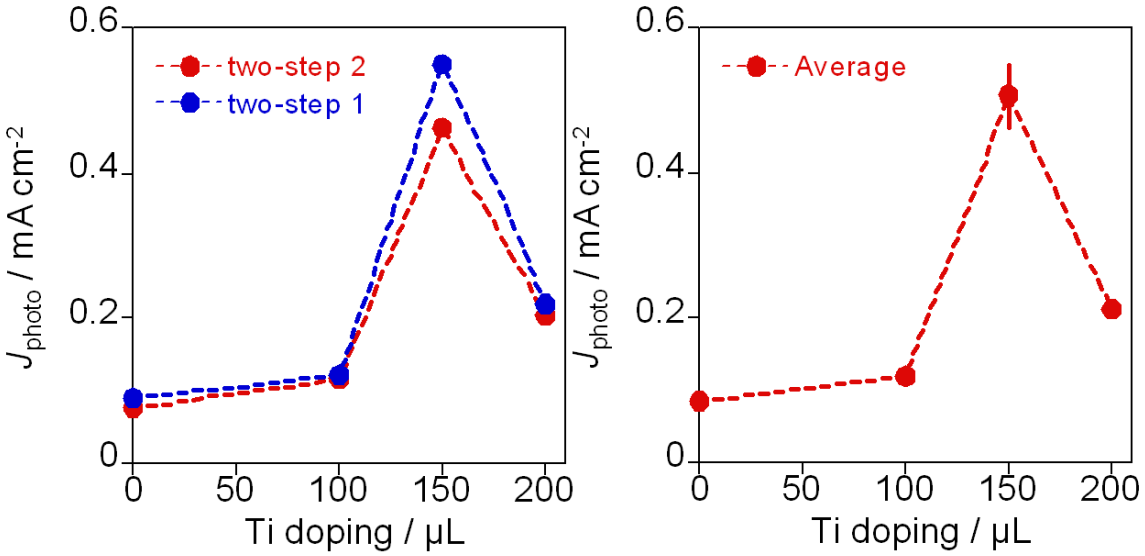

Figure 2.15. Effect of Ti doping on the photocurrent response of two-step annealed sample with reproducibility in 1 mol L^{-1} NaOH solution. The error bars were from measurements of two different two-step annealed samples.

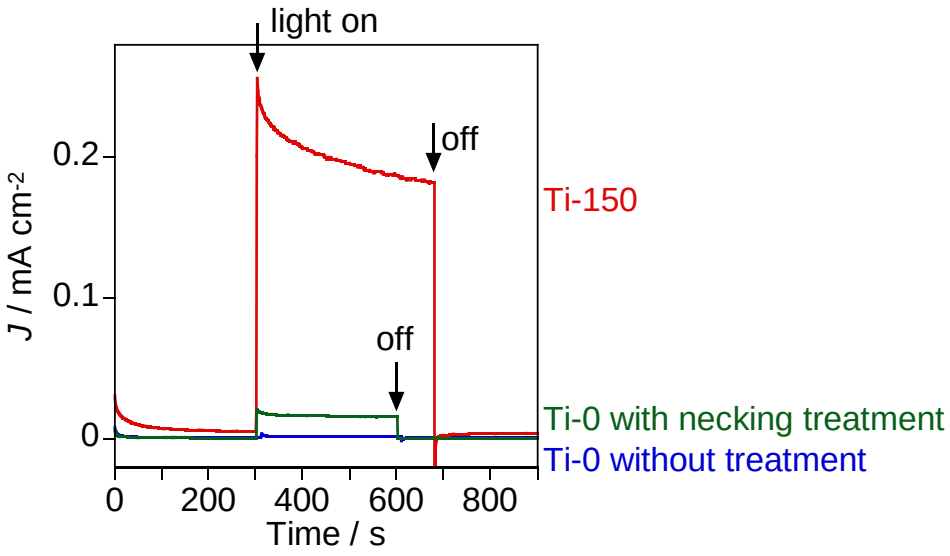

Figure 2.16. Effect of post-necking treatment on the photocurrent response of Ti-0(two-step) in 1 mol L^{-1} NaOH solution.

Moreover, the effect of post-necking treatment using $TiCl_4$ solutions as a precursor on the photocurrent response of FTO/Fe_2O_3 without Ti doping was observed. Post-necking treatments are frequently applied for dye-sensitized solar cells based on TiO_2 and particulate photoanodes to decrease the grain-boundary resistance.[34–36] Figure 2.16 shows the current-time curve of Ti-

0(two-step) with necking treatment. The necking treatment only showed a low increase in photocurrent response, indicating that the TiO_2 layer on the surface is ineffective for the enhancement of PEC performance. This result suggests that the high photocurrent response of FTO/Ti-Fe_2O_3 is attributed to the doping of Ti^{4+} species.

2.3.3 Electron concentration and conductivity

Mott–Schottky measurements were performed to determine the N_D, which indicates the electron density of the n-type semiconductor. The N_D was calculated from the semiconductor capacitance (C) by assuming an ideal flat electrode.[28] Figure 2.17 shows the Mott–Schottky plots of FTO/Ti-Fe_2O_3 at various Ti doping levels before and after two-step annealing. The obtained positive slope indicates the n-type conductivity of the semiconductor. The slope and x-intercept provide the N_D and flat-band potential (E_{fb}), respectively. Principally, both the sample calcined in air and the two-step annealed sample exhibit a similar trend for the Mott–Schottky analysis result (Table 2.3). The Ti-150 exhibited the highest positive value of E_{fb}. Generally, the sample with Ti doping showed the enhanced N_D after the argon annealing. In specific, N_D increased in connection with the Ti doping from 0 to 150 μL and then slightly decreased at 200 μL. Importantly, Ti-150 showed the highest N_D after the post-argon treatment at 473 K, which was 2.64×10^{19} cm^{-3}. The N_D analysis was consistent with the result of photocurrent density. This result indicates that the enhanced photocurrent density is attributed to the increase in electron density due to the Ti-doping and two-step annealing treatments.

The electron density produced by reductive conditions can be explained by Eq. 3, where conduction electrons appear because of oxygen vacancies.[1,30] In contrast, as shown in Eq. 1, Ti^{4+} doping suppresses the formation of oxygen vacancies, which might act as a recombination center. The oxygen vacancies on the surface were passivated by water to generate two hydroxyl groups, as explained by the following Eq. 2.7:[30]

$$V_O^{\bullet\bullet} + H_2O + O_O^{\times} \rightarrow 2(OH)_O^{\bullet} \quad (2.7)$$

where $(OH)_O^{\bullet}$ is a hydroxyl group in the oxygen lattice. The electrons generated in Ti-Fe_2O_3 could increase the electron density after post-argon annealing. The two-step annealing treatment boosted the N_D of FTO/Ti-Fe_2O_3, which increased the photocurrent density.

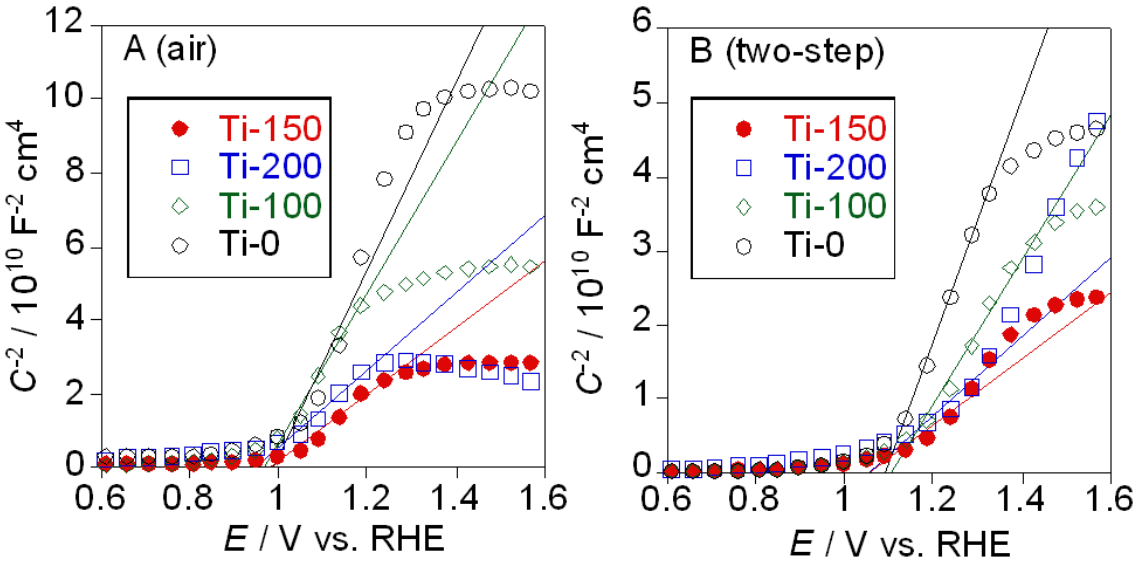

Figure 2.17: Mott–Schottky plots of (A) FTO/Ti-Fe_2O_3(air) and (B) FTO/Ti-Fe_2O_3(two-step) at various Ti doping levels in 1 mol L^{-1} NaOH solution.

Table 2.3. Mott–Schottky analysis result of FTO/Ti-Fe_2O_3 in 1 mol L^{-1} NaOH solution

Sample	FTO/Ti-Fe_2O_3(air)		FTO/Ti-Fe_2O_3(two-step)	
	E_{fb} / V vs. RHE	N_D / cm^{-3}	E_{fb} / V vs RHE	N_D / cm^{-3}
Ti-0	1.00	3.29×10^{18}	1.07	7.17×10^{18}
Ti-100	0.94	5.81×10^{18}	1.08	1.20×10^{19}
Ti-150	0.95	1.30×10^{19}	1.03	2.64×10^{19}
Ti-200	0.92	1.12×10^{19}	1.03	2.20×10^{19}

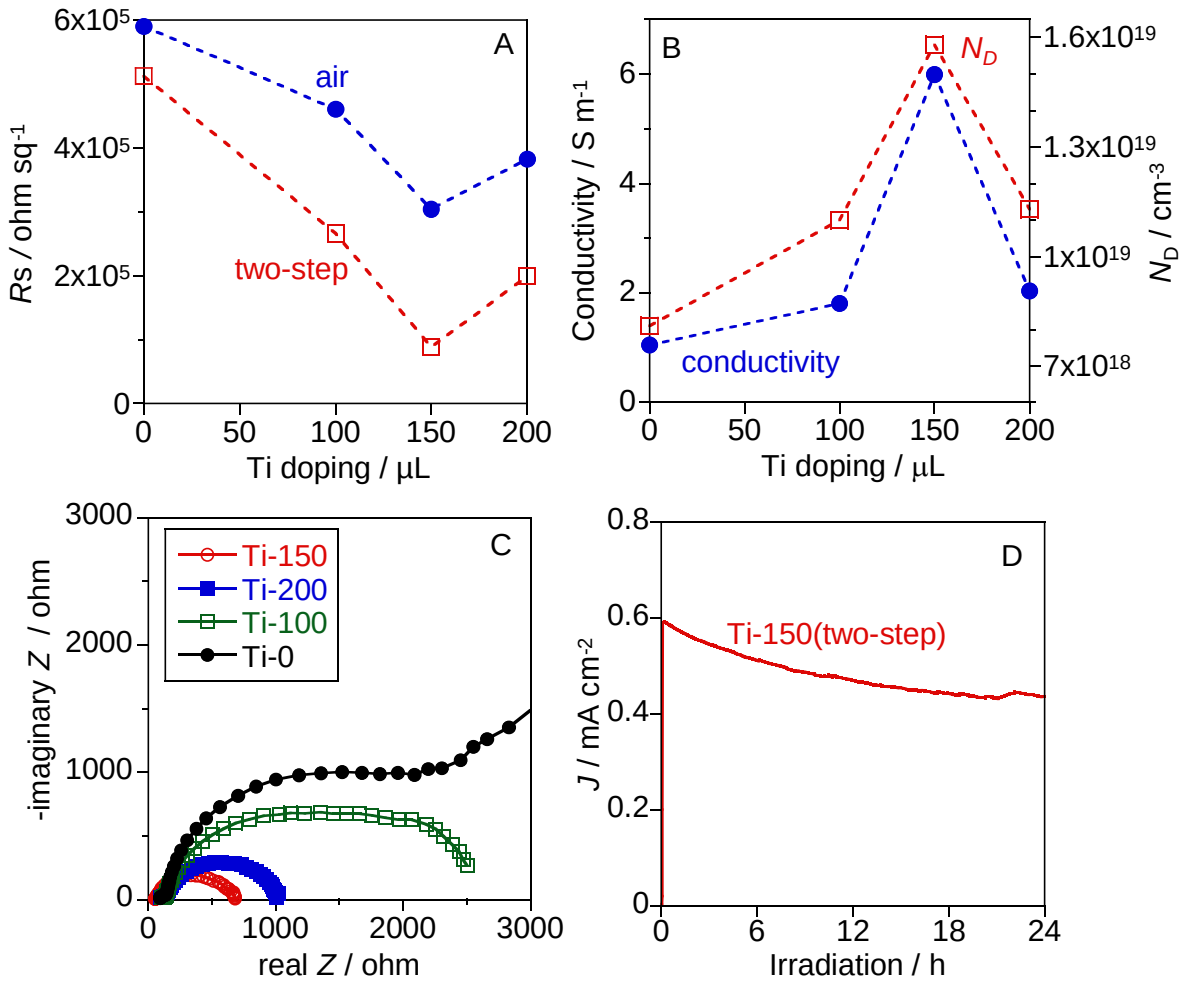

Figure 2.18: (A) Effect of Ti dopant amount on the sheet resistance (R_s) of FTO/Ti-Fe_2O_3(air) and FTO/Ti-Fe_2O_3(two-step). (B) Relationship curve between conductivity (σ) and donor density (N_D) of FTO/Ti-Fe_2O_3(two-step). (C) EIS curves of FTO/Ti-Fe_2O_3(two-step) at 1.50 V vs. RHE under AM 1.5G illumination (100 mW cm^{-2}). (D) Photocurrent stability measurements of Ti-150(two-step) in 1 mol L^{-1} NaOH at 1.50 V vs. RHE under 385 nm irradiation for 24 h (I_0 = 17 mW cm^{-2}).

In n-type semiconductors, the enhancement of the electron density is in line with the improved electrical conductivity. To confirm the increased electrical conductivity, R_s measurements were performed for the photoanodes at various Ti doping amounts. Figure 2.18A displays the effect of two-step annealing on the R_s of FTO/Ti-Fe_2O_3 determined by the four-

point probe method. It is important to note that the R_s value was attributed not only to the Fe_2O_3 film but also to the underlying FTO substrate because electrons can migrate from the Fe_2O_3 film to the underlying FTO substrate with high conductivity.[28,30] The two-step annealed samples generate lower R_s than those calcined in air for all observed Ti doping. Importantly, the Ti-150 of FTO/Ti-Fe_2O_3(two-step) exhibits the lowest R_s, which is approximately three times lower than that of FTO/Ti-Fe_2O_3(air). This low R_s is ascribed to the increase in electrical conductivity.[28,30]

Figure 2.18B presents the correlation between the conductivity (σ) and N_D of the FTO/Ti-Fe_2O_3(two-step). Conductivity, σ, was calculated using the following equation:

$$\sigma = \frac{1}{R_s \times T} \tag{2.8}$$

where T is the thickness of the conductive layer. In the case of the conductivity of FTO/Ti-Fe_2O_3, T was calculated from the sum of the FTO and Fe_2O_3 thicknesses. The thicknesses of the Ti-Fe_2O_3 and FTO layers were obtained from SEM measurements (Figure 2.7).

Table 2.4. Summary of the calculation of conductivity and donor density (N_D) of bare FTO-coated glass and the FTO/Ti-Fe_2O_3(two-step) photoanodes at various Ti doping

Samples	R_s / kΩ sq^{-1}	Thickness of FTO / μm	Thickness of Fe_2O_3 / μm	Conductivity / S m^{-1}
Bare FTO	0.0086	0.75	-	1.54×10^5
Ti-0	512.5	0.71	1.15	1.05
Ti-100	293.8	0.68	1.20	1.81
Ti-150	88.8	0.68	1.20	5.99
Ti-200	229.6	0.68	1.47	2.04

Table 2.4 summarizes the calculated conductivity and N_D of FTO/Ti-Fe_2O_3(two-step) at various Ti doping levels. Interestingly, a similar trend was observed between the conductivity

and N_D of FTO/Ti-Fe_2O_3. Ti-150 exhibits a high N_D and high conductivity. In contrast, the FTO/Fe_2O_3 without Ti doping resulted in a low N_D with low conductivity. This result suggests that the improvement in electrical conductivity is attributed to the increased concentration of electrons. It is important to note that the two-step annealing treatment simultaneously increases both the electrical conductivity and the electron density of the Ti^{4+}-doped Fe_2O_3 photoanode, which results in an enhanced PEC efficiency.

EIS measurement of FTO/Ti-Fe_2O_3(two-step) was performed at 1.50 V vs. RHE under photoirradiation. The Nyquist plot presents the impedance in the real and imaginary parts, as shown in Figure 2.18C. A semicircle with a distortion was observed, indicating that the active sites in the reaction are heterogeneous.[1] It is noted that the smallest diameter of the semicircle was found to be FTO/Ti-Fe_2O_3(Ti-150). This behavior is attributed to the most effective carrier separation, which enhances the migration of electron-hole to the surface.[33,37] Therefore, FTO/Ti-Fe_2O_3(Ti-150) exhibits the highest PEC performance. This result is consistent with the analyses of photocurrent response and electron density.

FTO/Ti-Fe_2O_3 (Ti-150) (two-step) was checked for its photocurrent stability within 24 h at an applied potential of 1.50 V vs. RHE (Figure 2.18D). After 24 h of irradiated time, the photocurrent density of FTO/Ti–Fe_2O_3 photoanodes was gradually reduced to 0.44 mA cm^{-2}, which is approximately 75 % at the initial. This indicates that the FTO/Ti-Fe_2O_3 photoanode shows moderate photocurrent stability in a long-term experiment.

2.4 Conclusions

Ti-Fe_2O_3 particulate films were prepared on FTO-coated glass via a hydrothermal method in the presence of $TiCl_4$ with the assistance of two-step annealing under two different conditions: air calcination at 873 K and subsequent annealing under argon at 473 K. PEC property testing revealed an increase in the photocurrent response of FTO/Ti-Fe_2O_3 after the

two-step annealing. The two-step annealed sample with optimized Ti doping exhibited a photocurrent density of 0.55 mA cm^{-2} at 1.50 V vs. RHE, which was approximately three times higher than that of FTO/Ti-Fe_2O_3 calcined in air. The optimized Ti doping for the highest photocurrent density was 150 μL (Ti-150), which had a Ti/Fe ratio of 0.03–0.07, as confirmed by SEM–EDS and XRF analysis.

SEM observations confirmed that the two-step annealing did not influence the morphology and particle size of Ti-Fe_2O_3 on the FTO substrate. The XRD analysis also suggested that there was no structural change due to additional annealing under argon at 473 K. In the case of optical properties, no significant change in the bandgap energy was observed after air and two-step annealing. However, the two-step annealed sample exhibited a higher absorption in the NIR region than that of the sample calcined in air, implying a high electron concentration.

The increased photocurrent density of the Ti-Fe_2O_3 photoanodes is attributed to the enhanced donor density by additional annealing in argon at 473 K. The increased electrical conductivity was also confirmed by four-point probe resistivity measurements. Importantly, the PEC properties of FTO/Ti-Fe_2O_3 were improved by the two-step annealing treatment because of the simultaneous increase in the electron density and electrical conductivity of the Ti^{4+}-doped hematite particles. It is concluded that the synergetic effect of the two-step annealing and Ti^{4+} doping increased the PEC performance of FTO/Ti-Fe_2O_3 for water oxidation under one-sun illumination.

References

1. Amano, F., Ohtani, B. & Yoshida, H. Role of Doped Titanium Species in The Enhanced Photoelectrochemical Properties of Iron Oxide Films: Comparison between Water Oxidation and Iodide Ion Oxidation. *J. Electroanal. Chem.* **766**, 100–106 (2016).

2. Gurudayal, G. *et al.* Improving The Efficiency of Hematite Nanorods for Photoelectrochemical Water Splitting by Doping with Manganese. *ACS Appl. Mater. Interfaces* **6**, 5852–5859 (2014).

3. Ling, Y., Wang, G., Wheeler, D. A., Zhang, J. Z. & Li, Y. Sn-Doped Hematite Nanostructures for Photoelectrochemical Water Splitting. *Nano Lett.* **11**, 2119–2125 (2011).

4. Ahmed, M. G. *et al.* A Facile Surface Passivation of Hematite Photoanodes with TiO_2 Overlayers for Efficient Solar Water Splitting. *ACS Appl. Mater. Interfaces* **7**, 24053–24062 (2015).

5. Rahman, G. & Joo, O. S. Photoelectrochemical Water Splitting at Nanostructured α-Fe_2O_3 Electrodes. *Int. J. Hydrogen Energy* **37**, 13989–13997 (2012).

6. Klahr, B., Gimenez, S., Fabregat-Santiago, F., Hamann, T. & Bisquert, J. Water Oxidation at Hematite Photoelectrodes: The Role of Surface States. *J. Am. Chem. Soc.* **134**, 4294–4302 (2012).

7. Kraushofer, F. *et al.* Atomic-Scale Structure of The Hematite α-Fe_2O_3(11-02) 'r-Cut' surface. *J. Phys. Chem. C* **122**, 1657–1669 (2018).

8. Najaf, Z. *et al.* Recent Trends in Development of Hematite (α-Fe_2O_3) as An Efficient Photoanode for Enhancement of Photoelectrochemical Hydrogen Production by Solar Water Splitting. *Int. J. Hydrogen Energy* 1–24 (2020)

doi:10.1016/j.ijhydene.2020.07.111.

9. Warren, S. C. *et al.* Identifying Champion Nanostructures for Solar Water-Splitting. *Nat. Mater.* **12**, 842–849 (2013).

10. Phuan, Y. W., Ong, W. J., Chong, M. N. & Ocon, J. D. Prospects of Electrochemically Synthesized Hematite Photoanodes for Photoelectrochemical Water Splitting: A Review. *J. Photochem. Photobiol. C Photochem. Rev.* **33**, 54–82 (2017).

11. Chae, S. Y., Rahman, G. & Joo, O. shim. Elucidation of The Structural and Charge Separation Properties of Titanium-Doped Hematite Films Deposited by Electrospray Method for Photoelectrochemical Water Oxidation. *Electrochim. Acta* **297**, 784–793 (2019).

12. Cao, Z. *et al.* Synthesis and Characterization of Sn-Doped Hematite as Visible Light Photocatalyst. *Mater. Res. Bull.* **77**, 41–47 (2016).

13. Liu, Y., Yu, Y. X. & Zhang, W. De. Photoelectrochemical Properties of Ni-Doped Fe_2O_3 Thin Films Prepared by Electrodeposition. *Electrochim. Acta* **59**, 121–127 (2012).

14. Huang, J., Hu, G., Ding, Y., Pang, M. & Ma, B. Mn-Doping and NiFe Layered Double Hydroxide Coating: Effective Approaches to Enhancing The Performance of α-Fe_2O_3 in Photoelectrochemical Water Oxidation. *J. Catal.* **340**, 261–269 (2016).

15. Cesar, I., Kay, A., Martinez, J. A. G. & Grätzel, M. Translucent Thin Film Fe_2O_3 Photoanodes for Efficient Water Splitting by Sunlight: Nanostructure-Directing Effect of Si-Doping. *J. Am. Chem. Soc.* **128**, 4582–4583 (2006).

16. Amano, F., Tosaki, R., Sato, K. & Higuchi, Y. Effects of Donor Doping and Acceptor Doping on Rutile TiO_2 Particles for Photocatalytic O_2 Evolution by Water Oxidation. *J. Solid State Chem.* **258**, 79–85 (2018).

17. Amano, F., Nakata, M., Vequizo, J. J. M. & Yamakata, A. Enhanced Visible Light Response of TiO_2 Codoped with Cr and Ta Photocatalysts by Electron Doping. *ACS Appl. Energy Mater.* **2**, 3274–3282 (2019).

18. Mir, J. F., Rubab, S. & Shah, M. A. Photo-electrochemical Ability of Iron Oxide Nanoflowers Fabricated Via Electrochemical Anodization. *Chem. Phys. Lett.* **741**, 137088 (2020).

19. Wu, Q. *et al.* Enhanced Interface Charge Transfer Via n-n WO_3/Ti–Fe_2O_3 Heterojunction Formation For Water Splitting. *J. Alloys Compd.* **803**, 1105–1111 (2019).

20. Chen, Y. C., Kuo, C. L. & Hsu, Y. K. Facile Preparation of Zn-Doped Hematite Thin Film as Photocathode for Solar Hydrogen Generation. *J. Alloys Compd.* **768**, 810–816 (2018).

21. Cesar, I., Sivula, K., Kay, A., Zboril, R. & Grätzel, M. Influence of Feature Size, Film Thickness, and Silicon Doping on The Performance of Nanostructured Hematite Photoanodes for Solar Water Splitting. *J. Phys. Chem. C* **113**, 772–782 (2009).

22. Pandiadurai, K., Mani, G. K., Shankar, P. & Rayappan, J. B. B. ZnO Nanospheres to Nanorods - Morphology Transition Via Fe-Doping. *Superlattices Microstruct.* **62**, 39–46 (2013).

23. Xu, J., Fujitsuka, M., Kim, S., Wang, Z. & Majima, T. Unprecedented Effect of CO_2 Calcination Atmosphere on Photocatalytic H_2 Production Activity from Water using g-C_3N_4 Synthesized From Triazole Polymerization. *Appl. Catal. B Environ.* **241**, 141–148 (2019).

24. Yu, J. & Wang, B. Effect of Calcination Temperature on Morphology and Photoelectrochemical Properties of Anodized Titanium Dioxide Nanotube Arrays. *Appl.*

Catal. B Environ. **94**, 295–302 (2010).

25. Rosa Silva, E., Curi, M., Furtado, J. G., Ferraz, H. C. & Secchi, A. R. The Effect of Calcination Atmosphere on Structural Properties of Y-doped $SrTiO_3$ Perovskite Anode for SOFC Prepared by Solid-State Reaction. *Ceram. Int.* **45**, 9761–9770 (2019).

26. Sienkiewicz, A. *et al.* Effect of Calcination on The Photocatalytic Activity and Stability of TiO_2 Photocatalysts Modified with APTES. *J. Environ. Chem. Eng.* **9**, 104794 (2021).

27. Kim, J. Y. *et al.* Single-Crystalline, Wormlike Hematite Photoanodes for Efficient Solar Water Splitting. *Sci. Rep.* **3**, 1–8 (2013).

28. Amano, F., Mukohara, H. & Shintani, A. Rutile Titania Particulate Photoelectrodes Fabricated by Two-Step Annealing of Titania Nanotube Arrays. *J. Electrochem. Soc.* **165**, H3164–H3169 (2018).

29. Makimizu, Y. *et al.* Activation of α-Fe_2O_3 for Photoelectrochemical Water Splitting Strongly Enhanced by Low Temperature Annealing in Low Oxygen Containing Ambient. *Chem. - A Eur. J.* **26**, 2685–2692 (2020).

30. Amano, F., Nakata, M., Yamamoto, A. & Tanaka, T. Effect of Ti^{3+} Ions and Conduction Band Electrons on Photocatalytic And Photoelectrochemical Activity of Rutile Titania for Water Oxidation. *J. Phys. Chem. C* **120**, 6467–6474 (2016).

31. Tamaki, Y., Hara, K., Katoh, R., Tachiya, M. & Furube, A. Femtosecond Visible-to-IR Spectroscopy of TiO_2 Nanocrystalline Films: Elucidation of The Electron Mobility Before Deep Trapping. *J. Phys. Chem. C* **113**, 11741–11746 (2009).

32. Fu, Z. *et al.* Highly photoactive Ti-Doped α-Fe_2O_3 Nanorod Arrays Photoanode Prepared by A Hydrothermal Method for Photoelectrochemical Water Splitting. *Electrochim. Acta* **129**, 358–363 (2014).

33. Kim, S. *et al.* A Systematic Study of Post-Activation Temperature Dependence on Photoelectrochemical Water Splitting of One-Step Synthesized FeOOH CF photoanodes with Erratically Loaded ZrO_2. *Sustain. Energy Fuels* **5**, 3414–3427 (2021).

34. Gujral, S. S., Simonov, A. N., Higashi, M., Abe, R. & Spiccia, L. Optimization of Titania Post-Necking Treatment of TaON Photoanodes to Enhance Water-Oxidation Activity under Visible-Light Irradiation. *ChemElectroChem* **2**, 1270–1278 (2015).

35. Zhang, N. *et al.* Design Principles for Construction of Charge Transport Channels in Particle-Assembled Water-Splitting Photoelectrodes. *ACS Sustain. Chem. Eng.* **7**, 10509–10515 (2019).

36. Cao, D. *et al.* Mechanism Investigation of the Postnecking Treatment to WO_3 Photoelectrodes. *ACS Appl. Energy Mater.* **1**, 4670–4677 (2018).

37. Li, Y. *et al.* Interface Engineering Z-scheme Ti-Fe_2O_3/In_2O_3 Photoanode for Highly Efficient Photoelectrochemical Water Splitting. *Appl. Catal. B Environ.* **290**, 120058 (2021).

Chapter 3

Chapter 3. Effect of conductive substrate for Ti-doped Fe_2O_3 photoanodes

3.1 Introduction

Photoelectrochemical (PEC) water splitting generally involves the oxygen evolution reaction (OER) at the photoanode and the hydrogen evolution reaction (HER) at the photocathode/cathode. Due to its abundant nature, Fe_2O_3 has been extensively investigated as a photoanode for the PEC-OER. Additionally, the band gap energy of Fe_2O_3 in the range of 2.0–2.2 eV is categorized as visible-light-sensitive metal oxides.[1] The use of a visible light irradiation source is crucial for effective PEC reactions in practical applications because it dominates the solar spectrum absorbed on the Earth's surface.[2] However, Fe_2O_3 has a major drawback owing to its low PEC performance, mostly because of its low photon absorptivity near its band edge owing to its indirect band gap.[3] Light absorption can be enhanced by increasing the thickness of the photoelectrode layer.[4–6] However, the specific thickness diminishes the PEC activity when it reaches a value greater than the carrier diffusion length. In an n-type photoanode system, only the holes generated close to the semiconductor–electrolyte interface contributes to the water oxidation reaction. In contrast, electrons, as the majority of charge carriers produced farther from the semiconductor–substrate interface than their diffusion length, cannot reach the conductive substrate.[5] The short carrier-diffusion lengths in Fe_2O_3 lead to the recombination of photogenerated electrons and holes before they reach the semiconductor–electrolyte, and semiconductor–substrate interfaces.[7,8]

To address this limitation, several concepts have been adopted to control the properties of Fe_2O_3, including its morphology, particle size, and thickness, to accelerate its PEC efficiency. Grätzel et al. developed a dendritic nanostructure of Fe_2O_3 that shortened the hole distance to

reach the interface with high light absorption.[2] Moreover, Fe_2O_3 has been synthesized with controlled thickness by atmospheric pressure chemical vapor deposition (APCVD) to achieve an increased donor density (N_D).[9] The electron diffusion length also determines the optimum thickness of Fe_2O_3 films with respect to their light absorption properties. When the electrical conductivity is low, a thick Fe_2O_3 film results in low PEC efficiency because of the long travel distance of the photoexcited electrons.

The use of conductive substrates with a larger surface area could be considered to achieve higher PEC activity in the fabrication of Fe_2O_3 photoanodes. To date, Fe_2O_3 has been frequently deposited on various conductive substrates such as glass coated with fluorine-doped tin oxide (FTO) and indium tin oxide (ITO) glass.[10–19] These conventional two-dimensional (2D) conductive substrates exhibit low PEC activity for solar-to-chemical conversion applications owing to their small surface areas. Alternative conductive substrates include three-dimensional (3D) microporous structures, such as carbon microfiber felt and sintered titanium microfiber felt.[4,5] Previous studies have reported that Ti microfiber felt exhibits a macroporous and high porosity (66.7%) structure, which is essential for mass transportation, and a higher calculated specific surface area (444 $cm^2\ g^{-1}$) than that of 2D Ti sheet conductive substrates (45 $cm^2\ g^{-1}$).[4,20] This property allows for a larger semiconductor–substrate interface and a thinner semiconductor layer at the same loading.[4] More importantly, a larger surface area increases the loading of active semiconductor materials for PEC reactions.[21]

An n-type oxide photoanode, for example, WO_3 has been prepared on 3D Ti felt.[22] The photocurrent density of WO_3 is higher than that of conventional 2D conductive substrates. Abe et al. fabricated a p-type $CuInS_2$ photocathode on 3D carbon felt.[5] This modified photocathode exhibited a higher cathodic current density compared to that of a conventional 2D Mo metal substrate. P-type Cu_2O photocathodes have been previously fabricated on 3D Ti felt for methyl viologen reduction.[4] A high photocurrent efficiency was obtained owing to the large

semiconductor–electrolyte, and semiconductor–substrate interfaces. Moreover, an increase in the loading amount and a thinner film layer generated high PEC activity, which was attributed to sufficient light absorption and a shorter carrier transport distance, respectively. Earlier studies focused on the preparation of WO_3 and TiO_2 photoanodes on 3D-structured titanium web substrates for PEC applications. Nevertheless, a comparison of their PEC performance with 2D conventional substrates and specifically for Fe_2O_3 electrodes has not been performed.[23,24] Recently, Sivula et al. investigated Fe_2O_3 photoanodes on a 3D transparent conductive substrate by coating SiO_2 fiber felts with an FTO layer. However, further modification is required for preparation using consecutive thermal annealing and APCVD.[25]

Even though the fabrication of photoelectrodes on 3D conductive substrates to improve their PEC performance has been described in numerous studies, few have considered the use of Ti microfibers for the fabrication of Fe_2O_3 photoanodes. This study aims to investigate the PEC activity of Fe_2O_3 on 3D conductive substrates. For comparison, FTO-coated glass and Ti sheets were used as conventional 2D conductive substrates. Ti-doped Fe_2O_3 films were prepared with different loading amounts and thicknesses and evaluated their PEC properties for the OER.

3.2 Experimental section

3.2.1 Preparation of Ti-felt/Ti-Fe_2O_3

Fe_2O_3 photoanodes on FTO-coated glass (thickness of 1.8 mm, AGC Fabritech Co., Ltd., Japan) were fabricated by a hydrothermal reaction with Ti doping and two-step annealing.[26] Ti microfiber felt (thickness of 0.1 mm; porosity of 66.7%; Nikko Techno, Japan) and Ti sheet (thickness of 0.1 mm; Nilaco, Japan) were also used as conductive substrates in this study. Iron (III) nitrate nonahydrate (99.9%, Wako Pure Chemical, Japan) and 1 mol L^{-1} sodium nitrate (99.9%, Wako Pure Chemical, Japan) were dissolved in 20 mL of deionized water under

constant stirring to prepare an aqueous solution of 0.1 mol L^{-1} $Fe(NO_3)_3$ and 1 mol L^{-1} $NaNO_3$. Titanium (IV) chloride ($TiCl_4$, 16–17% as Ti, Wako Pure Chemical, Japan) in ethanol solution (Ti/Fe ratio in feed, ~0.4%) was added to the aqueous solution. The precursor mixture was then incorporated into a stainless-steel, Teflon-lined autoclave by placing the substrate vertically in the vessel. Hydrothermal treatment was performed at 120 °C for 10 h. Once the reaction was complete, the electrodes were sequentially washed with ethanol and deionized water, then dried at 100 °C. The resulting product was calcined at 550 °C for 2 h in air, followed by annealing at 300 °C for 2 h under an argon atmosphere. This two-step annealing in air and argon atmospheres increased the photocurrent density because of the simultaneous improvement in donor density (N_D) and electrical conductivity.[26] The Ti-doped Fe_2O_3 samples on the Ti felt, FTO glass, and Ti sheet substrates are denoted as Ti-felt/Ti-Fe_2O_3, FTO/Ti-Fe_2O_3, and Ti-sheet/Ti-Fe_2O_3, respectively.

3.2.2 Characterization

Field-emission scanning electron microscopy (FE-SEM, JSM–7500 F microscope, JEOL, Japan) at an acceleration voltage of 5.0 kV was used to observe the morphology, particle diameter, and thickness of the photoanodes. The diffraction pattern of the samples was analyzed by X-ray diffraction (XRD, SmartLab, Rigaku, Japan) with Cu Kα radiation at 40 kV and 30 mA. The step and scan measurements were set at 0.01° and 5°/min, respectively. Raman spectra were analyzed with a laser excitation source of 532 nm using a confocal Raman microscope (XploRA PLUS, Horiba, Japan). The optical properties of the photoanodes were investigated using a UV–Vis diffuse reflectance spectrophotometer (UV–2600, Shimadzu, Japan). The oxidation state of the chemical composition was determined by X-ray photoelectron spectroscopy (XPS, JPS-9010 MX, JEOL, Japan) with irradiation of Mg Kα. The XPS profiles were normalized to the O 1s at 530.0 eV.

3.2.3 Photoelectrochemical measurements

PEC properties were measured using a potentiostat (VersaSTAT 3, Princeton Applied Research). The conventional three-electrodes system in a glass cell was used to evaluate PEC properties in a 1 mol L^{-1} NaOH (pH = 13.6) solution with a reference electrode of Hg/HgO, a counter electrode of platinum wire, and a working electrode with an irradiated area of 1.0 cm^2 under solar simulator photoirradiation (XES-40S1, SAN-EI Electric, Japan) (AM 1.5G, I_0 = 100 mW cm^{-2}). Linear scan voltammetry (LSV) was performed at an applied potential in the range of −0.5 to +0.7 V vs. Hg/HgO with a scan rate of 0.05 V s^{-1}. The Nernst equation was used to convert the potential obtained from the measurement into the RHE as follows:

$$E\ [\text{V vs. RHE}] = E\ [\text{V vs. Hg/HgO}] + 0.0591 \times \text{pH} + E^{\circ}(\text{Hg/HgO}) \quad (3.1)$$

where E°(Hg/HgO) is +0.118 V vs. the standard hydrogen electrode (SHE). The chronoamperometry measurement was conducted at 1.23 V vs. RHE for 900 s, with irradiation starting from 300 s to 600 s. Furthermore, the stability of the photocurrent was examined at 1.23 V vs. RHE for 3 h under one-sun irradiation. The influence of incident light intensities (I_0) ranging from 1.5 to 41 mW cm^{-2} was observed by using a light-emitting diode (LED, peak wavelength 385 nm, width ~10 nm). The incident light intensity of the LED lamp was adjusted using a DC power supply (PMX18–2A, Kikusui Electronics, Japan) and recorded using an optical power meter (3664, Hioki, Japan). Additionally, the incident photon-to-current conversion efficiency (IPCE) action spectra were analyzed using a 300-W xenon lamp (MAX-303, Asahi Spectra, Japan) with bandpass filters. The IPCE was quantified from the photocurrent density (J_{photo}) using the following formula:

$$\text{IPCE} = \frac{J_{\text{photo}}}{I_0} \times \frac{1240}{\text{wavelength [nm]}} \quad (3.2)$$

N_D was evaluated by Mott–Schottky measurements at a frequency of 1 kHz with an applied sinusoidal amplitude of 10 mV in the dark. The capacitance of the space charge layer (C) was determined from the imaginary part of the electrochemical impedance, which represented a

series capacitor–resistor model. N_D and the flat-band potential (E_{fb}) were calculated from the C^{-2} versus applied potential (E) plot using the Mott–Schottky formula, assuming a flat semiconductor model, as follows:

$$\frac{1}{C^2} = \frac{2}{q\varepsilon\varepsilon_0 N_D}\left(E - E_{fb} - \frac{kT}{q}\right) \quad (3.3)$$

where q, ε, ε_0, k, and T are the elementary electric charge, dielectric constant, the permittivity of vacuum, Boltzmann's constant, and temperature, respectively. The dielectric constant of Fe_2O_3 is 12.

The PEC's water splitting was performed in an H-type glass reactor. The anode and cathode were separated using a Fumapem FAA-3-50 anion exchange membrane (Fumatech, Germany). The PEC-OER was observed in a 1 mol L^{-1} NaOH solution under UV irradiation from an LED (peak wavelength 385 nm, width ~10 nm). The I_0 value was established at 40 mW cm^{-2} on electrodes with a geometrical area of 1.0 cm^2. The produced O_2 in the gas phase was quantified by gas chromatography (490 Micro GC, Agilent Technologies).

3.3 Results and discussion

3.3.1 Loading amount of Ti-Fe_2O_3 on different conductive substrates

Photographs of the different conductive substrates are shown in Figure 3.1. 3D Ti felt was used to evaluate the PEC properties of Ti-doped Fe_2O_3 (Figure 3.1A). For comparison, FTO-coated glass was employed as a 2D conductive substrate (Figure 3.1B). Additionally, a Ti-doped Fe_2O_3 photoanode was prepared on another 2D conductive substrate, a Ti sheet (Figure 3.1C). The Fe_2O_3 layers were visually observed on the surfaces of all substrates with similar reddish colors (Figures 3.1D–F).

Table 1 summarizes the loading amounts of the Fe_2O_3 layers on the three conductive substrates. On a 12-cm^2 area of the substrate, the lowest amount (1.80 mg) was loaded on the

FTO glass. In contrast, the loading amount per geometric area on the Ti felt (10.1 mg) was approximately five times higher than that on the FTO glass. Among the 2D conductive substrates, the Ti sheet was loaded with 4.60 mg of the Fe_2O_3 layer, which was more than that on the FTO glass. This is because both sides of the Ti sheet contained a Fe_2O_3 layer. Fe_2O_3 was loaded only on the conductive surface of the FTO glass. This result suggests that the larger specific surface area of the 3D macroporous structure enables a higher amount of Fe_2O_3 to be loaded onto the Ti felt.

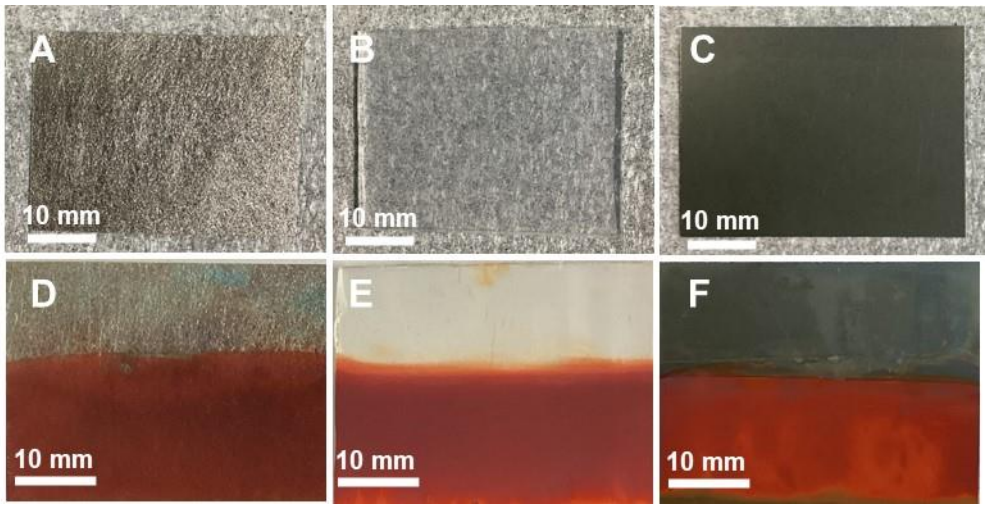

Figure 3.1: Photographs of (A) Ti felt, (B) FTO glass, (C) Ti sheet, (D) Ti-felt/Ti-Fe_2O_3, (E) FTO/Ti-Fe_2O_3, and (F) Ti-sheet/Ti-Fe_2O_3 with a geometric area of 12 cm^2.

Figure 3.2 shows the SEM images of the Ti-doped Fe_2O_3 layers on the Ti felt. At low magnification, the Ti felt exhibited an interconnected fibrous network with a porous structure (Figure 3.2A). The Fe_2O_3 particles were layered on all surfaces of the Ti microfibers in the 3D macroporous felt. Interestingly, the Fe_2O_3 layer was not only attached to the substrate surface but also to the interior of the Ti fiber network. This phenomenon enables the Ti felt to have a high loading amount because of its larger surface area.

Table 3.1. Loading amount of Fe_2O_3 prepared on the 2D- and 3D-conductive substrates with a geometric area of 12 cm^2

Photoanodes	Weight of conductive substrates		Fe_2O_3 loading / mg
	Before loading / mg	After loading / mg	
Ti-felt/Ti-Fe_2O_3	208.0	218.1	10.1
FTO/Ti-Fe_2O_3	5572.2	5574.0	1.80
Ti-sheet/Ti-Fe_2O_3	537.1	541.7	4.60

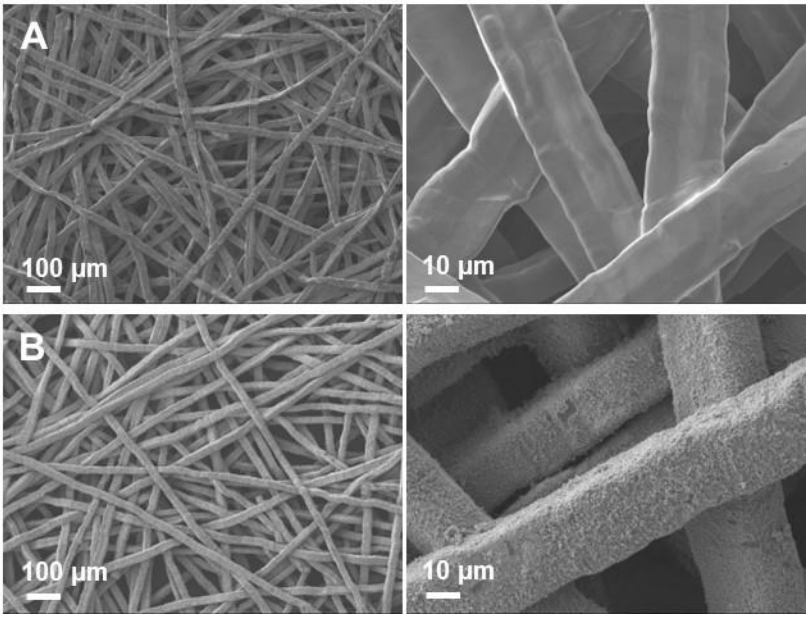

Figure 3.2: SEM images of (A) Ti felt and (B) Ti-felt/Ti-Fe_2O_3.

3.3.2 Characterization of Ti-Fe_2O_3 photoanodes

SEM images of the top and cross-sectional side views of the Ti-doped Fe_2O_3 on different conductive substrates were analyzed in Figure 3.3. The top-view images show that all morphologies of Fe_2O_3 were similar in the spherical aggregates at higher magnification. However, the diameters of the Fe_2O_3 particles for the different conductive substrates were different (Figure 3.4). Fe_2O_3 particles with diameters less than 70 nm were deposited on the surface of the Ti felt. For FTO/Ti-Fe_2O_3, the particle size of Fe_2O_3 was estimated to be in the

range of 60–80 nm. The diameters of the Fe_2O_3 particles on the Ti sheets were approximately 100 nm.

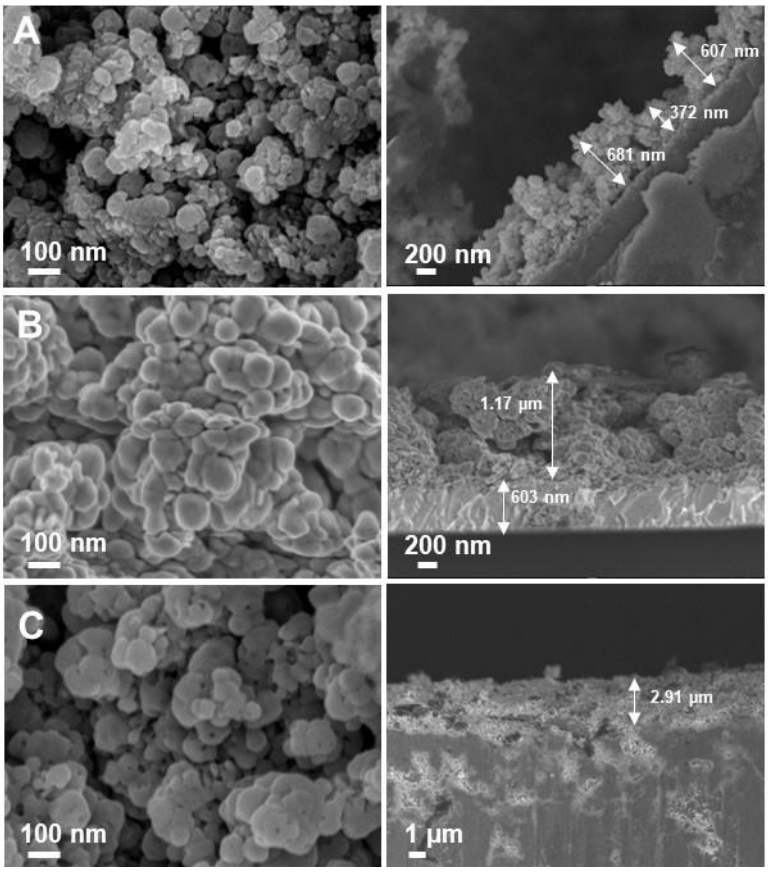

Figure 3.3: SEM images of (A) Ti-felt/Ti-Fe_2O_3, (B) FTO/Ti-Fe_2O_3, and (C) Ti-sheet/Ti-Fe_2O_3; top view and cross-sectional side view.

In the case of cross-sectional side view images, the thickness of the Fe_2O_3 layer on the Ti felt was ~0.6 µm. The distribution of the Fe_2O_3 thickness varied in different observation areas, indicating that the Fe_2O_3 layer deposited by the hydrothermal method was not uniform. For FTO/Ti-Fe_2O_3, the thickness of Fe_2O_3 on the FTO glass was about 1 µm. In contrast, the Fe_2O_3 film had the greatest thickness on the Ti sheets (> 2 µm). Although the distribution of the Fe_2O_3 thickness was not homogeneous over the entire surface of the Ti felt, the film became thinner on the 3D macroporous substrates than on the conventional 2D substrates.

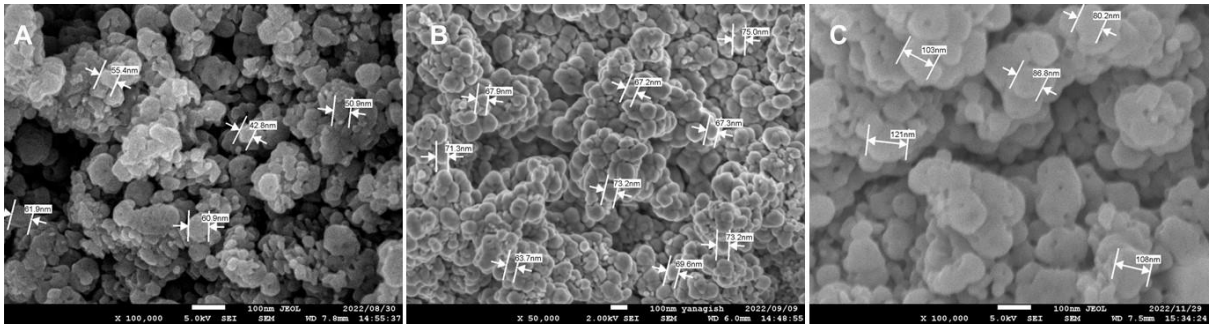

Figure 3.4: SEM images of top view (A) Ti-felt/Ti-Fe_2O_3, (B) FTO/Ti-Fe_2O_3, and (C) Ti-sheet/Ti-Fe_2O_3 with particle size information.

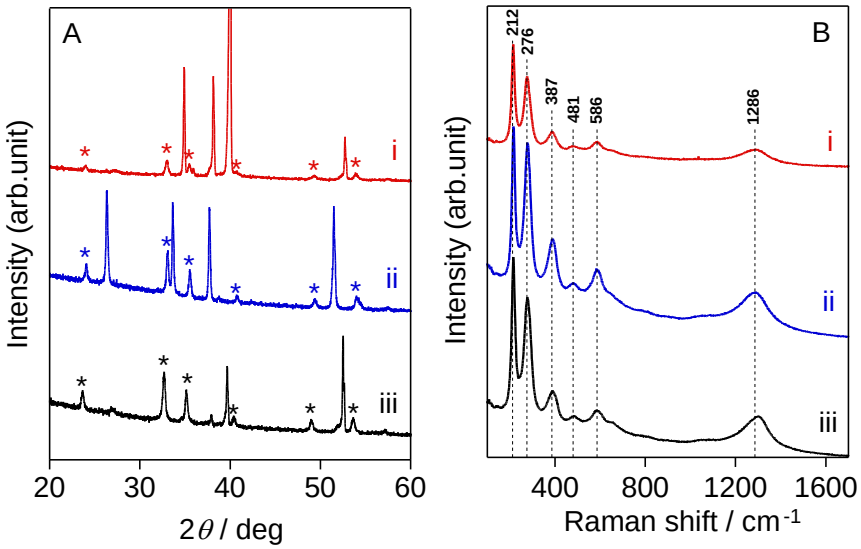

Figure 3.4: (A) X-ray diffraction patterns of (i) Ti-felt/Ti-Fe_2O_3, (ii) FTO/Ti-Fe_2O_3, and (iii) Ti-sheet/Ti-Fe_2O_3. The asterisk signs correspond to the characteristic of α-Fe_2O_3 (PDF standard no. 01-089-0596). (B) Raman spectra of Ti-felt/Ti-Fe_2O_3 and FTO/Ti-Fe_2O_3.

The diffraction patterns of Ti-doped Fe_2O_3 on different conductive substrates are shown in Figure.3.4A. The standard of the diffraction patterns for α-Fe_2O_3, α-Ti, and SnO_2 are shown in Figure 3.5. For Ti-felt/Ti-Fe_2O_3 and Ti-sheet/Ti-Fe_2O_3, the four primary peaks at 34.9°, 38.1°, 39.9°, and 52.7° were indexed to α–Ti (PDF 00-044-1294). For FTO/Ti-Fe_2O_3, the peaks at 26.3°, 33.6°, 37.7°, and 51.4° are ascribed to SnO_2 (PDF 01-077-0452). However, several peaks

at 24.0°, 33.0°, 35.5°, 40.8°, 49.3°, and 54.1° were consistent with trigonal α-Fe_2O_3 (R-3c(167), PDF 01-089-0596). The diffraction patterns of Fe_2O_3 were similar for the different conductive substrates. Next, the vibrational properties of Fe_2O_3 were assessed using Raman spectroscopy (Figure 3.4B). The vibrational intensities at 212, 276, 387, 481, 586, and 1286 cm^{-1} were attributed to hematite (α-Fe_2O_3).[26] No additional band intensities were observed, indicating the absence of impurities in the Ti-Fe_2O_3 films.

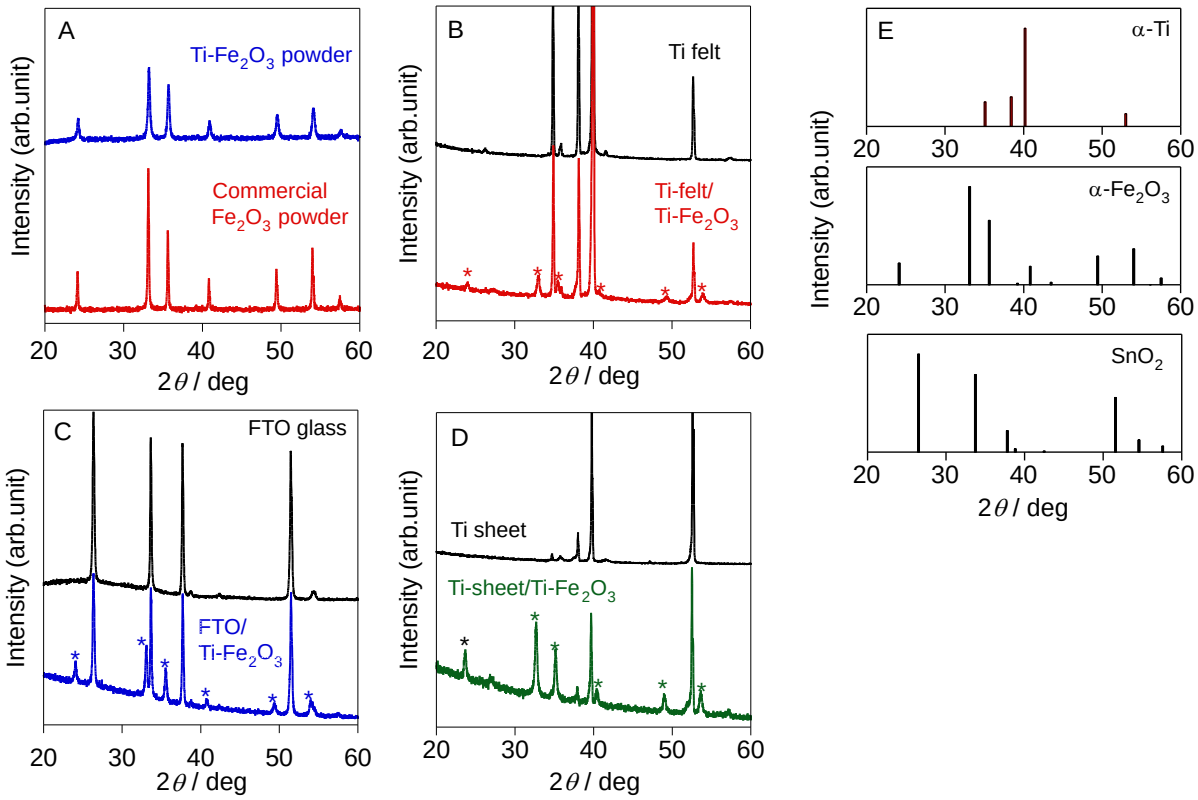

Figure 3.5: X-ray diffraction patterns of (A) Ti-Fe_2O_3 powder and commercial Fe_2O_3 (High Purity Chemical Laboratory, Japan), (B) Ti felt and Ti-felt/Ti-Fe_2O_3, (C) FTO glass and FTO/Ti-Fe_2O_3, (D) Ti sheet and Ti-sheet/Ti-Fe_2O_3, and (E) standard data; α-Ti (no. 00-044-1294), α-Fe_2O_3 (no. 01-089-0596), and SnO_2 (no. 01-077-0452).

The optical properties of the Ti-doped Fe_2O_3 prepared on different conductive substrates were analyzed by UV–visible diffuse reflectance spectroscopy (DRS) at 220–1400 nm (Figure 3.6). Each sample with different conductive substrates exhibited different photoabsorption at 220–600 nm. Among the samples, Ti-felt/Ti-Fe_2O_3 showed the highest photoabsorption. This high photoabsorption was attributed to the large amount of Fe_2O_3 loaded on the Ti felt. The 3D-conductive substrates generated Fe_2O_3 layers with higher photoabsorption. In contrast, the photoabsorption of FTO/Ti–Fe_2O_3 was the lowest.

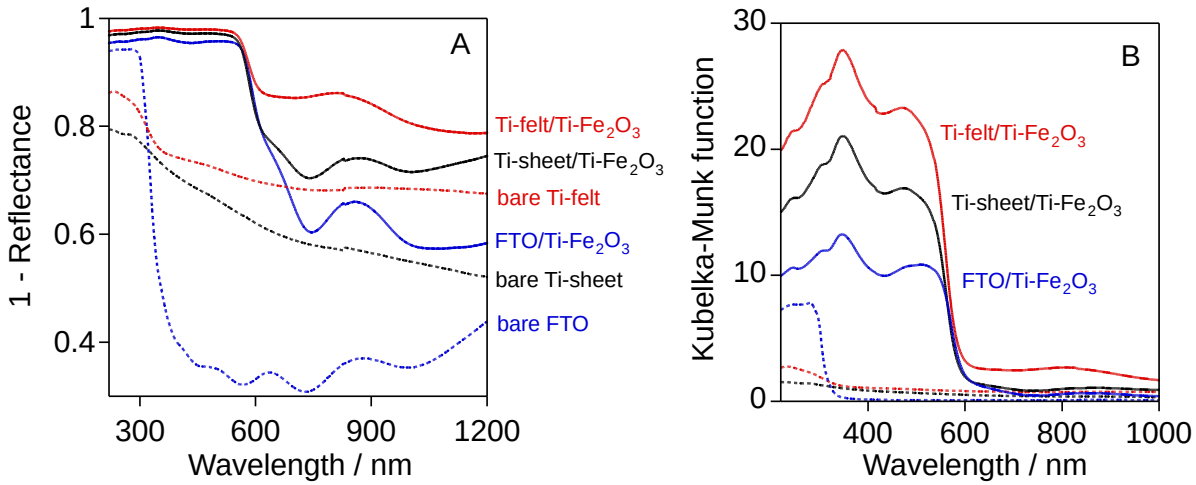

Figure 3.6: (A) Diffuse reflectance UV–visible–NIR spectra of FTO/Ti-Fe_2O_3, Ti-felt/Ti-Fe_2O_3, and Ti-sheet/Ti-Fe_2O_3; (A) 1 − Reflectance and (B) Kubelka-Munk function. The dashed lines represent bare substrates.

Next, the optical band gaps of Fe_2O_3 on different conductive substrates were analyzed. The relationships between $(\alpha h\nu)^{0.5}$ and $h\nu$ are plotted in Figure 3.7. The band gap energies of Fe_2O_3 on the Ti felt, FTO glass, and Ti sheet substrates were 2.11, 2.08, and 2.11 eV, respectively. This result is consistent with the bandgap energy of Fe_2O_3 reported in previous studies.[1,26] Different conductive substrates did not significantly affect the bandgap energy of Fe_2O_3.

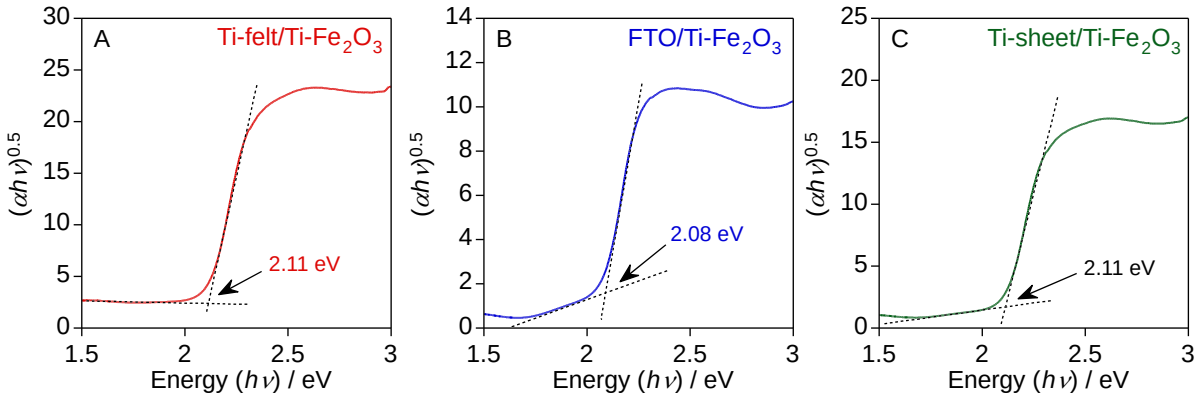

Figure 3.7: Tauc plots of (A) Ti-felt/Ti-Fe_2O_3, (B) FTO/Ti-Fe_2O_3, and (C) Ti-sheet/Ti-Fe_2O_3.

XPS measurements were performed to analyze the oxidation state of Ti-doped Fe_2O_3 prepared on Ti- and FTO-coated glass substrates (Figure 3.8). The binding energies of 710.8 eV and 724.2 eV were assigned to the Fe $2p_{3/2}$ and $2p_{1/2}$ of Fe^{3+}, respectively. In the case of Ti 2p, two primary peaks at 458.1 eV ($2p_{3/2}$) and 463.9 eV ($2p_{3/2}$) correspond to the typical Ti^{4+}, suggesting that the doped species is Ti^{4+}. The O 1s peak at a binding energy of 530 eV corresponds to lattice oxygen (O^{2-}). A notable discrepancy attributed to hydroxyl groups was observed at 531.7 eV. Hydroxyl groups may be formed through the consumption of oxygen vacancies by H_2O, as explained by the following equation:[27]

$$V_O^{\bullet\bullet} + H_2O + O_O^{\times} \rightarrow 2(OH)_O^{\bullet} \qquad (3.4)$$

where $(OH)_O^{\bullet}$ is a hydroxyl group at the oxygen lattice position. The intensities of the hydroxyl groups in Ti-felt/Ti-Fe_2O_3 are lower than those in FTO/Ti-Fe_2O_3 and Ti-sheet/Ti-Fe_2O_3. This result indicates that Ti-felt/Ti-Fe_2O_3 presented the lowest density of oxygen vacancies during the two-step annealing process.

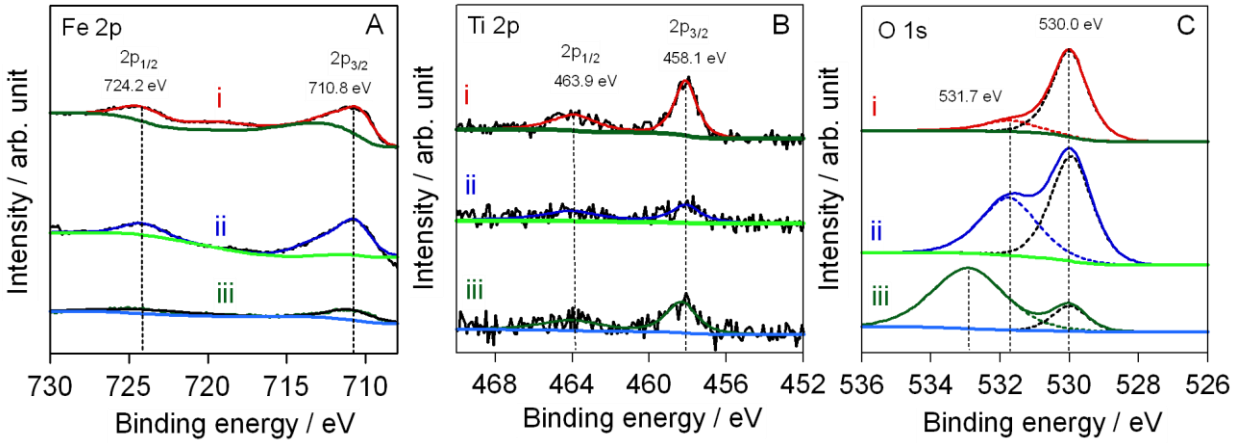

Figure 3.8: X-ray photoelectron spectra of (A) Fe 2p, (B) Ti 2p, and (C) O 1s of (i) Ti-felt/Ti-Fe_2O_3 (ii) FTO/Ti-Fe_2O_3 and (iii) Ti-sheet/Ti-Fe_2O_3. The spectra were normalized by O 1s at 530.0 eV.

3.3.3 Photoelectrochemical performance of Ti-Fe_2O_3 photoanodes

The PEC properties of Ti-felt/Ti-Fe_2O_3, FTO/Ti-Fe_2O_3, and Ti-sheet/Ti-Fe_2O_3 prepared under similar conditions were also evaluated. Figure 3.9A shows the LSV measurements in 1 mol L^{-1} NaOH (pH = ~13.6) under one-sun irradiation (100 mW cm^{-2}). Each conductive substrate produced a different photocurrent response in the Ti-doped Fe_2O_3 layers. The lowest photocurrent response was obtained for Ti-sheet/Ti-Fe_2O_3. J_{photo} of FTO/Ti-Fe_2O_3 was slightly higher than that of Ti-sheet/Ti-Fe_2O_3. The highest J_{photo} was observed for Ti-felt/Ti-Fe_2O_3, suggesting that the 3D macroporous Ti felt was important for improving the photocurrent response.

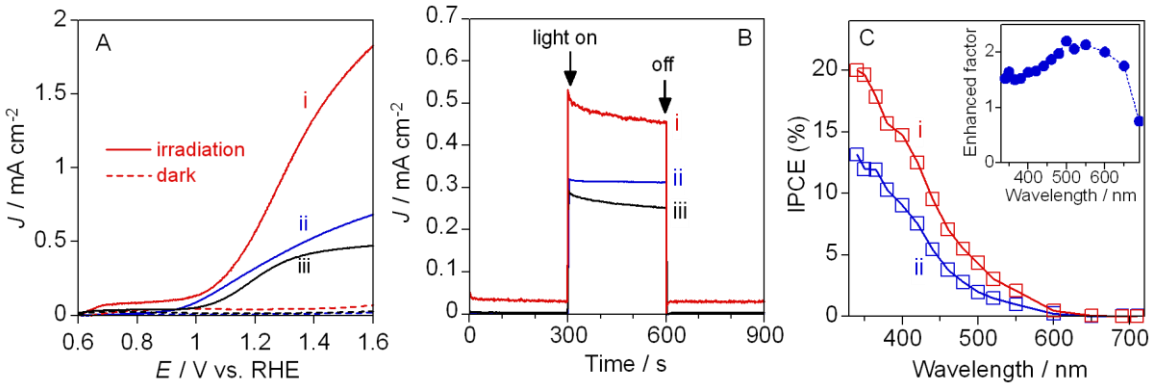

Figure 3.9: PEC properties in a 1 mol L^{-1} NaOH solution of (i) Ti-felt/Ti-Fe_2O_3, (ii) FTO/Ti-Fe_2O_3, and (iii) Ti-sheet/Ti-Fe_2O_3 under one-sun irradiation (I_0 = 100 mW cm^{-2}); (A) Current–potential curve. The dashed line indicates the current density in the dark. (B) Photocurrent response at 1.23 V vs. RHE under irradiation for 300–600 s. (C) IPCE curves at 1.23 V vs. RHE under light irradiation (λ, 340–710 nm). The IPCE value was quantified using J_{photo} after subtracting their dark current. Inset shows the increment factor for IPCE of Ti-felt/Ti-Fe_2O_3 compared to FTO/Ti-Fe_2O_3.

For a clearer evaluation, chronoamperometry was measured at 1.23 V vs. RHE (Figure 3.9B). The photocurrent densities for Ti-felt/Ti-Fe_2O_3, FTO/Ti-Fe_2O_3, and Ti-sheet/Ti-Fe_2O_3 were 0.43, 0.31, and 0.25 mA cm^{-2}, respectively. It is observed that the photocurrent response of the Fe_2O_3 prepared on the 3D-conductive substrate was higher than that on the 2D-conductive substrate. This result is partly ascribed to the higher amount of Fe_2O_3 loaded onto the Ti felt per unit geometric area. With a large loading, Fe_2O_3 sufficiently absorbed the light, which enhanced the PEC activity, as shown in the UV-visible DRS analysis (Figure 3.6). The moderate thickness of the Fe_2O_3 layer on the Ti felt is another factor that likely shortens the traveling distance of the photoexcited electrons. In contrast, the J_{photo} of Ti-sheet/Ti-Fe_2O_3 with a higher loading amount was slightly lower than that of FTO/Ti-Fe_2O_3. This is because of the very large thickness of Fe_2O_3 on the Ti sheet substrate owing to the higher loading amount; the recombination of charge carriers may easily occur because of the long travel distance. The

action spectra of the IPCE for Ti-felt/Ti-Fe_2O_3 and FTO/Ti-Fe_2O_3 were measured at 1.23 V vs. RHE in the wavelength range of 340–710 nm (Figure 3.9C). Both samples exhibit a similar trend of IPCE onset at approximately 600 nm, which appropriately matches the optical bandgap of Fe_2O_3 (~2.05 eV). The IPCE value of Ti-felt/Ti-Fe_2O_3 was higher than that of FTO/Ti-Fe_2O_3 owing to the increased photoabsorption of Fe_2O_3 on the Ti felt in the 340–600 nm range. The inset graph shows the increment factor for the photoabsorption of Ti-felt/Ti-Fe_2O_3 compared with that of FTO/Ti-Fe_2O_3. The increment factor in the visible region is slightly higher than that in the UV region. Fe_2O_3 on 3D-conductive substrates shows a good photoresponse under visible-light irradiation, even near its band edge.

3.3.4 Donor density of Ti-Fe_2O_3 photoanodes

The Mott–Schottky analysis was performed based on the capacitance of the space layer (C) with the assumption that the semiconductor used was ideal and flat.[8] Figure 3.10 shows the Mott–Schottky plot simulated using the inverse capacitance squared (C^{-2}) and applied potentials (V). E_{fb} and N_D were calculated from the x-intercepts and slopes. All the slopes were observed to be positive, indicating a semiconductor with n-type conductivity. The donor densities for Ti-felt/Ti-Fe_2O_3, FTO/Ti-Fe_2O_3, and Ti-sheet/Ti-Fe_2O_3 were 8.58×10^{21}, 8.39×10^{20}, and 2.44×10^{20} cm^{-3}, respectively (Table 3.2).

Table 3.2. Donor density (N_D) and flat-band potential (E_{fb}) measured by the Mott-Schottky analysis of Fe_2O_3 prepared on the 2D- and 3D-conductive substrates

Photoanodes	N_D / cm^{-3}	E_{fb} / V vs. RHE
Ti-felt/Ti-Fe_2O_3	8.58×10^{21}	0.17
FTO/Ti- Fe_2O_3	8.39×10^{20}	0.19
Ti-sheet/Ti- Fe_2O_3	2.44×10^{20}	0.26

Ti-felt/Ti-Fe_2O_3 exhibits the highest N_D. Because FTO/Ti-Fe_2O_3 is a 2D-conductive substrate, its N_D was slightly higher than that of Ti-sheet/Ti-Fe_2O_3. This result was in good agreement with the J_{photo} value obtained from LSV and chronoamperometry measurements. The increased electron concentration on the Ti-felt/Ti-Fe_2O_3 was partly attributed to the higher loading of Fe_2O_3 on the substrates per geometric area.

Table 3.3. The donor density (N_D) and flat-band potential (E_{fb}) measured by Mott-Schottky analysis of Ti-felt/non-doped Fe_2O_3, Ti-felt/Ti-Fe_2O_3 annealed only in the air (without two-step annealing), and Ti-felt/Ti-Fe_2O_3 with two-step annealing

Photoanodes	N_D / cm^{-3}	E_{fb} / V vs. RHE
Ti-felt/undoped Fe_2O_3(air)	6.70×10^{19}	0.26
Ti-felt/Ti-Fe_2O_3(air)	5.69×10^{20}	0.21
Ti-felt/Ti-Fe_2O_3(two-step)	8.58×10^{21}	0.17

Moreover, the donor densities of Ti-felt/undoped Fe_2O_3 and Ti-felt/Ti-Fe_2O_3 (air), which were prepared without a second Ar treatment were evaluated (Figure 3.11). As shown in Table 3.3, Ti-felt/undoped Fe_2O_3 showed the lowest N_D (6.70×10^{19} cm^{-3}). The N_D of Ti-felt/Ti-Fe_2O_3

(air), at 5.69 × 10^{20} cm^{-3}, was much lower than that of Ti-felt/Ti-Fe_2O_3(two-step), at 8.58 × 10^{21} cm^{-3}.

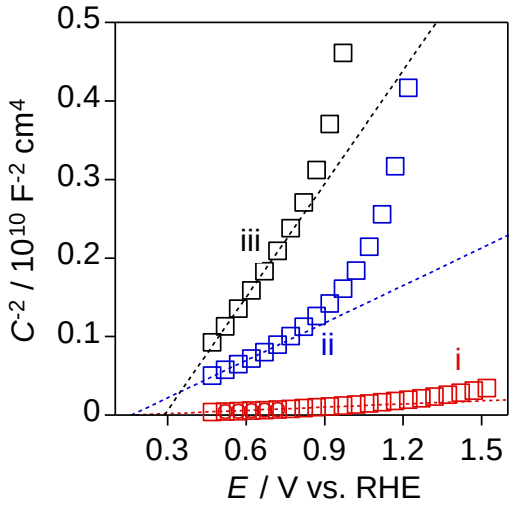

Figure 3.10: Mott–Schottky plots of (i) Ti-felt/Ti-Fe_2O_3, (ii) FTO/Ti-Fe_2O_3, and (iii) Ti-sheet/Ti-Fe_2O_3 in the dark condition.

This result indicates that Ti doping and the second-step Ar annealing contributed to an increase in the electron concentration of Fe_2O_3 on the Ti felt. Annealing in a non-oxidizing atmosphere produces electrons and oxygen vacancies, as explained by the Kröger–Vink notation as follows:

$$Fe_2O_3 \longrightarrow 2Fe_{Fe}^{\times} + 2e' + 2O_O^{\times} + V_O^{\bullet\bullet} + \frac{1}{2}O_2 \qquad (3.5)$$

where $O_O^{\times}$ and $V_O^{\bullet\bullet}$ represent the double positive charges of oxygen vacancies and lattice O^{2-}, respectively. Ti^{4+} ions act as electron donors for Fe_2O_3 as shown in Eq. 6.

$$2TiO_2 \xrightarrow{Fe_2O_3} 2Ti_{Fe}^{\bullet} + 2e' + 3O_O^{\times} + \frac{1}{2}O_2 \qquad (3.6)$$

where $Ti_{Fe}^{\bullet}$ is the Ti^{4+} species at the Fe^{3+} sites. Successful Ti^{4+} doping reduces the number of oxygen vacancies, which may act as recombination centers. The increase in the electron concentration from Ti^{4+} doping and the two-step annealing treatments is consistent with the improved electrical conductivity of n-type semiconductors.[26] Higher electrical conductivity

could provide the advantage of a longer electron diffusion length required for high PEC activity. The photocurrent responses for Ti-felt/undoped Fe_2O_3 (air) and Ti-felt/Ti-Fe_2O_3 (air) were 0.06 and 0.14 mA cm^{-2}, respectively, at 1.23 V vs. RHE, which were much less than that of Ti-felt/Ti-Fe_2O_3 (two-step) (Figures 3.11 B and C). Therefore, a higher electron concentration improves PEC properties.

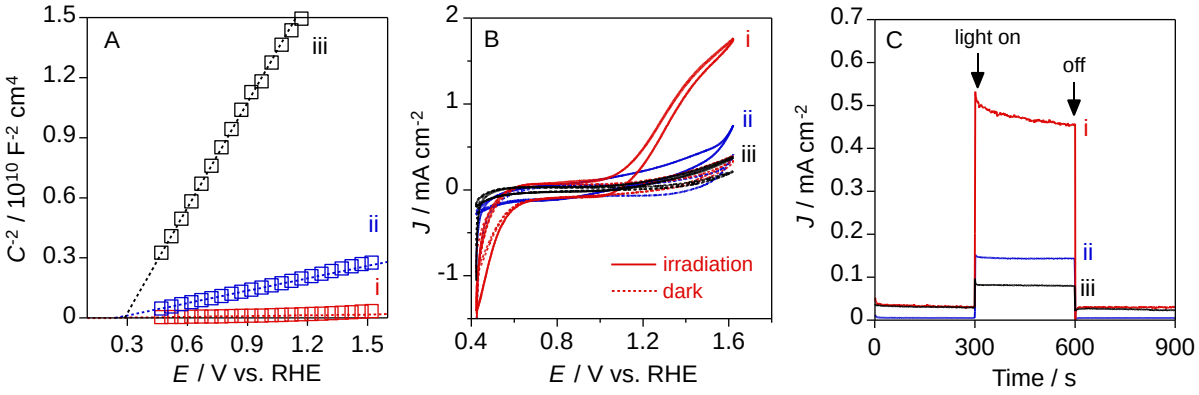

Figure 3.11: PEC properties of (i) Ti-felt/Ti-Fe_2O_3(two-step), (ii) Ti-felt/Ti-Fe_2O_3(air), and (iii) Ti-felt/non-doped Fe_2O_3(air) in 1 mol L^{-1} sodium hydroxide solution under one–sun irradiation (300–600 s, I_0 = 100 mW cm^{-2}); (A) Mott–Schottky plots in the dark condition. (B) Current–potential (V vs. RHE) curves at a sweep rate of 0.05 V s^{-1}. The dashed line indicates the current density in the dark. (C) Photocurrent response at 1.23 V vs. RHE under irradiation at 300–600 s.

3.3.5 Charge transfer behavior of Ti-Fe_2O_3 photoanodes

To analyze the charge transfer behavior of Fe_2O_3 prepared on Ti felt and FTO-coated glass conductive substrates, electrochemical impedance spectroscopy was conducted in PEC water oxidation at 1.23 V vs. RHE (Figure 3.12). The Nyquist plots for Ti-felt/Ti-Fe_2O_3 and FTO/Ti-Fe_2O_3 show that the semicircle diameter decreased when Ti-doped Fe_2O_3 was prepared on Ti

felt. To quantitatively analyze the charge-transfer resistance, the Nyquist plot was fitted to an equivalent circuit model to determine the parameters.

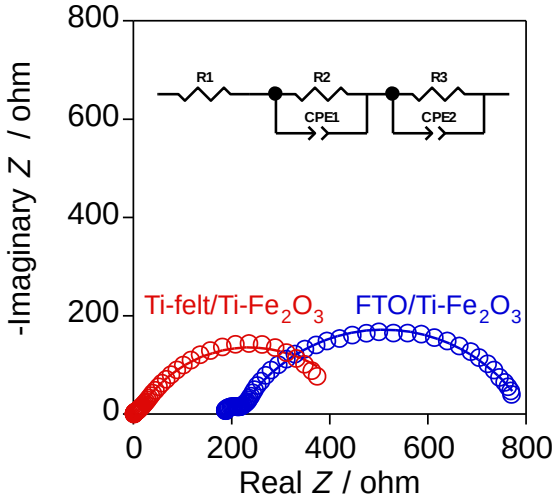

Figure 3.12: EIS spectra of Ti-felt/Ti-Fe_2O_3 and FTO/Ti-Fe_2O_3 at 1.23 V vs. RHE under one-sun irradiation (I_0 = 100 mW cm^{-2}). The inset graph is the equivalent circuit model used to obtain the Nyquist plot for both samples.

The fitting results for the impedance spectra of Ti felt/Ti-Fe $_2O_3$ and FTO/Ti-Fe_2O_3 are shown in Figure 3.13. *CPE* and R_1 represent the constant phase elements due to heterogeneity in the system and the resistance due to the electrolyte and conductive substrate, respectively. R_2 and R_3 represent the resistances of interfacial charge transfer. R_3 indicates the distortion of the semicircle. The estimated values of R_1 for Ti-felt/Ti-Fe_2O_3 and FTO/Ti-Fe_2O_3 were 1.22 Ω and 184 Ω, respectively. These differences are due to the different sheet resistance of the conductive substrates. The R_2 value for Ti-felt/Ti-Fe_2O_3 (458 Ω) was smaller than that of FTO/Ti-Fe_2O_3 (589 Ω). The lower charge transfer resistance at the semiconductor–electrolyte interface suggests better electron transport in both the bulk and at the interface of the photoanode. The semicircle for the less PEC-active FTO/Ti-Fe_2O_3 was large with significant distortions in the Nyquist plot.[28]

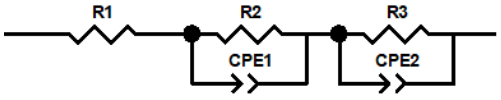

A

Element	Freedom	Value	Error	Error %
R1	Free(+)	1.223	0.035033	2.8645
R2	Free(+)	457.7	22.505	4.917
CPE1-T	Free(+)	0.0010534	5.7799E-05	5.4869
CPE1-P	Free(+)	0.67992	0.016463	2.4213
R3	Free(+)	7.269	1.0252	14.104
CPE2-T	Free(+)	8.8888E-05	3.1197E-05	35.097
CPE2-P	Free(+)	0.88545	0.041244	4.658

Chi-Squared:	0.011817
Weighted Sum of Squares:	0.57108

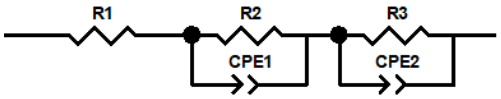

B

Element	Freedom	Value	Error	Error %
R1	Free(+)	183.6	0.81412	0.44342
R2	Free(+)	588.7	3.129	0.53151
CPE1-T	Free(+)	0.00023416	3.2453E-06	1.3859
CPE1-P	Free(+)	0.67162	0.0037962	0.56523
R3	Free(+)	31.4	1.3538	4.3115
CPE2-T	Free(+)	4.0199E-06	1.4036E-06	34.916
CPE2-P	Free(+)	0.8277	0.035164	4.2484

Chi-Squared:	0.00046673
Weighted Sum of Squares:	0.0062538

Figure 3.13: The equivalent circuit model for the Nyquist plot. The fitting parameters for the plots of (A) Ti-felt/Ti-Fe_2O_3, and (B) FTO/Ti-Fe_2O_3.

3.3.6 Effect of incident light intensity

Figure 3.14A shows the effect of light intensities (1.5 to 41 mW cm^{-2}) on the PEC efficiency of Ti-felt/Ti-Fe_2O_3 and FTO/Ti-Fe_2O_3. The samples were initially incubated in the dark for 60 s, followed by UV irradiation for 120 s. J_{photo} was linearly enhanced as a consequence of the increased incident light intensity. As previously concluded, the photocurrent response of Ti-felt/Ti-Fe_2O_3 was higher than that of FTO/Ti-Fe_2O_3.

Figure 3.14B shows the relationship between J_{photo} and light intensity. The transient photocurrent was evaluated by observing different values of the initial and steady-state photocurrents. A notable change in the initial and steady-state J_{photo} values was observed with the increase in the incident light intensity. For both samples, J_{photo} was stable at low intensities. However, a significant gap between the initial and steady-state photocurrents was observed when the incident light intensity was higher than 20 mW cm^{-2}. This behavior suggests that a large number of photogenerated charge carriers lead to a high rate of recombination at high light intensities.[4]

The relationship between IPCE and light intensity is shown in Figure 3.14C. No significant change in the IPCE of Ti-felt/Ti-Fe_2O_3 occurred over the entire range of incident light intensities. This result indicates that the IPCE of Fe_2O_3 prepared on 3D-conductive substrates was constant even when the light intensity was low. In contrast, the IPCE values of FTO/Ti-Fe_2O_3 were small in the light intensity range of 1.5–5.0 mW cm^{-2}. It then reached a steady-state IPCE in the light intensity range of 9.0–41 mW cm^{-2}. The lower activity of FTO/Ti-Fe_2O_3 at low light intensities can be attributed to insufficient light absorption due to the lower loading of Fe_2O_3 on the 2D-structured conductive substrates.

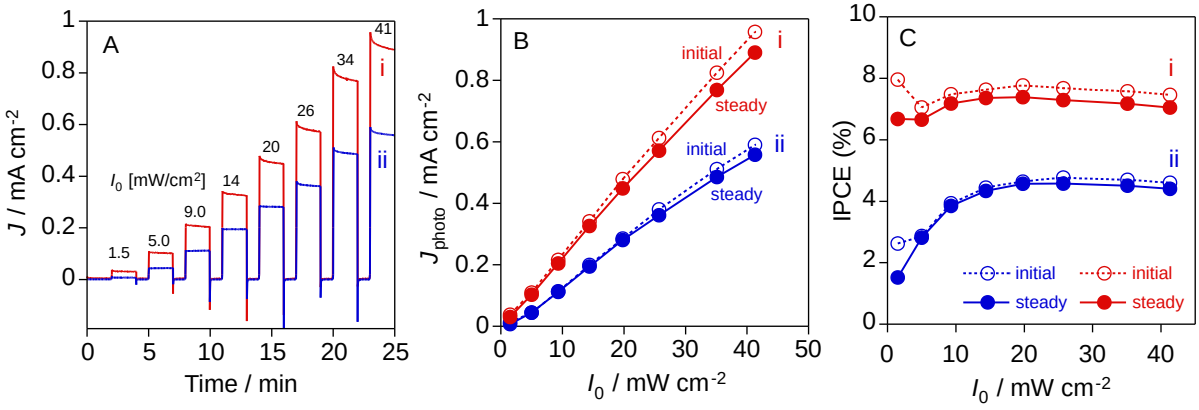

Figure 3.14: Effect of incident light intensities (I_0) on the PEC properties of (i) Ti-felt/Ti-Fe_2O_3 and (ii) FTO/Ti-Fe_2O_3 in a 1 mol L^{-1} NaOH solution at 1.23 V vs. RHE under 385-nm light irradiation; (A) current–time curve in an I_0 range of 1.5–41 mW cm^{-2}; (B) initial photocurrent

(dashed lines) and steady-state photocurrent (straight lines) densities; (C) IPCE at the initial (dashed lines) and steady states (straight lines).

3.3.7 Effect of similar Fe_2O_3 thickness on 2D- and 3D-conductive substrates

Ti-doped Fe_2O_3 films with similar thicknesses were fabricated on Ti sheets and felt substrates. The Fe_2O_3 denoted as Ti-sheet/Ti-Fe_2O_3(Hyd2) was synthesized on the Ti sheet using the same method with a shorter hydrothermal reaction time (2 h) to reduce the thickness of Fe_2O_3 (Figure 3.15). As a result, the loading amount on the Ti sheet (12 cm^2) decreased to 2.50 mg, which is approximately half that of Ti-sheet/Ti-Fe_2O_3 prepared by a hydrothermal reaction for 10 h, as shown in Table 1. The thickness of the Fe_2O_3 layer on the Ti sheet was similar to that on the Ti felt (0.5 to 1 μm). In contrast, the J_{photo} and N_D of Ti-sheet/Ti-Fe_2O_3(Hyd2) decreased to 0.09 mA cm^{-2} and 1.07×10^{20} cm^{-3}, respectively (Figure 3.16). The decrease in J_{photo} by approximately one-third was partly attributed to the diminishing Fe_2O_3 loading on the substrates, which led to reduced N_D and light absorption.

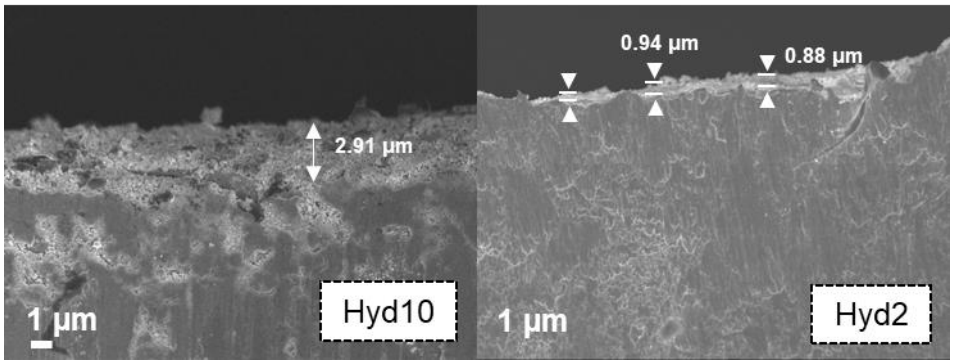

Figure 3.15: Cross-sectional side view SEM images of Ti-sheet/Ti-Fe_2O_3(Hyd10) and Ti-sheet/Ti-Fe_2O_3(Hyd2).

Preparation of photoelectrodes on 2D substrates requires thick layers for effective photoabsorption.[5] However, it increases charge recombination because of its short carrier

diffusion length. Importantly, the PEC activity of Fe_2O_3 on 3D-porous substrates was higher than that on conventional 2D substrates, even with similar thicknesses. Table 3.4 summarizes the reported PEC properties of several photoelectrodes prepared on 2D and 3D substrates. The photoelectrodes on the 3D substrates showed a similar trend, which was a higher J_{photo} than that on the 2D substrates.

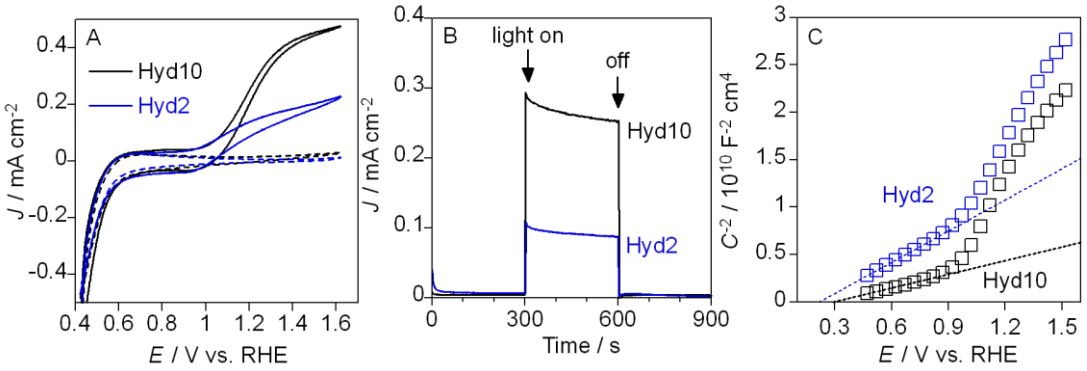

Figure 3.16: PEC properties in a 1 mol L^{-1} NaOH solution of Ti-sheet/Ti-Fe_2O_3 under one-sun irradiation (I_0 = 100 mW cm^{-2}); (A) Current–potential curve. The dashed line indicates the current density in the dark. (B) Photocurrent response at 1.23 V vs. RHE under irradiation for 300–600 s. (C) Mott–Schottky plots in the dark condition.

Table 3.4. The comparison of photocurrent density (J_{photo}) for several photoelectrodes prepared on the 2D and 3D conductive substrates in the PEC application

No	Photoelectrode	J_{photo} / mA cm^{-2} (2D substrate)	J_{photo} / mA cm^{-2} (3D substrate)	Applied potential	Irradiation	Ref.
1	Cu_2O	2.5	5.7	−0.4 V vs Ag/AgCl	385 nm (40 mW cm^{-2})	4
2	WO_3	~1	~6	1.0 V vs Ag/AgCl	385 nm (40 mW cm^{-2})	22
3	Fe_2O_3	0.6	1.5	1.6 V vs RHE	1 sun (100 mW cm^{-2})	25
4	Fe_2O_3	0.31	0.43	1.23 V vs RHE	1 sun (100 mW cm^{-2})	This work

3.3.8 Photoelectrochemical stability and oxygen evolution reaction

The photocurrent stability was evaluated at 1.23 V vs. RHE for 3 h under one-sun irradiation (Figure 3.17). No change was observed in the J_{photo} of Ti-felt/Ti-Fe_2O_3 from an initial value of 0.43 mA cm^{-2}. FTO/Ti-Fe_2O_3 also exhibited a stable J_{photo} of 0.32 mA cm^{-2}.

Figure 3.18 shows the PEC-OER tested at 1.50 V vs. RHE under 385-nm light irradiation. UV irradiation was performed for 30–60 min. The photoanode and cathode compartments were separated using an alkaline anion-exchange membrane (Figure 3.19). The evolution rates of O_2 for Ti-felt/Ti-Fe_2O_3 and FTO/Ti-Fe_2O_3 were ~0.23 µmol min^{-1} and ~0.09 µmol min^{-1}, respectively.

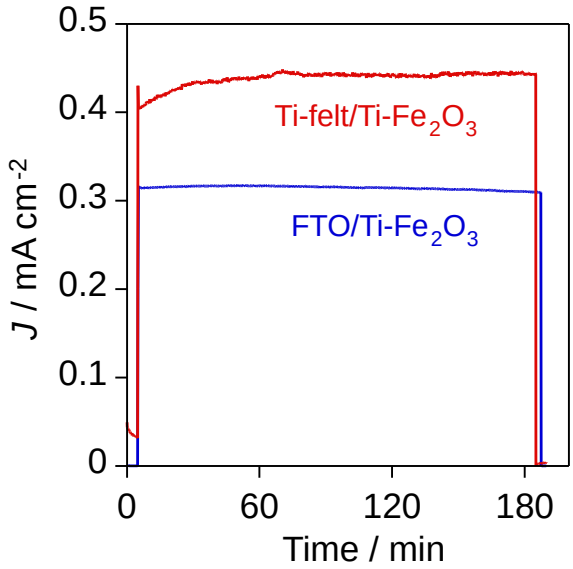

Figure 3.17: Photocurrent stability of Ti-felt/Ti-Fe_2O_3 and FTO/Ti-Fe_2O_3 at 1.23 V vs. RHE for 3 h under one–sun irradiation (I_0 = 100 mW cm^{-2}).

The IPCE value of Ti-felt/Ti-Fe_2O_3 was observed to be 13.7% during initial light irradiation and decreased to 12.4% after 30 min of irradiation. In the case of FTO/Ti-Fe_2O_3, the IPCE value diminished from 6.29% to 5.44%. The Faraday efficiency (FE), which is the ratio of electric current to total electric current, was calculated using Eq. 7.

$$FE = (n\ F\ r) / J_{photo} \tag{3.7}$$

where n is the number of O_2 electrons (4), F is the Faraday constant, and r is the rate of O_2 formation.[29] The values of FE for O_2 evolution in the photoanode compartment were estimated to be approximately 96.7% and 94.8% for Ti-felt/Ti-Fe_2O_3 and FTO/Ti-Fe_2O_3, respectively. Considering the IPCE value and Faradaic efficiency, Ti-felt/Ti-Fe_2O_3 showed higher PEC-OER activity than FTO/Ti-Fe_2O_3. Fe_2O_3 photoanodes on a 3D-conductive substrate are promising materials for applications in membrane electrode assembly systems in the future.

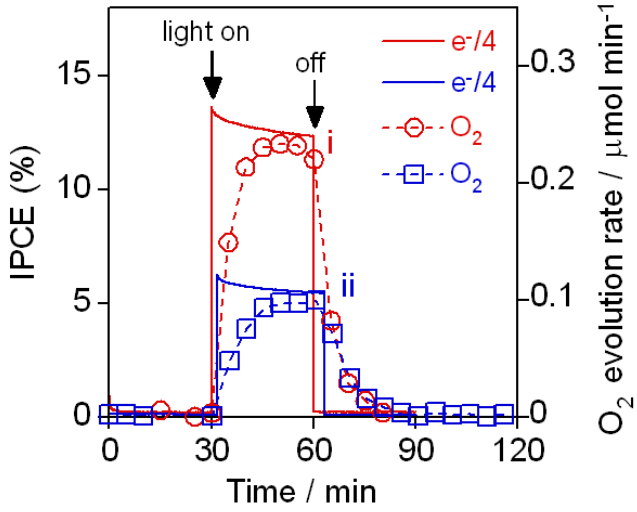

Figure 3.18: PEC-OER of (i) Ti-felt/Ti-Fe_2O_3 and (ii) FTO/Ti-Fe_2O_3 at 1.50 V vs. RHE under 385-nm light irradiation (30–60 min, I_0 = 40 mW cm^{-2}).

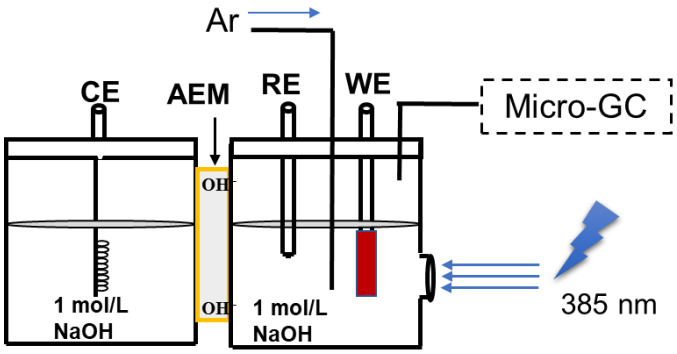

Figure 3.19: Schematic illustration for PEC oxygen evolution reaction in a 1 mol/L NaOH solution (pH= ~13.6). Counter and reference electrodes were Pt and Hg/HgO (E_0 = 118 mV vs. RHE), respectively. The light irradiation was sourced from a light-emitting diode (peak

wavelength 385 nm, I_0 = 40 mW cm^{-2}). The reaction was performed under an Ar stream at a flow rate of ~20 mL/min and a temperature range of 25–27 °C. An anion exchange membrane (AEM) was used to separate the anode and cathode compartments.

3.4 Conclusions

Ti-doped Fe_2O_3 films were prepared on three-dimensional and conventional two-dimensional substrates using a hydrothermal method followed by a two-step annealing treatment. The larger specific surface area of the 3D macroporous Ti felt produced the highest loading amount and a thinner Ti-doped Fe_2O_3 layer. Ti-doped Fe_2O_3 on Ti felt (Ti-felt/Ti-Fe_2O_3) exhibited an improved photocurrent response. The donor density was increased by Ti^{4+} doping, and two-step annealing improved the electrical conductivity, resulting in a larger charge-diffusion length than the thickness of the semiconductor layer, which provided less recombination. A higher loading of Fe_2O_3 on Ti felt contributed to an increase in photoabsorption, which enhanced the PEC properties of Fe_2O_3. Additionally, the IPCE of Ti-felt/Ti-Fe_2O_3 was not dependent on irradiance owing to sufficient light absorption, even at low light intensity. The Fe_2O_3 photoanodes on Ti felt also showed good photocurrent stability for O_2 evolution. The use of a 3D-conductive substrate is promising for the preparation of Fe_2O_3 photoanodes with improved PEC activity for solar-to-chemical conversion. It is believed that the macroporous photoanodes can be applied to the membrane electrode assembly systems for gas-fed reactions and mass-transport-limited reactions.

References

1. Tahir, A. A., Upul Wijayantha, K. G., Saremi-Yarahmadi, S., Maznar, M. & McKee, V. Nanostructured α-Fe_2O_3 Thin Films for Photoelectrochemical Hydrogen Generation. *Chem. Mater.* **21**, 3763–3772 (2009).
2. Kay, A., Cesar, I. & Grätzel, M. New Benchmark for Water Photooxidation by Nanostructured α-Fe_2O_3 Films. *J. Am. Chem. Soc.* **128**, 15714–15721 (2006).
3. Rahman, G. & Joo, O. S. Facile Preparation of Nanostructured α-Fe_2O_3 Thin Films with Enhanced Photoelectrochemical Water Splitting Activity. *J. Mater. Chem. A* **1**, 5554–5561 (2013).
4. Amano, F., Uchiyama, A., Furusho, Y. & Shintani, A. Effect of Conductive Substrate on The Photoelectrochemical Properties of Cu_2O Film Electrodes for Methyl Viologen Reduction. *J. Photochem. Photobiol. A Chem.* **389**, 1–8 (2020).
5. Homura, H., Tomita, O., Higashi, M. & Abe, R. Fabrication of $CuInS_2$ Photocathodes on Carbon Microfiber Felt by Arc Plasma Deposition for Efficient Water Splitting Under Visible Light. *Sustain. Energy Fuels* **1**, 699–709 (2017).
6. Brillet, J., Gra, M., Sivula, K. & Fe, P. Decoupling Feature Size and Functionality in Electrodes for Solar Water Splitting. *Nano Lett.* **10**, 4155–4160 (2010).
7. Kim, J. Y. *et al.* Single-Crystalline, Wormlike Hematite Photoanodes for Efficient Solar Water Splitting. *Sci. Rep.* **3**, 1–8 (2013).
8. Amano, F., Mukohara, H. & Shintani, A. Rutile Titania Particulate Photoelectrodes Fabricated by Two-Step Annealing of Titania Nanotube Arrays. *J. Electrochem. Soc.* **165**, H3164–H3169 (2018).
9. Cesar, I., Sivula, K., Kay, A., Zboril, R. & Grätzel, M. Influence of Feature Size, Film Thickness, and Silicon Doping on The Performance of Nanostructured Hematite Photoanodes for Solar Water Splitting. *J. Phys. Chem. C* **113**, 772–782 (2009).

10. Ling, Y., Wang, G., Wheeler, D. A., Zhang, J. Z. & Li, Y. Sn-Doped Hematite Nanostructures for Photoelectrochemical Water Splitting. *Nano Lett.* **11**, 2119–2125 (2011).

11. Ahmed, M. G. *et al.* A Facile Surface Passivation of Hematite Photoanodes with TiO_2 Overlayers for Efficient Solar Water Splitting. *ACS Appl. Mater. Interfaces* **7**, 24053–24062 (2015).

12. Klahr, B., Gimenez, S., Fabregat-Santiago, F., Hamann, T. & Bisquert, J. Water Oxidation at Hematite Photoelectrodes: The Role of Surface States. *J. Am. Chem. Soc.* **134**, 4294–4302 (2012).

13. Kraushofer, F. *et al.* Atomic-Scale Structure of The Hematite α-Fe_2O_3(11-02) 'r-Cut' Surface. *J. Phys. Chem. C* **122**, 1657–1669 (2018).

14. Phuan, Y. W., Ong, W. J., Chong, M. N. & Ocon, J. D. Prospects of Electrochemically Synthesized Hematite Photoanodes for Photoelectrochemical Water Splitting: A Review. *J. Photochem. Photobiol. C Photochem. Rev.* **33**, 54–82 (2017).

15. Chae, S. Y., Rahman, G. & Joo, O. shim. Elucidation of The Structural and Charge Separation Properties of Titanium-Doped Hematite Films Deposited by Electrospray Method for Photoelectrochemical Water Oxidation. *Electrochim. Acta* **297**, 784–793 (2019).

16. Liu, Y., Yu, Y. X. & Zhang, W. De. Photoelectrochemical Properties of Ni-Doped Fe_2O_3 Thin Films Prepared by Electrodeposition. *Electrochim. Acta* **59**, 121–127 (2012).

17. Huang, J., Hu, G., Ding, Y., Pang, M. & Ma, B. Mn-Doping and NiFe Layered Double Hydroxide Coating: Effective Approaches to Enhancing The Performance of α-Fe_2O_3 in Photoelectrochemical Water Oxidation. *J. Catal.* **340**, 261–269 (2016).

18. Duret, A. & Grätzel, M. Visible Light-Induced Water Oxidation on Mesoscopic α-Fe_2O_3 Films Made by Ultrasonic Spray Pyrolysis. *J. Phys. Chem. B* **109**, 17184–17191 (2005).

19. Ahn, H. J., Kwak, M. J., Lee, J. S., Yoon, K. Y. & Jang, J. H. Nanoporous Hematite Structures to Overcome Short Diffusion Lengths in Water Splitting. *J. Mater. Chem. A* **2**, 19999–20003 (2014).

20. Amano, F. *et al.* Vapor-Fed Photoelectrolysis of Water at 0.3 V using Gas-Diffusion Photoanodes of $SrTiO_3$ Layers. *Sustain. Energy Fuels* **4**, 1443–1453 (2020).

21. Wang, Y. *et al.* A 3D Nanoporous Ni-Mo Electrocatalyst with Negligible Overpotential for Alkaline Hydrogen Evolution. *ChemElectroChem* **1**, 1138–1144 (2014).

22. Amano, F., Shintani, A., Tsurui, K. & Hwang, Y. M. Fabrication of Tungsten Trioxide Photoanode with Titanium Microfibers as A Three Dimensional Conductive Back Contact. *Mater. Lett.* **199**, 68–71 (2017).

23. Stoll, T. *et al.* Visible-Light-Promoted Gas-Phase Water Splitting using Porous $WO_3/BiVO_4$ Photoanodes. *Electrochem. commun.* **82**, 47–51 (2017).

24. Zafeiropoulos, G. *et al.* Porous Titania Photoelectrodes Built on A Ti-Web of Microfibers for Polymeric Electrolyte Membrane Photoelectrochemical (PEM-PEC) Cell Applications. *Sol. Energy Mater. Sol. Cells* **180**, 184–195 (2018).

25. Caretti, M. *et al.* Transparent Porous Conductive Substrates for Gas-Phase Photoelectrochemical Hydrogen Production. *Adv. Mater.* **35**, (2023).

26. Apriandanu, D. O. B., Nomura, S., Nakayama, S., Tateishi, C. & Amano, F. Effect of Two-Step Annealing on Photoelectrochemical Properties of Hydrothermally Prepared Ti-Doped Fe_2O_3 Films. *Catal. Today* (2022) doi:10.1016/j.cattod.2022.06.041.

27. Amano, F., Nakata, M., Yamamoto, A. & Tanaka, T. Effect of Ti^{3+} Ions and Conduction Band Electrons on Photocatalytic and Photoelectrochemical Activity of Rutile Titania for Water Oxidation. *J. Phys. Chem. C* **120**, 6467–6474 (2016).

28. Amano, F., Ohtani, B. & Yoshida, H. Role of Doped Titanium Species in The Enhanced Photoelectrochemical Properties of Iron Oxide Films: Comparison between water

oxidation and iodide ion oxidation. *J. Electroanal. Chem.* **766**, 100–106 (2016).

29. Ta, C. X. M., Akamoto, C., Furusho, Y. & Amano, F. A Macroporous-Structured WO_3/Mo-Doped $BiVO_4$ Photoanode for Vapor-Fed Water Splitting under Visible Light Irradiation. *ACS Sustain. Chem. Eng.* **8**, 9456–9463 (2020).

Chapter 4. Anion exchange membrane water splitting using porous Fe_2O_3 photoanodes

4.1 Introduction

The advancement of sustainable water-splitting technologies holds immense significance in the quest for renewable energy sources. Photoelectrochemical (PEC) water splitting emerged as a promising approach for driving oxygen evolution reactions (OER) and hydrogen evolution reactions (HER) by utilizing light energy.[1,2] However, conventional PEC systems necessitate the presence of a supporting electrolyte to increase the conductivity of the aqueous solution in the water-splitting reaction. This reliance on liquid electrolytes, such as H_2SO_4 and NaOH, can impede the development of a more practical and efficient PEC water-splitting system due to their persistent detrimental impact on the environment and financial resources.

Recently, there has been a growing interest in exploring porous-based photoelectrodes for PEC devices incorporating a solid electrolyte membrane. In the PEC hydrogen production over TiO_2-based membrane electrode assembly (MEA), H^+ is transported from the anode to the cathode through the proton exchange membrane (PEM), where they undergo reduction to generate hydrogen molecules.[3] The PEM-PEC cells have been successfully investigated for vapor-fed photoelectrolysis in the absence of liquid electrolytes.[4–10] The role of the membrane as a solid electrolyte is to facilitate proton transfer, while effectively separating the anode and cathode compartments in the PEC water splitting cell. To enable ion transport and drive the water oxidation reaction, the membrane requires a photoanode with a porous structure. Numerous studies have employed the use of macroporous three-dimensional conductive substrate to prepare the porous photoanodes for the PEM-PEC system.[4–6,8–10]

Chapter 4

Hematite photoanode is a favorable candidate for PEC water splitting due to its abundance and suitable bandgap to visible light irradiation.[11–13] However, hematite exhibits stability solely in alkaline environments, as indicated by the Pourbaix diagram.[14] Therefore, coupling the hematite photoanode with PEM, which is only compatible with acidic-tolerance photoelectrodes, is not feasible.[15] On the other hand, an anion exchange membrane (AEM) is a solid polymer electrolyte that facilitates the transport of anions, especially OH^- ions, often employing quaternary ammonium-type positively charged ions (Figure 4.1),[16] is commonly employed in highly alkaline conditions (pH >10).[17,18] This property is advantageous for the hematite photoanode for the developed PEC system using a solid electrolyte membrane, particularly considering its instability under acidic conditions.

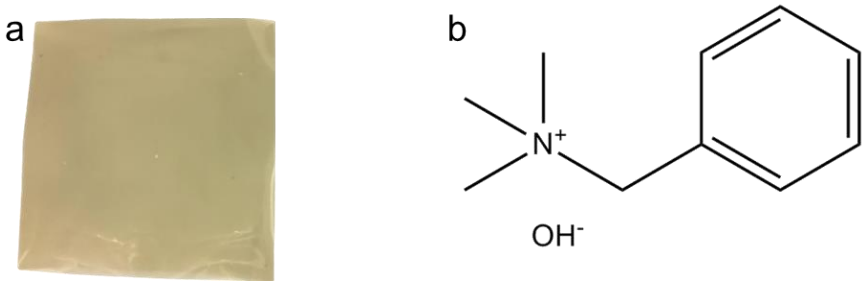

Figure 4.1: (a) Photograph of AEM and (b) chemical structure of quaternary ammonium type, $-NR_3^+$ in AEM.

Sivula and coworkers demonstrated the fabrication of porous hematite photoanode on transparent porous conductive substrates.[19] However, their study did not observe the PEC properties of the hematite photoanode in the presence of a solid electrolyte membrane. The combination of porous photoelectrodes with AEM has not been reported in the literature thus far. In this study, the PEC water-splitting using porous hematite-based photoanode in two-compartment cells was demonstrated, which are in the photoanode, and cathode parts separated by AEM. The AEM-PEC water splitting was conducted in pure water without supporting electrolytes, utilizing visible light irradiation.

Chapter 4

4.2 Experimental section

4.2.1 Fabrication of Ti/Ti-Fe_2O_3 photoanodes

Ti/Ti-Fe_2O_3 was fabricated on macroporous 3D titanium felt substrates (0.1 mm thickness; 67% porosity; Nikko Techno, Japan) using a hydrothermal method with Ti doping and two-step annealing treatments.[11,20] The Ti felt substrate was vertically positioned in a stainless-steel Teflon-lined autoclave containing a solution composed of ferric nitrate ($Fe(NO_3)_3$ $9H_2O$, 99.9%, Wako Pure Chemical, Japan), sodium nitrate ($NaNO_3$, 99.9%, Wako Pure Chemical, Japan), and titanium (IV) chloride ($TiCl_4$, 16–17% Ti, Wako Pure Chemical, Japan). The hydrothermal reaction was treated at 120 °C for 10 h. Subsequently, the substrate was rinsed successively with ethanol and ultrapure water, followed by drying at 100 °C for 10 min. The two-step annealing of the sample was sequentially carried out; first, at 550°C for 2 h in air, and then at 300°C for 2 h under an argon atmosphere. The resulting photoanode was designated as Ti/Ti-Fe_2O_3.

4.2.2 Deposition of Al_2O_3 on Ti/Ti-Fe_2O_3 photoanodes

Al_2O_3 passivation layer was deposited on Ti/Ti-Fe_2O_3 by the atomic layer deposition (ALD) method. The condition was slightly modified from the previous report.[13,21] The photoanodes were placed in a vacuum chamber of the ALD system (Anric Technologies, AT-410). The Al_2O_3 layer was loaded at 200°C using trimethylaluminum as the precursor, water as the oxidant, and nitrogen as the carrier gas. The deposition process consisted of eight cycles. The resulting photoanode was designated as Ti/Ti-Fe_2O_3-Al_2O_3.

4.2.3 Loading of CoPi on Ti/Ti-Fe_2O_3-Al_2O_3 photoanodes

CoPi as a co-catalyst was deposited on Ti/Ti-Fe_2O_3-Al_2O_3 using the photoelectrodeposition method under 1-sun irradiation.[12,22] CoPi solution (pH=~8) comprised 0.5 mM of cobalt (II) nitrate ($Co(NO_3)_2.6H_2O$, 99.9%, Wako Pure Chemical, Japan) and 0.1 M of Disodium hydrogenphosphate (Na_2HPO_4, 99.0%, Wako Pure Chemical, Japan) The deposition was performed at an applied potential of 1.77 V versus reversible hydrogen electrode (RHE) within 60 s recorded by chronoamperometry measurement. The resulting photoanode was designated as Ti/Ti-Fe_2O_3-Al_2O_3-CoPi.

4.2.4 Characterizations of photoanodes

The features of macroporous 3D Ti felt substrates and porous hematite-based photoanodes were confirmed by Field-emission scanning electron microscopy (FE-SEM, JSM–7500 F microscope, JEOL, Japan) at an acceleration voltage of 5.0 kV. The elemental mapping images were analyzed by scanning electron microscopy with energy–dispersive X-ray spectroscopy (Desktops SEM-EDX, Phenom ProX, Thermo Fisher Scientific, Japan). UV–Vis diffuse reflectance spectrophotometer (UV–2600, Shimadzu, Japan) was used to estimate the bandgap energy. X-ray diffraction (XRD, SmartLab, Rigaku, Japan) with Cu Kα radiation at 40 kV and 30 mA was utilized to analyze the crystal structure. Raman spectra were acquired using a confocal Raman microscope (XploRA PLUS, Horiba, Japan) with a laser excitation wavelength of 532 nm. X-ray photoelectron spectroscopy (XPS, JPS-9010 MX, JEOL, Japan) with irradiation of Mg Kα was employed to validate the oxidation state of the element present on the photoanode surface. X-ray absorption fine edge structure (XAFS) spectra at Ti K-edges were recorded at the BL11S2 beamline of the Aichi Synchrotron Radiation Center. The spectra were recorded in a fluorescence mode for FTO/Ti-Fe_2O_3 and a transmission mode for reference samples at room temperature using Si (111) double-crystal monochromator. The valence band

maximum (VBM) of the photoanodes was measured by photoelectron yield spectroscopy (PYS, Bunkoukeiki BIP-KV201) at the wavelength of 130–310 nm (4.00–9.54 eV) in a vacuum. The monochromator (slit 1.0 mm) was purged by N_2 gas with a flow rate of 2 L/min. Photomultiplier Tube (PMT) was used as an irradiation intensity detector. Au foil was used as a reference for energy calibration with an ionization energy of about 4.70 eV.

4.2.5 Photoelectrochemical (PEC) measurements

4.2.5.1 PEC measurements in a conventional system

A three-electrode system was configured in a one-compartment glass cell using porous hematite-based photoanodes as the working electrodes, Hg/HgO reference electrode (RE), and platinum wire counter electrode (CE). All the PEC measurements were performed by using a potentiostat (VersaSTAT 3, Princeton Applied Research) at 25°C. The aqueous electrolyte solutions used were NaOH at concentrations of 1, 0.1, and 0.01 M. In addition, 1 M sodium sulfate ($NaSO_4$, 99.9%, Wako Pure Chemical, Japan) was also used after adjusting pH to ~9 and ~10.5 by using NaOH solution. The photoanode with an area of 1 cm^2 was irradiated by simulated sunlight (AM 1.5G, I_0=100 mW cm^{-2}) from a solar simulator (XES-40S1, SAN-EI Electric, Japan). Linear scan voltammogram (current–potential curve) was recorded at a scan rate of 50 mV s^{-1} in the applied potential range from −0.5 to +0.7 V vs. Hg/HgO. All the potentials were converted to the RHE scale using the Nernst equation.

$$E \text{ (versus RHE)} = E \text{ (versus Hg/HgO)} + 0.059 \text{ pH} + E^{\circ}_{\text{Hg/HgO}} \quad (4.1)$$

Here, $E^{\circ}_{\text{Hg/HgO}}$ corresponds to the standard electrode potential of Hg/HgO (+0.118 V versus standard hydrogen electrode). The current–time curve was obtained through chronoamperometry (CA) measurement at 1.23 V versus RHE with irradiation performed from 300 to 600 s.

The values of incident photon-to-current conversion efficiency (IPCE) were evaluated at 1.23 V vs. RHE using a 300-W xenon lamp (MAX-303, Asahi Spectra, Japan). The various wavelengths from 310 to 710 nm were applied, and the light intensity was measured using an optical power meter (3664, Hioki, Japan). The IPCE value at a specific wavelength was calculated using the following equation:

$$\mathrm{IPCE} = \frac{J_{\mathrm{photo}}}{I_0} \times \frac{1240}{\lambda} \tag{4.2}$$

where J_{photo} is the photocurrent density (mA cm^{-2}), I_0 is the incident light intensity (mW cm^{-2}), and λ is the wavelength (nm).

Mott–Schottky analysis was performed to estimate the donor density (N_D) under dark conditions. The measurement was performed at 1000 Hz with an applied sinusoidal amplitude of 10 mV. The capacitance (C) of the space charge layer was analyzed based on the imaginary component of the electrochemical impedance, considering a model comprising a series combination of a capacitor and a resistor. N_{D} and the flat-band potential (E_{fb}) were estimated by applying the Mott-Schottky formula to the plot of C^{-2} versus the applied potential (E), assuming a flat semiconductor model.

$$\frac{1}{C^2} = \frac{2}{q\varepsilon\varepsilon_0 N_{\mathrm{D}}}\left(E - E_{\mathrm{fb}} - \frac{kT}{q}\right) \tag{4.3}$$

where, q is the elementary electric charge, ε is the dielectric constant (12 for Fe_2O_3), ε_0 is the vacuum permittivity, k is Boltzmann's constant, and T is temperature. Electrochemical impedance spectroscopy (EIS) spectra at 1.23 V vs. RHE under 1-sun irradiation were measured at a frequency from 100 kHz to 0.1 Hz with a sinusoidal amplitude of 10 mV.

4.2.5.2 AEM-PEC measurements in two-compartment cells

Figure 4.2 illustrates the design of the AEM-PEC device in two-compartment cells. The porous hematite-based photoanode was manually attached to an AEM by sandwiching it between two gold plated-plates. AEM (Fumapem FAA-3-50, thickness 45-55 µm, Fumatech, Germany) was initially pretreated by immersing into NaCl 0.5 M for 24 h. The AEM and photoanode were further layered with a gasket to seal the solution side, and the membrane electrode assembly (MEA) was inserted between two gold-plated plates with an opening irradiation area of 1 cm^{-2}. In the photoanode part, the working electrode was immersed in ultra-pure water (conductivity < 0.1 mS/m, pH ~7) without liquid electrolyte. NaOH with various concentrations of 1, 0.2, and 0.1 M were used as the electrolyte solutions in the cathode part consisting of a platinum wire CE and Hg/HgO RE. The two-compartment glass cells were strongly pressed against the MEA to minimize the solution leakage from both compartments. The MEA faced the irradiation source of 1 simulated sun (AM 1.5G). The PEC properties were measured with LSV and CA under light irradiation with a similar procedure as described previously.

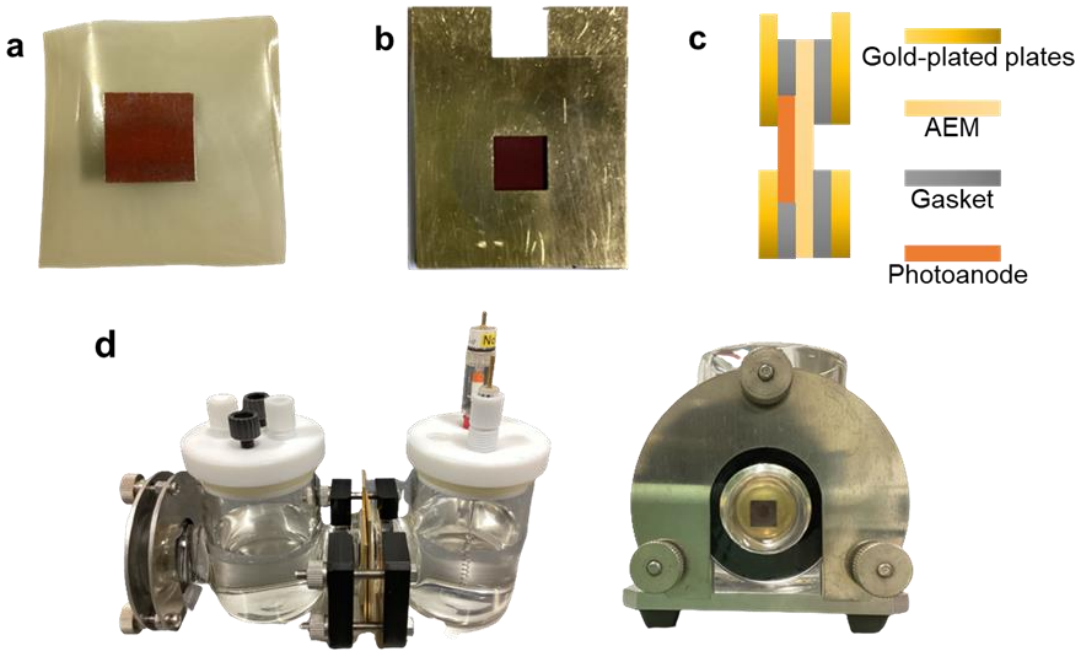

Figure 4.2: Photographs of (a) MEA comprising the hematite photoanode attached to an AEM and (b) the MEA sandwiched by two gold-plated plates. (c) Cross-sectional schematic diagram of the MEA. (d) Photograph of AEM-PEC system with a two-compartment cell configuration

4.3 Results and discussion

4.3.1 Characterizations of photoanodes

A porous hematite photoanode was fabricated on a Ti felt (Figure 4.3a), which was selected as a conductive substrate based on its high porosity. The hematite photoanode was prepared using Ti doping and two-step annealing process to improve its donor density, thus the electrical conductivity increases.[11] The surface of the Ti-doped hematite (Ti/Ti-Fe2O3) was modified by applying an Al2O3 passivation layer, which reduces surface recombination and shifts more negative onset potential,[23] utilizing the atomic layer deposition method. Furthermore, the Ti/Ti-Fe2O3-Al2O3 was loaded with a CoPi co-catalyst for oxygen evolution reaction through a photoelectrodeposition method.[22]

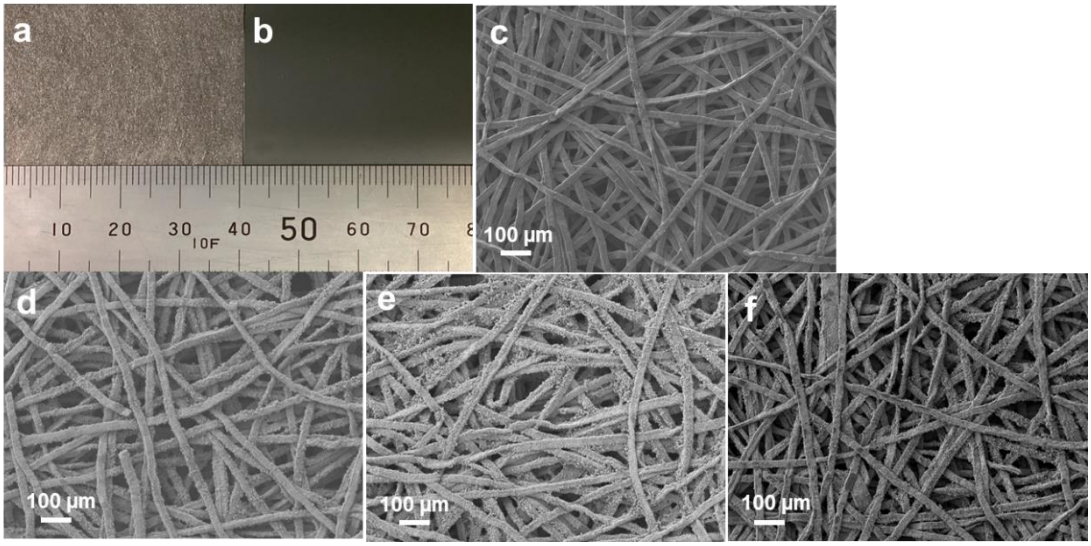

Figure 4.3: Photograph of (a) Ti-felt and (b) Ti-sheet substrates. Top-view SEM images of the samples: (c) Ti felt substrate, (d) Ti/Ti-Fe_2O_3, (e) Ti/Ti-Fe_2O_3-Al_2O_3 , and (f) Ti/Ti-Fe_2O_3-Al_2O_3-CoPi.

Table 4.1. SEM-EDX elemental analysis for porous hematite-based photoanodes

Component	Ti/Ti-Fe_2O_3	Ti/Ti-Fe_2O_3-Al_2O_3	Ti/Ti-Fe_2O_3-Al_2O_3-CoPi	FTO/Ti-Fe_2O_3
	%At	%At	%At	%At
Fe	16.05	20.73	16.45	20.13
Ti	12.26 [b]	9.12 [b]	10.27 [b]	0.290 [c]
Al	n/a	1.01	0.68	n/a
P	n/a	n/a	0.520	n/a
Co	n/a	n/a	0.240	n/a
O	71.69	69.13	71.84	75.12
Sn	n/a	n/a	n/a	4.460
Ti/Fe ratio	n/a	n/a	n/a	0.014
Al/Fe ratio	n/a	0.049	0.041	n/a
Co/Fe ratio	n/a	n/a	0.015	n/a

[a] n/a = not available
[b] Ti element was from the Ti felt substrate.
[c] FTO-glass substrate was used to validate the presence of Ti.

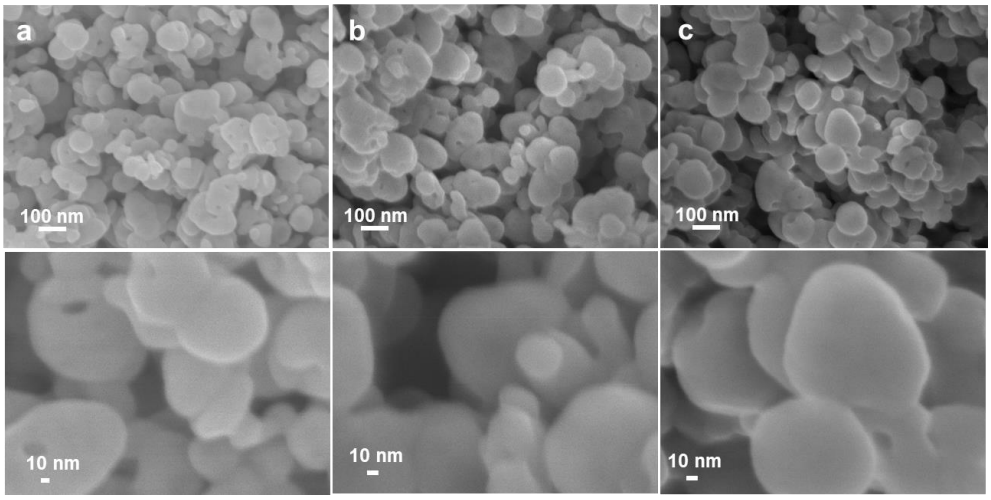

Figure 4.4: Top-view FE-SEM images of (a) Ti/Ti-Fe_2O_3 (b) Ti/Ti-Fe_2O_3-Al_2O_3, and (c) Ti/Ti-Fe_2O_3-Al_2O_3-CoPi at high magnifications.

The morphology of the hematite-based photoanodes was characterized by field emission scanning electron microscopy, confirming the porous structure (Figures 4.3c-f). Top-view and cross-sectional side-view images in high magnification revealed particle size below 100 nm in all samples (Figure 4.4-4.5). Modifications with Al_2O_3 and CoPi did not alter the morphological properties of hematite. EDX elemental mapping images (Figure 4.6) demonstrated the appearance of Al, Co, and P species after modification with the Al_2O_3 layer and CoPi cocatalyst (Table 4.1). Additionally, in the case of Ti doping, the presence of Ti species was observed when utilizing an FTO glass substrate. Diffuse reflectance UV–visible–NIR spectra display no changes in the bandgap energy of hematite (2.1 eV) after the modifications (Figure 4.7). Furthermore, no notable alterations were observed in the X-ray diffraction pattern and Raman vibrational mode of hematite across all samples (Figures 4.8).

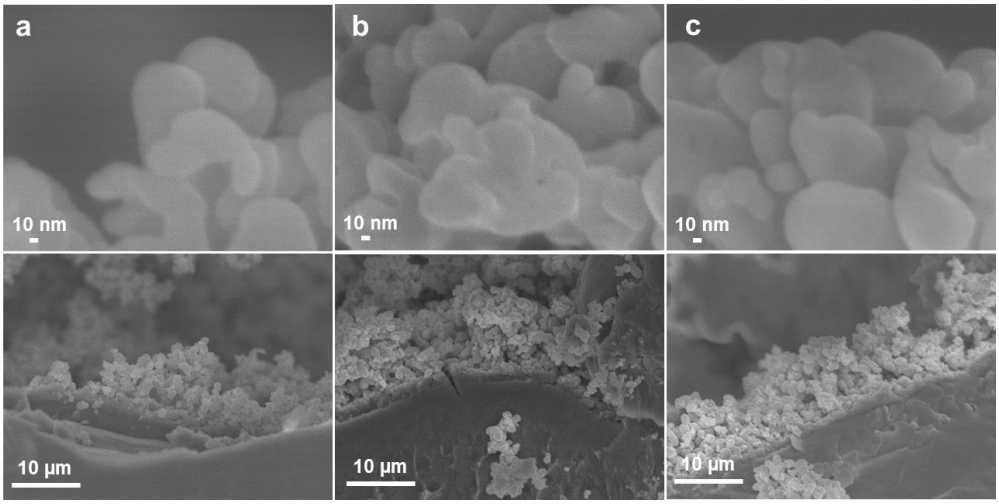

Figure 4.5: Cross-sectional side-view FESEM images of (a) Ti/Ti-Fe_2O_3 (b) Ti/Ti-Fe_2O_3-Al_2O_3, and (c) Ti/Ti-Fe_2O_3-Al_2O_3-CoPi.

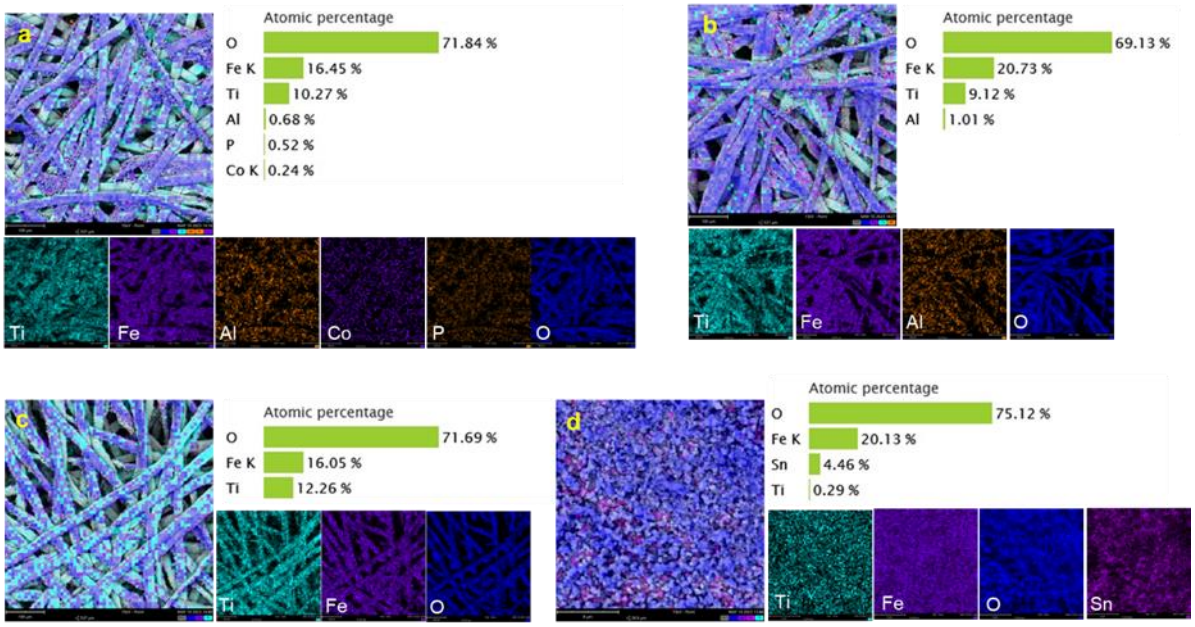

Figure 4.6: SEM-EDX elemental mapping images of hematite photoanodes:(a) Ti/Ti-Fe_2O_3-Al_2O_3-CoPi, (b) Ti/Ti-Fe_2O_3-Al_2O_3, (c) Ti/Ti-Fe_2O_3, and (d) FTO/Ti-Fe_2O_3.

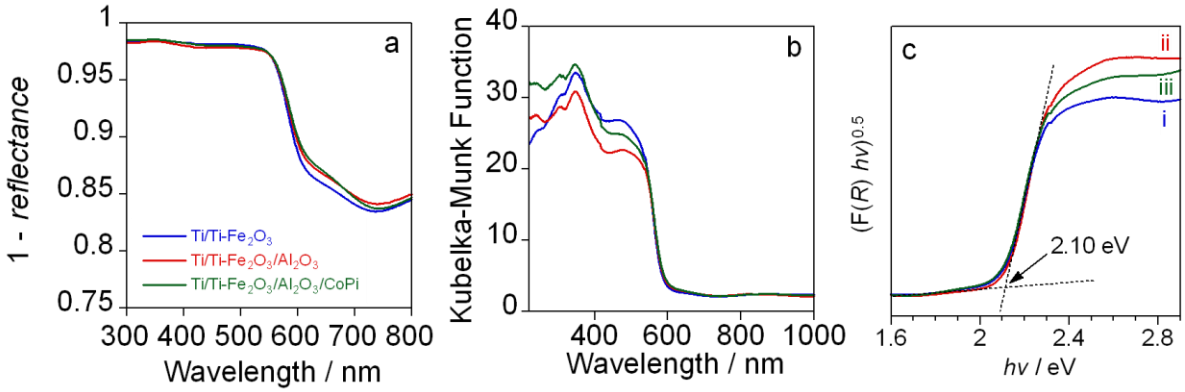

Figure 4.7: Diffuse reflectance UV–visible–NIR spectra of Ti/Ti-Fe_2O_3, Ti/Ti-Fe_2O_3-Al_2O_3, and Ti/Ti-Fe_2O_3-Al_2O_3-CoPi (a) 1 − Reflectance (b) Kubelka-Munk function and (c) Tauc plots.

To provide further evidence of the presence of Al_2O_3 and CoPi, surface analysis was conducted through XPS characterization (Figures 4.9). The oxidation states of the Ti-doped hematite were identified based on the binding energy of Fe^{3+} and Ti^{4+}. Figure 4.10 shows Ti K-edge XANES spectra of FTO/Ti-Fe_2O_3. The spectrum was almost the same as that of $TiFeO_3$ and different from that of TiO_2. This result indicates that Ti species in FTO/Ti-Fe_2O_3 was not segregated but successfully incorporated into the crystal structure of Fe_2O_3. The incorporated Ti species were in the Ti^{4+} oxidation state and coordinated with six-oxygen atoms, similar to Ti species in $TiFeO_3$. In the case of Ti/Ti-Fe_2O_3-Al_2O_3-CoPi, the binding energy at 73.0 eV indicated the presence of Al^{3+}.[21] Additionally, the emergence of Co^{2+} and P in the phosphate group was observed at 780.6 eV and 132.1 eV, respectively, confirming the presence of CoPi.[12] These results provide compelling evidence that the hematite photoanode was successfully modified with Al_2O_3 and CoPi.

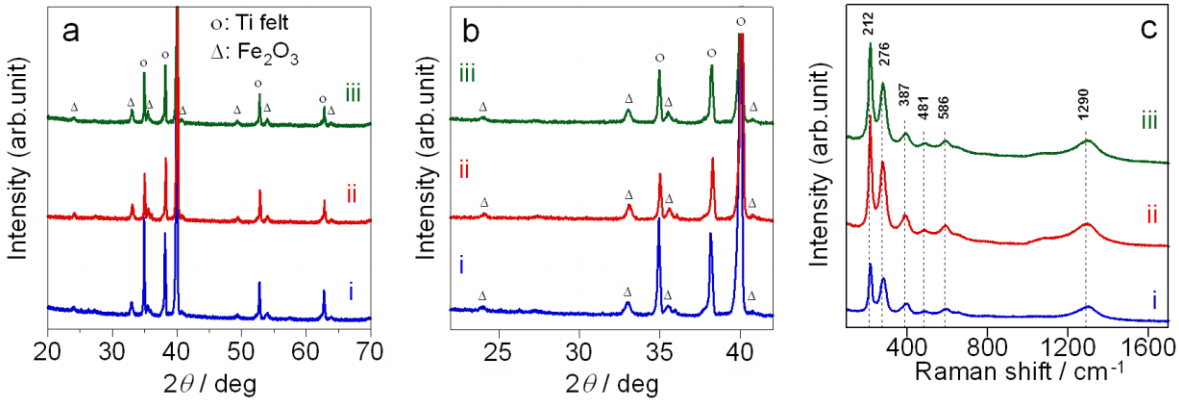

Figure 4.8: (a) X-ray diffraction patterns; (b) its enlargement and (c) Raman spectra of (i) Ti/Ti-Fe_2O_3, (ii) Ti/Ti-Fe_2O_3-Al_2O_3, and (iii) Ti/Ti-Fe_2O_3-Al_2O_3-CoPi.

Figure 4.11 shows the energy diagram of Ti/Ti-Fe_2O_3, Ti/Ti-Fe_2O_3-Al_2O_3, and Ti/Ti-Fe_2O_3-Al_2O_3-CoPi. The modification of Ti-doped Fe_2O_3 with Al_2O_3 and CoPi did not affect a significant change in the position of band alignment. This result is consistent with UV-Vis DRS spectroscopy analysis, confirming that the bandgap energy of Al_2O_3 was almost similar after modification with Al_2O_3 and CoPi.

4.3.2 Photoelectrochemical performance of porous-based hematite photoanodes in conventional PEC system

The PEC properties were initially assessed in a one-compartment cell in 1 M NaOH (pH 13.6) using a conventional three-electrode system under 1 simulated sun (AM 1.5G). After modification, the photocurrent density of the hematite photoanode improved from 0.32 to 0.85 mA cm^{-2} at 1.23 V vs. RHE. The increase in IPCE efficiency was observed from 5.26% to 23.2 % at 340 nm. The modification with Al_2O_3 passivation layers and CoPi co-cocatalysts resulted in improved photocurrent response and IPCE efficiency of porous hematite photoanode (Figures 4.12a-c). Moreover, the onset potential was cathodically shifted from 0.92 to 0.57 V. The enhanced PEC properties can be attributed to the influence of Al_2O_3 and CoPi,

which reduce surface recombination and shift more negative onset potential, respectively.[23,24] Furthermore, Mott-Schottky (Figure 4.12d) and Nyquist plot analyses (Figure 4.13c) were conducted, revealing that the modification with Al_2O_3 and CoPi leads to an increased electron concentration (Table 4.2) and enhanced charge transfer efficiency.

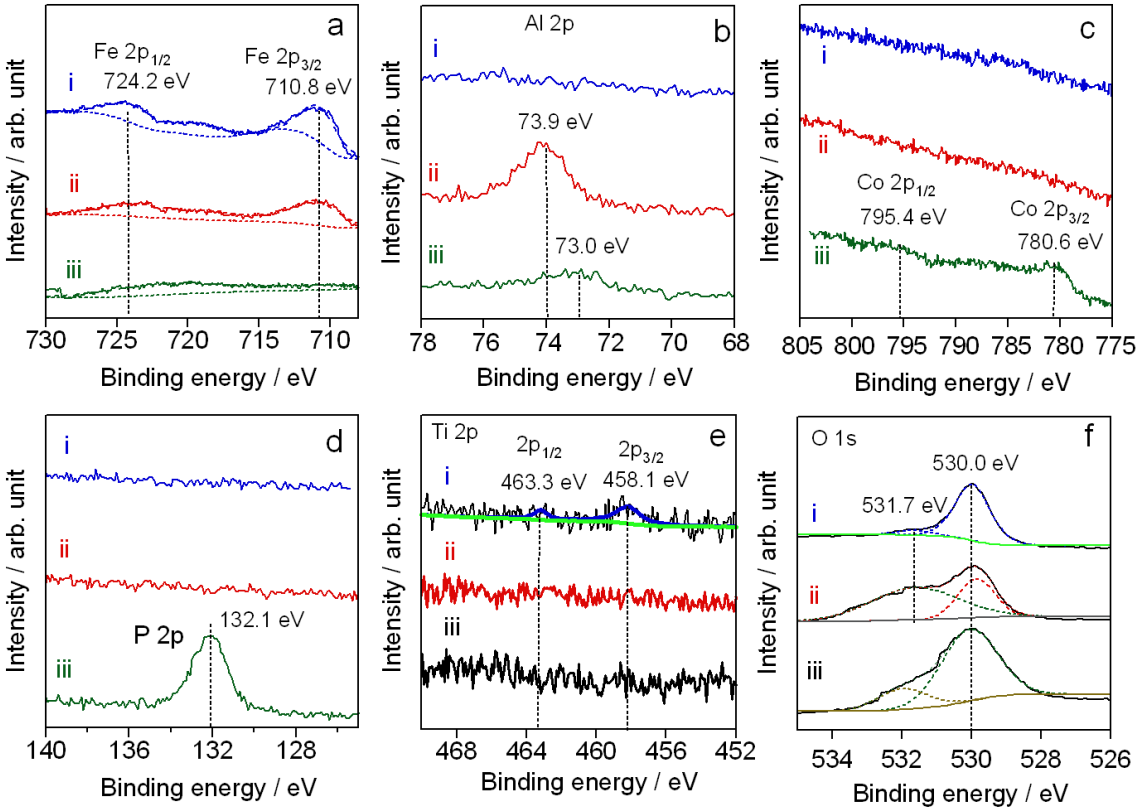

Figure 4.9: Normalized XPS spectra of (a) Fe 2p; (b) Al 2p; (c) Co 2p; (d) P 2p; (e) Ti 2p and (f) TO 1s for (i) Ti/Ti-Fe_2O_3, (ii) Ti/Ti-Fe_2O_3-Al_2O_3, and (iii) Ti/Ti-Fe_2O_3-Al_2O_3-CoPi.

Table 4.2. The donor density of porous hematite-based photoanodes estimated from Mott–Schottky analysis in a conventional PEC system in a one-compartment cell

Photoanodes	N_D / cm^{-3}
Ti/Ti-Fe_2O_3	1.11×10^{21}
Ti/Ti-Fe_2O_3-Al_2O_3	4.61×10^{21}
Ti/Ti-Fe_2O_3-Al_2O_3-CoPi	23.5×10^{21}

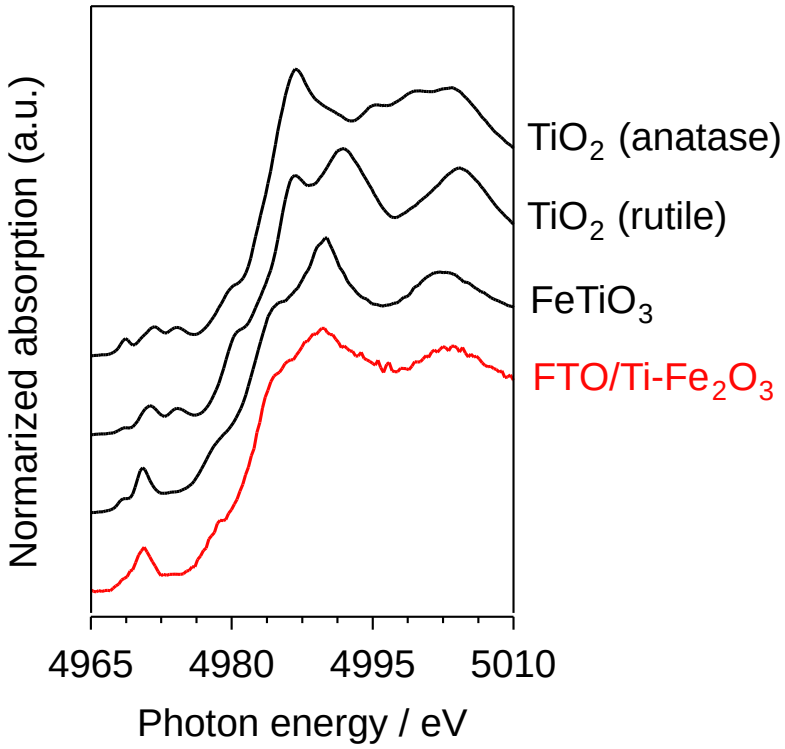

Figure 4.10: Ti K-edge XANES spectra of FTO/Ti-Fe_2O_3.

Table 4.3. The values of conductivity and pH of various electrolyte solutions

Solutions	Conductivity (mS/m)	pH
1 M NaOH	~ 17000	13.45
0.1 M NaOH	~ 2000	12.65
0.01 M NaOH	~ 200	11.80
1 M Na_2SO_4 (adjusted by NaOH)	~ 9000	~ 10.5
1 M Na_2SO_4 (adjusted by NaOH)	~ 9000	~ 9
Ultra-pure water	< 0.1	~ 7

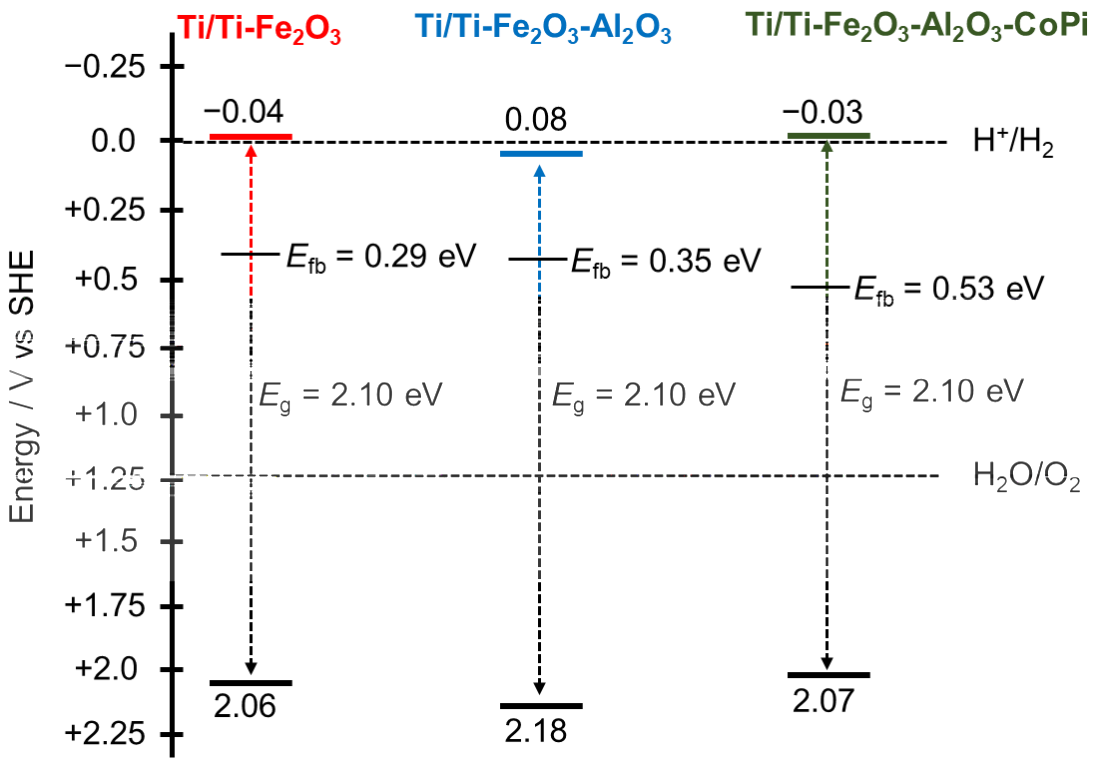

Figure 4.11: Energy diagram of Ti/Ti-Fe_2O_3, Ti/Ti-Fe_2O_3-Al_2O_3, and Ti/Ti-Fe_2O_3-Al_2O_3-CoPi. The valence band maximum (VBM) was determined from ionization energy measurement by PYS. Conduction band maximum (CBM) was obtained from the VBM using the band gap energy (E_g) estimated by UV-Vis DRS measurement. Flat-band potential (E_{fb}) was determined from the Mott-Schottky analysis.

Figure 4.12e presents the linear scan voltammetry for the porous photoanodes in NaOH solutions at different pH levels to verify the alkaline nature of the hematite-based photoanode. The photocurrent response was significantly decreased in low pH, which was observed from 0.85 to 0.03 mA cm^{-2} at 1.23 V vs. RHE (Figure 4.12f). The influence of varying electrolyte pH not only reduces the current density but also induces a positive shift of the onset potential due to the lower stability of the hematite in a less alkaline environment. Notably, the 1 M Na_2SO_4 (pH 9 and 10.5) exhibited a sharp decline in the photocurrent decay and lower photocurrent response compared to 0.01 M NaOH (pH 11) even which had lower conductivity

(Table 4.3). A similar phenomenon was observed in the Ti/Ti-Fe_2O_3-Al_2O_3 photoanode (Figure 4.13b). The photocurrent response was significantly diminished in the mildly alkaline pH. These findings indicate that a high electrolyte pH is more critical than ion conductivity alone for achieving optimal performance of the hematite photoanodes in the conventional PEC system.

4.3.3 Photoelectrochemical performance of porous based hematite photoanodes in AEM-PEC system

We investigated the AEM-PEC water-splitting system, which was designed in a two-compartment cell. In this setup, the photoanode part operated in pure water without the addition of a supporting electrolyte, while the cathode part comprised Hg/HgO reference and Pt counter electrodes immersed in 1 M NaOH solution. To construct the AEM-PEC cell, the porous photoanode was attached to AEM and secured with a gasket to seal the solution side. The assembled unit, known as the MEA (membrane electrode assembly), was then inserted between two gold-plated plates, providing an irradiation area of 1 cm^2 faced the light source. Importantly, the absence of solution crossover in both the photoanode and cathode sections was confirmed. The photocurrent response of the porous hematite-based photoanodes was examined in the AEM-PEC system under 1-sun irradiation as illustrated in Figure 4.14a. The anode compartment was filled with pure water, while the cathode compartment contained 1M NaOH. After modification, the photocurrent density of the porous hematite increased from 0.22 to 0.52 mA cm^{-2} at 1.23 V vs. RHE. The enhancement of IPCE efficiency was obtained from 3.84% to 12.7% at 340 nm. Moreover, the onset potential was cathodically shifted by approximately 0.2 V. The modifications with Al_2O_3 and CoPi significantly enhanced the photocurrent response of porous hematite photoanode (Figures 4.14b-c). The IPCE action analysis revealed that the

porous hematite photoanode in the AEM-PEC system was active under visible irradiation (Figure 4.14d).

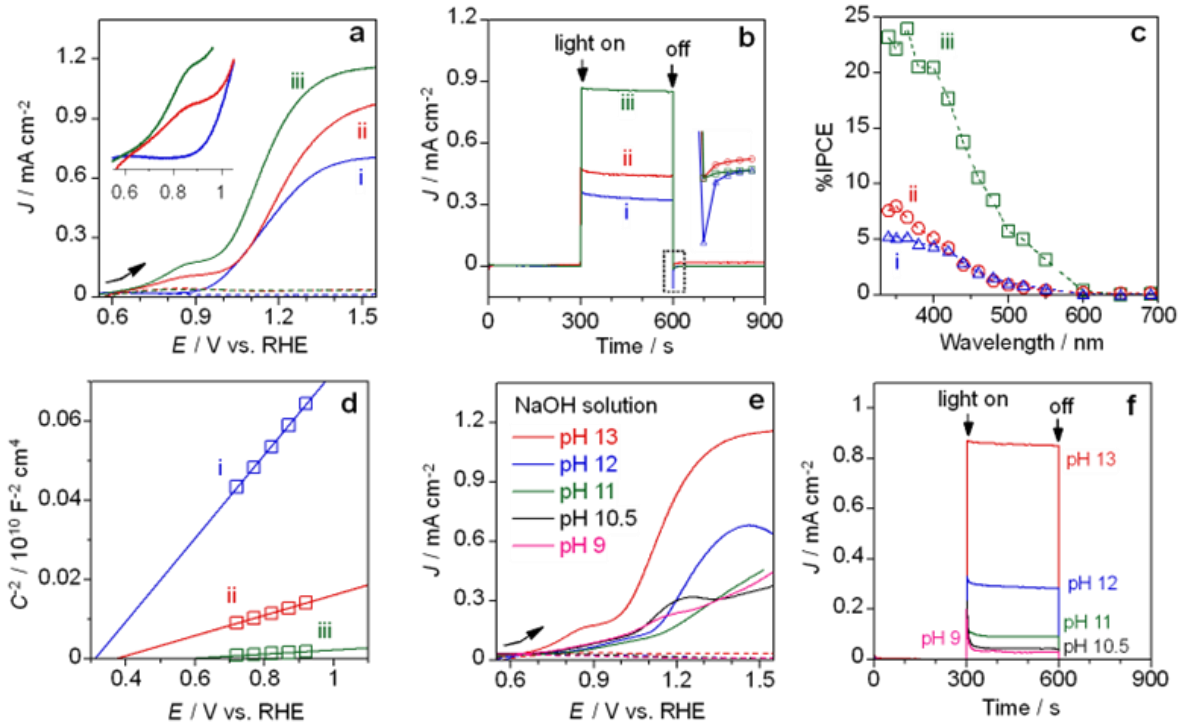

Figure 4.12: PEC properties of (i) Ti/Ti-Fe_2O_3, (ii) Ti/Ti-Fe_2O_3-Al_2O_3, (iii) Ti/Ti-Fe_2O_3-Al_2O_3-CoPi in a conventional liquid system. (a) Current–potential curves under 1-sun irradiation. Dashed lines indicate the curve in the dark. Inset shows onset potential shift more negatively. (b) Photocurrent response at 1.23 V vs. RHE. The inset shows a cathodic transient current once the irradiation is terminated. (c) IPCE action spectra at 1.23 V vs. RHE under irradiation at 340–710 nm. (d) Mott–Schottky plots under dark conditions. PEC properties of Ti/Ti-Fe_2O_3-Al_2O_3-CoPi with various pH of NaOH solutions under 1-sun irradiation; (e) Current–potential curves and (f) photocurrent response at 1.23 V vs. RHE.

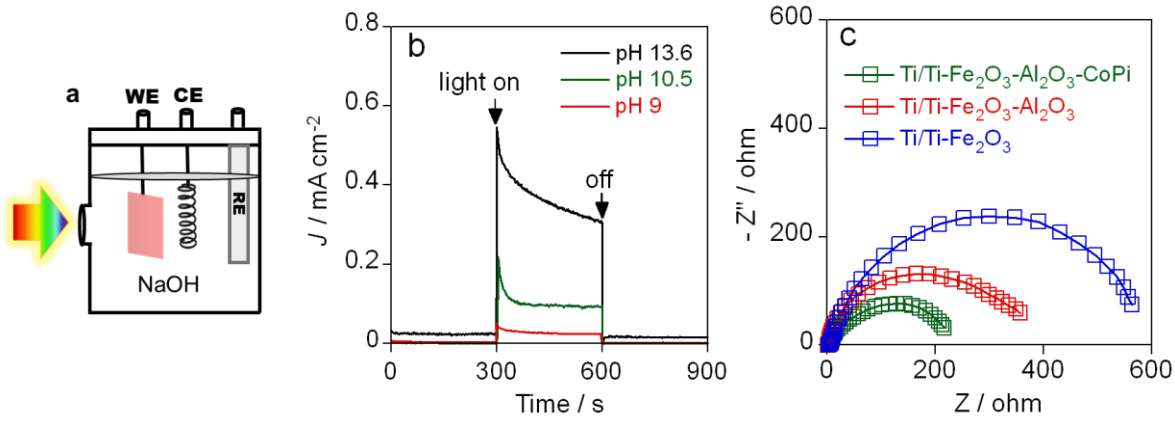

Figure 4.13: (a) Schematic illustration of a conventional PEC system in a one-compartment cell with a WE, Pt CE, and Hg/HgO RE (b) Photocurrent response of Ti/Ti-Fe_2O_3-Al_2O_3 in NaOH solutions with different pH values and (c) EIS spectra at 1.23 V vs. RHE under 1-sun irradiation.

The visible light response was up to approximately 600 nm, which corresponds to the optical band gap of Fe_2O_3 (~2.1 eV). Remarkably, to the best of our knowledge, this absorption range represents the broadest coverage of the visible spectrum among the reported MEA with porous photoanodes (WO_3 and $BiVO_4$).[4–6]

After careful consideration, the conductivity and pH of water in the photoanode part were increased before and after the reaction (Table 4.4). This phenomenon is likely attributed to the elution of OH^- from the AEM as well as the transport of OH^- ions from the cathode side to the photoanode side through the AEM. Subsequently, the effect of NaOH concentrations in the cathode part on the AEM-PEC properties was investigated. For both Ti/Ti-Fe_2O_3-Al_2O_3 and Ti/Ti-Fe_2O_3-Al_2O_3-CoPi photoanodes, decreasing the NaOH concentrations in the cathode compartment decreased the conductivity and pH of the photoanode water after the reactions (Table 4.5-4.6), consequently decreased the photocurrent response of the Ti/Ti-Fe_2O_3-Al_2O_3 during the reaction (Figure 4.15). In the case of Ti/Ti-Fe_2O_3-Al_2O_3-CoPi photoanode, the current density at 1.23 V vs. RHE decreased from 0.52 to 0.34 mA cm^{-2} by changing the

cathode NaOH concentration from 1 M to 0.1 M (Figures 4.14e-f). The onset potentials were nearly independent of the cathode electrolyte. Interestingly, a photocurrent response was still observed even when the pH in the photoanode compartment was approximately 9. This demonstrates that hematite-based MEA can operate even under weak alkaline conditions since the photoanode is directly contact with AEM, in contrast to conventional PEC systems that require high concentrations of OH^- ions.

Table 4.4. The values of conductivity and pH of water in the photoanode part in the AEM-PEC system in two-compartment cells

Photoanodes	Water in the photoanode part				
	Conductivity (mS/m)			pH	
	Fresh[a]	Before[b]	After	Before	After
Ti/Ti-Fe_2O_3	0.062	0.238	9.250	~ 7.07	~ 10.4
Ti/Ti-Fe_2O_3-Al_2O_3	0.061	0.234	13.33	~ 7.00	~ 10.5
Ti/Ti-Fe_2O_3-Al_2O_3-CoPi	0.053	0.203	4.33	~ 6.65	~ 10.2

[a] "Fresh" indicates the conductivity of ultrapure water before incorporating it into the photoanodes.

[b] "Before" indicates the conductivity of ultrapure water after incorporating it into the photoanodes. The value was slightly increased, probably, due to the effect of OH^- species from AEM.

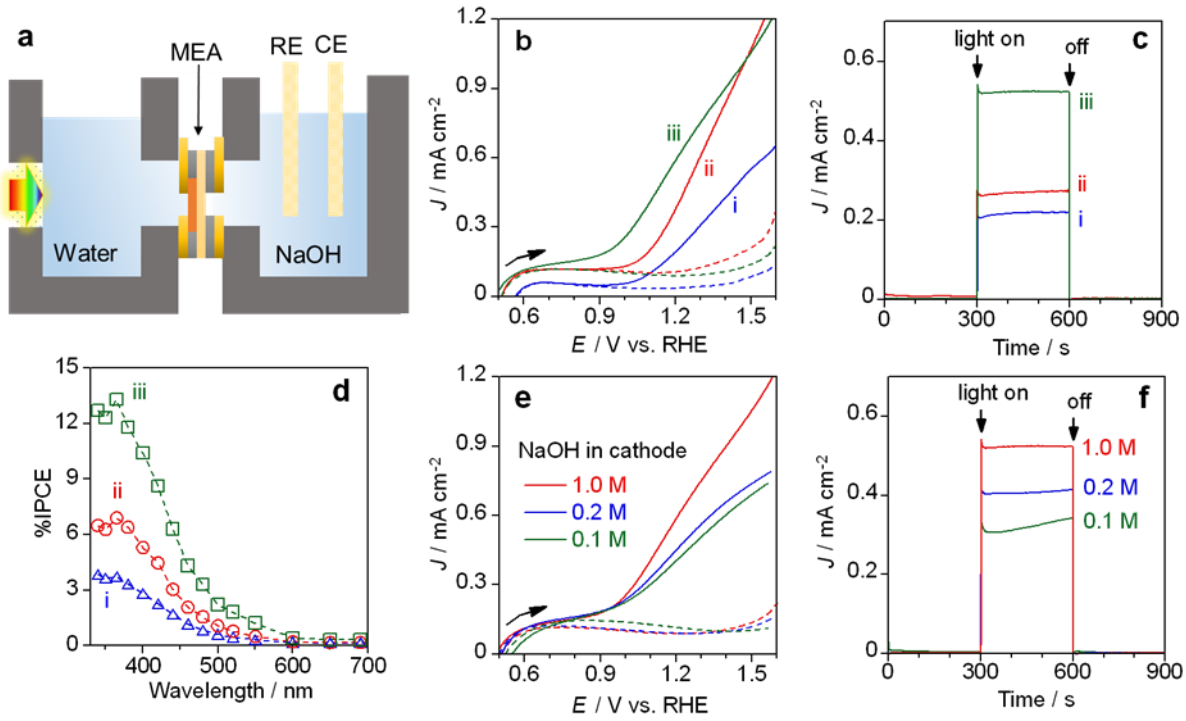

Figure 4.14: (a) AEM-PEC system of (i) Ti/Ti-Fe_2O_3, (ii) Ti/Ti-Fe_2O_3-Al_2O_3, (iii) Ti/Ti-Fe_2O_3-Al_2O_3-CoPi in a two-compartment cell under AM 1.5G irradiation. The photoanode part contains water without liquid electrolytes. Working electrode faced light source with irradiation area of 1 cm^2. The conductivity and pH of water were initially < 0.1 mS/m and ~ 7, respectively. Cathode parts consist of NaOH solution, Pt counter electrode, and Hg/HgO reference electrode. (b) current–potential curve. Dashed lines indicate current in the dark. (c) current–time curve at 1.23 V vs. RHE. Irradiation was performed from 300s to 600s. (d) IPCE action spectra at 1.23 V vs. RHE. AEM-PEC system with different concentrations of electrolyte solution in the cathode part (e) current–potential curve. (f) current–time curve at 1.23 V vs. RHE.

Table 4.5. The values of conductivity and pH of water for the Ti/Ti-Fe_2O_3-Al_2O_3-CoPi photoanode in the AEM-PEC system with different NaOH concentrations in the cathode part

NaOH in the cathode part	Water in the photoanode part				
	Conductivity (mS/m)			pH	
	Fresh[a]	Before[b]	After	Before	After
1 M	0.053	0.203	4.330	~ 6.65	~ 10.2
0.2 M	0.063	0.171	1.664	~ 6.68	~ 9.23
0.1 M	0.058	0.082	1.241	~ 6.62	~ 8.84

[a] "Fresh" indicates the conductivity of ultrapure water before incorporating it into the photoanodes.

[b] "Before" indicates the conductivity of ultrapure water after incorporating it into the photoanodes. The value was slightly increased, probably, due to the effect of OH^- species from AEM.

Table 4.6. AEM-PEC system. The values of conductivity and pH of water for the Ti/Ti-Fe_2O_3-Al_2O_3 photoanode in the AEM-PEC system with different NaOH in the cathode part

NaOH in the cathode part	Water in the photoanode part				
	Conductivity (mS/m)			pH	
	Fresh[a]	Before[b]	After	Before	After
1 M	0.062	0.238	9.250	~ 7.07	~ 10.4
0.2 M	0.052	0.149	7.010	~ 6.54	~ 8.86
0.1 M	0.041	0.117	0.887	~ 6.91	~ 8.84

[a] "Fresh" indicates the conductivity of ultrapure water before incorporating it into the photoanodes.

[b] "Before" indicates the conductivity of ultrapure water after incorporating it into the photoanodes. The value was slightly increased, probably, due to the effect of OH^- species from AEM.

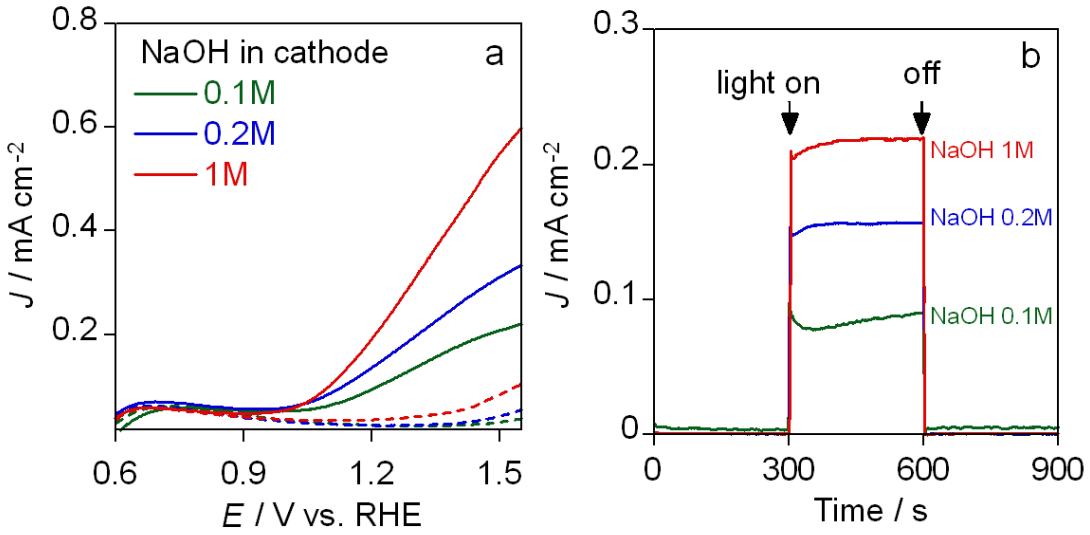

Figure 4.15: AEM-PEC system of Ti/Ti-Fe_2O_3-Al_2O_3 in a two-compartment cell in NaOH solutions with different pH under 1-sun irradiation. (a) Current–potential curve, with dashed lines indicating current in the dark. (b) Photocurrent response at 1.23 V vs. RHE, with irradiation performed from 300 to 600 s.

Compared to the photocurrent of 0.85 mA cm^{-2} obtained in the conventional 1 M NaOH at 1.23 V vs. RHE, the AEM-PEC system using pure water in the photoanode side exhibited a photocurrent of 0.52 mA cm^{-2}. This observation suggests that the direct penetration of 1 M NaOH into the interconnected porous hematite is more favorable in promoting water oxidation reactions compared to using water without liquid electrolytes.

We further investigated the effect of neutral 1 M Na_2SO_4 in the cathode electrolyte (Figure 4.16). When 1 M Na_2SO_4 was used in the cathode electrolyte, the photocurrent response was small even under 385-nm light irradiation. The current-time curve exhibited a decay in a photocurrent and increased after the termination of irradiation. The absence of OH^- ions in the cathode compartment significantly decreased the photocurrent response. It speculates that the transport of OH^- ions from the neutral cathode to the photoanode side was insufficient.

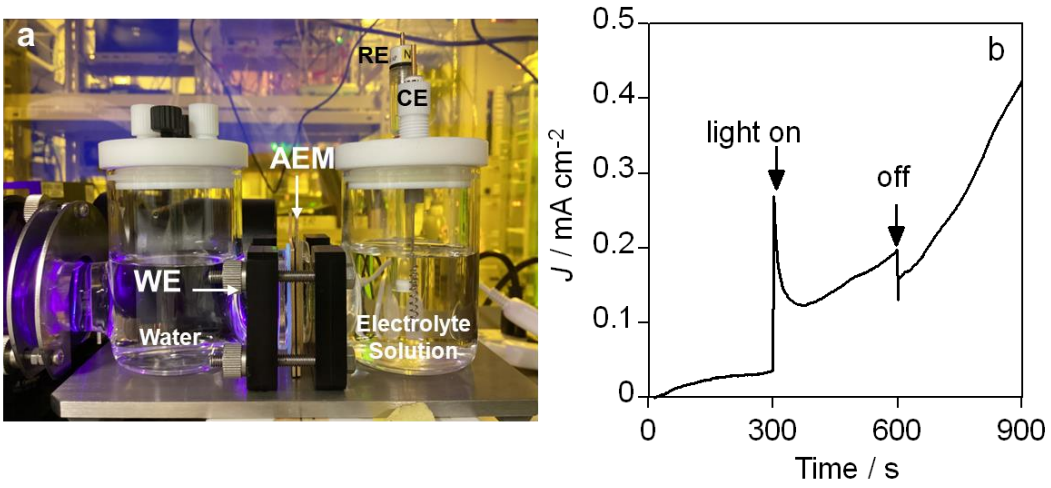

Figure 4.16: (a) AEM-PEC system of Ti/Ti-Fe_2O_3 in two-compartment cells. The photoanode part contains water without liquid electrolytes (conductivity <0.1 mS/m, pH ~7). Cathode parts consist of 1 M Na_2SO_4 solution (conductivity ~9000 mS/m, pH ~7), Pt CE, and Ag/AgCl RE. (b) Photocurrent response at 1.23 V vs. RHE under 385-nm irradiation (I_0 ~30 mW cm^{-2}).

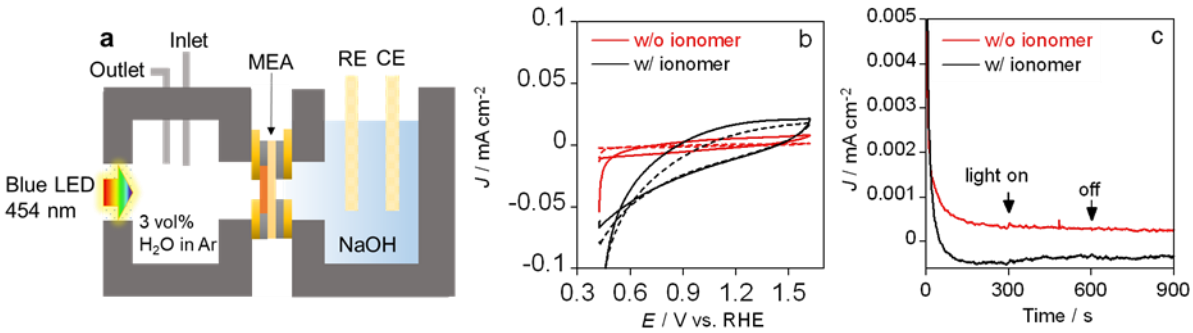

Figure 4.17: (a) Vapor-fed AEM-PEC system for the Ti/Ti-Fe_2O_3 photoanode under Ar gas flow with 3 vol% water vapor, while cathode part consists of 1 M NaOH solution, Pt CE, and Hg/HgO RE. (b) Current–potential curves and (c) photocurrent response at 1.23 V vs. RHE under blue LED 454-nm irradiation (I_0 ~10.7 mW cm^{-2}). The hematite photoanode was coated with Fumion ionomer solution (FAA-3-SOLUT-10, 3.32 mg cm^{-2}) and dried at 80 °C. The photocurrent response was not observed even with the ionomer coating. The hydration of the photoanode surface with the ionomer was insufficient to achieve the PEC reaction.

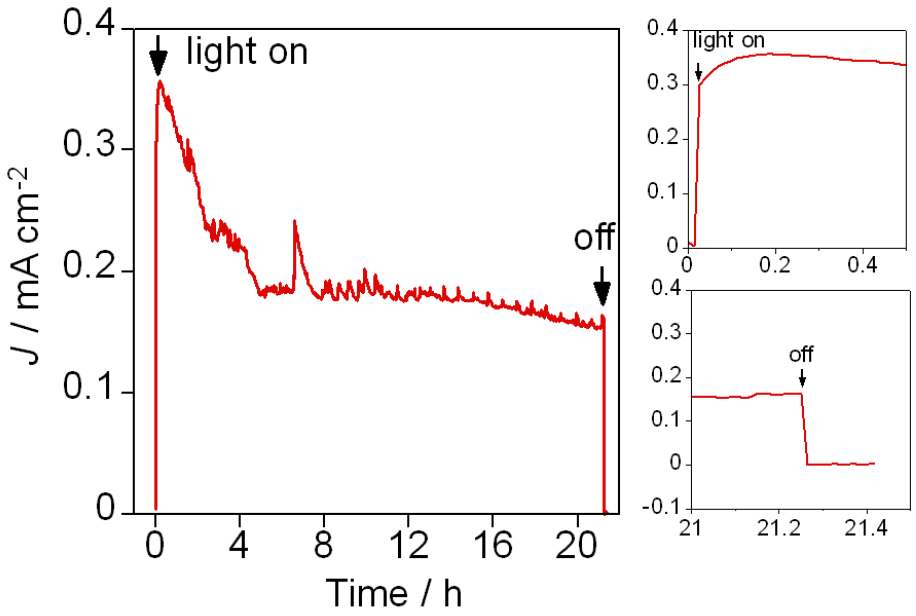

Figure 4.18. Photocurrent stability measurement of Ti/Ti-Fe_2O_3-Al_2O_3-CoPi at 1.23 V vs. RHE under 1-sun irradiation in the AEM-PEC system within 21 h. Pure water was supplied to the photoanode compartment. The conductivity and pH of water were initially < 0.1 mS/m and ~ 7, respectively. The cathode parts consist of a Pt counter and Hg/HgO reference electrodes in 0.1 M NaOH solution. Insets show the current after on-off irradiation. The photocurrent response of Ti/Ti-Fe_2O_3-Al_2O_3-CoPi was diminished from 0.30 to 0.16 mA cm^{-2} at 1.23 V vs. RHE after 21 hours of irradiation and the stability reached about 53%.

(A)

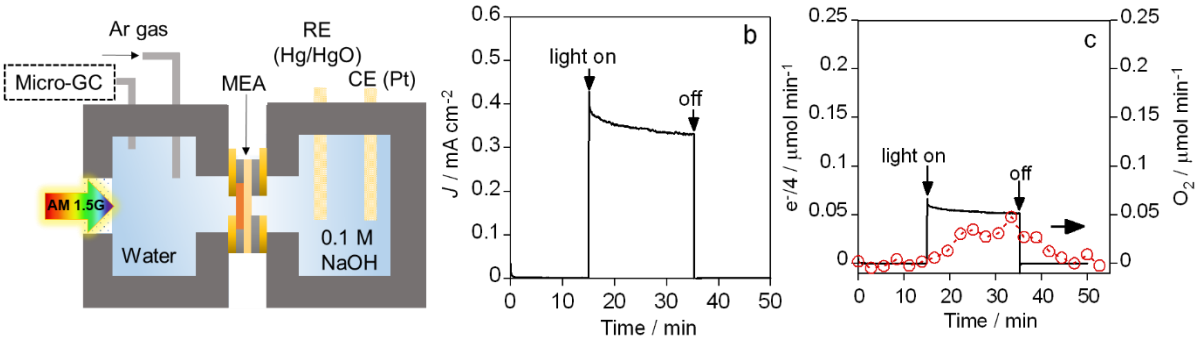

(B)

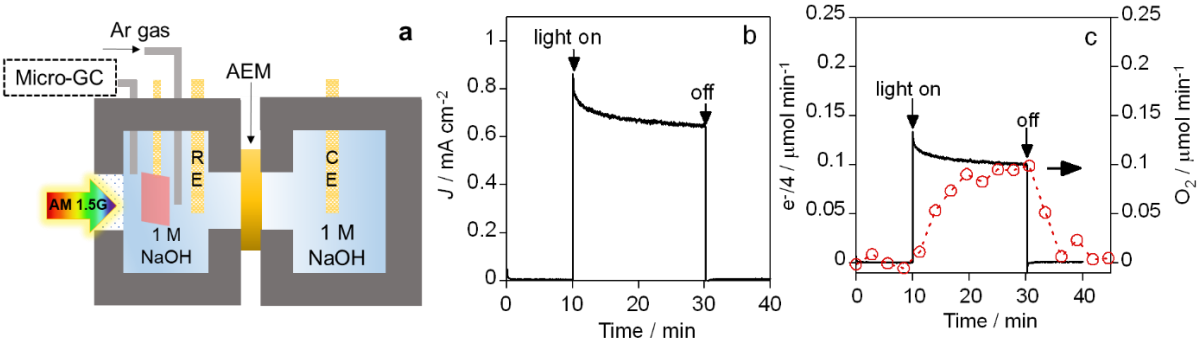

Figure 4.19. Oxygen evolution reaction using Ti/Ti-Fe_2O_3-Al_2O_3-CoPi in (A) water and (B) 1 M NaOH using AEM-PEC system under 1-sun irradiation (AM 1.5G, 100 mW cm^{-2}): (a) Schematic illustration, (b) Current–time curve at 1.23 V vs. RHE, and (c) Time course of O_2 evolution rate with $e^-/4$.

Additionally, the experiment using a vapor-fed AEM-PEC system was conducted by replacing pure water with water vapor, which resulted in almost no photocurrent response (Figure 4.17). This finding implies that the proper hydration of the porous hematite photoanode surface is critical to facilitate proton-coupled electron transfer and charge transport within the AEM-PEC system. Besides, it is noteworthy that the AEM-PEC system operates within alkaline-free water characterized by low pH and low conductivity. This property distinguishes it from conventional PEC systems, which require highly alkaline conditions with a pH exceeding 12. The photocurrent OER response of Ti/Ti-Fe_2O_3-Al_2O_3-CoPi lasted for more than

20 h, indicating pro-longed stability (Figure 4.18). In the OER measurement, the O_2 evolution rate was ~0.05 and 0.09 μmol min^{-1} cm^{-2} with the Faradaic efficiency (FE) of 92.4% and 94.1%, respectively (Figure 4.19). The AEM-PEC system can achieve the PEC reactions even under weak alkaline conditions due to the locally alkaline microenvironment at the photoanode, which directly interfaces with the AEM.

4.4 Conclusions

In conclusion, a membrane electrode assembly (MEA) that incorporates porous α-Fe_2O_3 (hematite)-based photoanodes integrated with an anion exchange membrane (AEM) has been successfully fabricated. This study demonstrates AEM-PEC water splitting using pure water, without supporting electrolytes, over porous hematite photoanodes under visible light irradiation. This novel system can operate the PEC reaction with photocurrent response, even under low-conductivity and near-neutral conditions (~1 mS/m and pH ~9). The AEM-PEC device proves to be an effective and appropriate system for utilizing hematite-based photoanodes in water-splitting reactions under visible light response extending up to 600 nm, surpassing that of previous reports on porous photoelectrode for PEC reaction with solid electrolyte membrane. Importantly, the AEM-PEC system is nonidentical to conventional PEC using liquid electrolytes, where hematite photoanodes are active only in strongly alkaline solutions. The synergistic combination of the porous photoanode and a solid electrolyte membrane successfully mitigates the mass-transport limitation in pure water without the presence of supporting electrolytes. The integration of the porous hematite photoanode with AEM for PEC water splitting in liquid electrolyte-free conditions holds significant potential in developing cost-effective devices for sustainable fuel production that harness solar energy.

References

1. Tilley, S. D., Cornuz, M., Sivula, K. & Grätzel, M. Light-Induced Water Splitting With Hematite: Improved Nanostructure and Iridium Oxide Catalysis. *Angew. Chemie - Int. Ed.* **49**, 6405–6408 (2010).
2. Warren, S. C. *et al.* Identifying Champion Nanostructures for Solar Water-Splitting. *Nat. Mater.* **12**, 842–849 (2013).
3. Seger, B. & Kamat, P. V. Fuel Cell Geared in Reverse: Photocatalytic Hydrogen Production using a TiO_2/Nafion/Pt Membrane Assembly with No Applied Bias. *J. Phys. Chem. C* **113**, 18946–18952 (2009).
4. Amano, F. *et al.* Vapor-Fed Photoelectrolysis of Water at 0.3 V using Gas-Diffusion Photoanodes of $SrTiO_3$ Layers. *Sustain. Energy Fuels* **4**, 1443–1453 (2020).
5. Zafeiropoulos, G., Johnson, H., Kinge, S., Van De Sanden, M. C. M. & Tsampas, M. N. Solar Hydrogen Generation from Ambient Humidity Using Functionalized Porous Photoanodes. *ACS Appl. Mater. Interfaces* **11**, 41267–41280 (2019).
6. Amano, F., Shintani, A., Mukohara, H., Hwang, Y. M. & Tsurui, K. Photoelectrochemical Gas-Electrolyte-Solid Phase Boundary for Hydrogen Production from Water Vapor. *Front. Chem.* **6**, 1–10 (2018).
7. Rongé, J. *et al.* Air-Based Photoelectrochemical Cell Capturing Water Molecules from Ambient Air for Hydrogen Production. *RSC Adv.* **4**, 29286–29290 (2014).
8. Ta, C. X. M., Akamoto, C., Furusho, Y. & Amano, F. A Macroporous-Structured WO_3/Mo-Doped $BiVO_4$ Photoanode for Vapor-Fed Water Splitting under Visible Light Irradiation. *ACS Sustain. Chem. Eng.* **8**, 9456–9463 (2020).
9. Amano, F., Mukohara, H., Shintani, A. & Tsurui, K. Solid Polymer Electrolyte-Coated Macroporous Titania Nanotube Photoelectrode for Gas-Phase Water Splitting. *ChemSusChem* **12**, 1925–1930 (2019).

10. Amano, F. *et al.* Photoelectrochemical Homocoupling of Methane under Blue Light Irradiation. *ACS Energy Lett.* **4**, 502–507 (2019).

11. Apriandanu, D. O. B., Nakayama, S., Shibata, K. & Amano, F. Ti-Doped Fe_2O_3 Photoanodes on Three-Dimensional Titanium Microfiber Felt Substrate for Photoelectrochemical Oxygen Evolution Reaction. *Electrochim. Acta* **456**, 142434 (2023).

12. Yi, S. S., Wulan, B. R., Yan, J. M. & Jiang, Q. Highly Efficient Photoelectrochemical Water Splitting: Surface Modification of Cobalt-Phosphate-Loaded Co_3O_4/Fe_2O_3 p–n Heterojunction Nanorod Arrays. *Adv. Funct. Mater.* **29**, 1–9 (2019).

13. Liardet, L., Katz, J. E., Luo, J., Grätzel, M. & Hu, X. An Ultrathin Cobalt-Iron Oxide Catalyst for Water Oxidation on Nanostructured Hematite Photoanodes. *J. Mater. Chem. A* **7**, 6012–6020 (2019).

14. Pourbaix, M. Atlas of Electrochemical Equilibria in Aqueous Solutions. *NACE* (1966).

15. Zhang, J., Zhang, Q. & Feng, X. Support and Interface Effects in Water-Splitting Electrocatalysts. *Adv. Mater.* **31**, 1–19 (2019).

16. Henkensmeier, D. *et al.* Overview: State-of-the Art Commercial Membranes for Anion Exchange Membrane Water Electrolysis. *J. Electrochem. Energy Convers. Storage* **18**, (2021).

17. Zhang, W. *et al.* Studies on Anion Exchange Membrane and Interface Properties by Electrochemical Impedance Spectroscopy: The Role of pH. *Membranes (Basel).* **11**, (2021).

18. Kuppusamy, H. G., Dhanasekaran, P., Nagaraju, N. & Neeshma, M. Anion Exchange Membranes for Alkaline Polymer Electrolyte. *Materials (Basel).* **15**, 5601 (2022).

19. Caretti, M. *et al.* Transparent Porous Conductive Substrates for Gas-Phase Photoelectrochemical Hydrogen Production. *Adv. Mater.* **35**, (2023).

20. Apriandanu, D. O. B., Nomura, S., Nakayama, S., Tateishi, C. & Amano, F. Effect of Two-Step Annealing on Photoelectrochemical Properties of Hydrothermally Prepared Ti-Doped Fe_2O_3 Films. *Catal. Today* **411**–**412**, 113826 (2023).

21. Fan, Z., Xu, Z., Yan, S. & Zou, Z. Tuning The Ion Permeability of An Al_2O_3 Coating Layer on Fe_2O_3 Photoanodes for Improved Photoelectrochemical Water Oxidation. *J. Mater. Chem. A* **5**, 8402–8407 (2017).

22. Carroll, G. M. & Gamelin, D. R. Kinetic Analysis of Photoelectrochemical Water Oxidation by Mesostructured Co-Pi/α-Fe_2O_3 Photoanodes. *J. Mater. Chem. A* **4**, 2986–2994 (2016).

23. Liu, R., Zheng, Z., Spurgeon, J. & Yang, X. Enhanced Photoelectrochemical Water-Splitting Performance of Semiconductors by Surface Passivation Layers. *Energy Environ. Sci.* **7**, 2504–2517 (2014).

24. Sivula, K., Le Formal, F. & Grätzel, M. Solar Water Splitting: Progress using Hematite (α-Fe_2O_3) Photoelectrodes. *ChemSusChem* vol. 4 432–449 (2011).

Chapter 5. General Conclusions

This thesis studied the development method on the preparation of hematite photoanode with enhanced photoelectrochemical (PEC) properties for water splitting. The main result is concluded as follows.

Firstly, Ti-doped Fe_2O_3 was treated by a two-step annealing condition: air calcination at 873 K and subsequent annealing under argon at 473 K. The photocurrent response of the sample with additional annealing in argon was higher than that without the treatment. The two-step annealed sample with optimized Ti doping exhibited a photocurrent density of 0.55 mA cm^{-2} at 1.50 V vs. RHE, which was approximately three times higher than that of FTO/Ti-Fe_2O_3 calcined in air. As supported by Diffuse reflectance UV-visible–NIR spectroscopy, the two-step annealed sample showed the highest absorption in the NIR region, which indicates the highest electron concentration. Additionally, four-point probe resistivity measurements confirmed the improved electrical conductivity on the sample with a two-step annealing treatment. Two-step annealing treatment is effective for Ti-doped Fe_2O_3 to produce higher PEC properties under visible light irradiation. The increased photocurrent density is attributed to the simultaneous enhancement of donor density and conductivity.

Secondly, the effect of different conductive substrates on the PEC properties of hematite photoanodes was discussed. Ti-doped Fe_2O_3 films were prepared on three-dimensional and conventional two-dimensional substrates The larger specific surface area of the 3D macroporous Ti felt produced the highest loading amount and a thinner Ti-doped Fe_2O_3 layer. High-loading amounts increase photoabsorption. Thin layers shorten electron transport distance. The thickness of the hematite layer was sufficiently obtained with the appropriate loading amount. As concluded previously, Ti^{4+} doping and two-step annealing enhanced the electrical conductivity, resulting in a larger charge-diffusion length than the thickness of the

semiconductor layer, which provided less recombination. Therefore, the PEC properties increase. Additionally, the IPCE of Ti-felt/Ti- Fe_2O_3 was not dependent on irradiance owing to sufficient light absorption, even at low light intensity, while the lower IPCE of FTO/Ti-Fe_2O_3 at low light intensities can be attributed to insufficient light absorption due to the lower loading of Fe_2O_3.

Thirdly, the macroporous photoanode on the 3D conductive substrate was implemented in the membrane electrode assembly systems for mass-transport-limited reactions. The porous hematite-based photoanodes have succeeded in the AEM-PEC water splitting reaction without liquid electrolytes under visible light irradiation for the first time. AEM-PEC system is nonidentical to the conventional PEC, which operates under weak alkaline conditions owing to the contact with AEM. The absorption shows the broadest coverage of the visible spectrum among the reported MEA with porous photoanodes (WO_3 and $BiVO_4$).

In summary, the author proposed the preparation of hematite photoanode with better PEC properties. In the case of two-step annealing treatments, the higher photocurrent response is attributed to the simultaneous increase in the donor density and the electrical conductivity. For the effect of different conductive substrates, it is found that better PEC properties of hematite photoanode were observed because the macroporous 3D Ti felt generates hematite with a moderate layer and higher loading amount per geometric area compared to the conventional 2D FTO-glass. In the development of porous hematite photoanode as membrane electrode assembly, the synergistic combination of the porous photoanode and a solid electrolyte membrane successfully mitigates the mass-transport limitation in pure water without the presence of supporting electrolytes. Finally, the 3D-conductive substrate is promising for the preparation of Fe_2O_3 photoanodes with improved PEC activity for solar-to-chemical conversion.

Acknowledgments

اَلْحَمْدُ للهِ رَبِّ الْعالَمِينَ

The work presented in this thesis was conducted at the Department of Chemical and Environmental Engineering, Graduate School of Environmental Engineering, The University of Kitakyushu from 2020 to 2022 and at the Department of Applied Chemistry for Environment, Graduate School of Urban Environmental Sciences, Tokyo Metropolitan University from 2022 to 2023 under the supervision of Professor Fumiaki Amano. Firstly, I would like to express my sincere gratitude to my supervisor, Professor Fumiaki Amano, for providing me with an enormous opportunity to join his research group as a PhD student. It is a great honor to develop my understanding, learn many things, and work with an advanced research facility in his laboratory that I have never experienced previously. Great thanks for all his kind guidance, limitless support, transferred knowledge, and valuable advice throughout the entire parts of my PhD study. Most of all, I am immensely grateful for believing in me and always supporting me to be better, as a researcher. The whole impact is highly important for my academic career in the future.

I am deeply indebted to Professor Kenji Asami, Professor Katsutoshi Yamamoto, Professor Lee Seung Woo, and Professor Koji Takasu for their constructive advice and helpful discussion in my Doctoral Thesis. I am extremely obliged to Mr. Yoshiyuki Furusho and Ms. Chau Xuan Minh Ta, for their kind guidance at the commencement of my research activity and my daily life in Japan. Additionally, I am very grateful to Mr. Satoshi Nakayama, Mr. Kento Shibata, Mr. Shinpei Nomura, and Mr. Chihiro Tateishi, who have been involved in the collaboration of the research activity presented in Chapter 2 and Chapter 3. Thanks are made to my all-Indonesian mates at the University of Kitakyushu, especially to Adessarman Muhammad Sahlan M.Eng,

Acknowledgmets

Dr. Siswanti Zuraida, Dr. Treza Chandra Julian, Dr. Bimasetyaji Surya Ramadhan, Dr. Athina Ardyanto. I wish them all good luck and success.

I am very grateful to all academic staff at the Advanced Catalysis Laboratory, the Department of Applied Chemistry for Environment, Graduate School of Urban Environmental Sciences, Tokyo Metropolitan University; Dr. Kosuke Beppu, Dr. Surya Prataph Singh, Dr. Takuya Okazaki, and Mrs. Tomoko Bessho for their kind support and useful discussion. I am indebted to the members of the Advanced Catalysis Laboratory led by Professor Fumiaki Amano; Mr. Keisuke Tsushiro, Mr. Rizki Marcony Surya, Mr. Souta Suzuki, Mr. Kazuki Obigane, Mr. Kohta Nomoto, Mr. Kazuma Enomoto, and Mr. Shimon Hirayama. I wish them all good luck with their study. Special Thanks should be made to Professor Tetsuya Shishido at Tokyo Metropolitan University for N_2 adsorption-desorption measurement.

I greatly appreciate the Japanese Government (MEXT) Scholarship for the financial support of my PhD study.

Last but not least, I would like to express my lovely gratitude to my wife, Mrs. Sri Hayati, and my son, Ryoichi Zian Elfathan Asshauqi as well as all my family in Indonesia, in particular to my fathers, my mothers, my sisters, and my brothers for all their continuous support, endless patience, and sincere prayer with heart. Also, I would like to thank all Indonesian communities in Kitakyushu and Hachioji as well as those who indirectly helped me physically and financially during my PhD study and living in Japan. May Allah SWT bless you all with success, health, and happiness now and always.

Academic Activities

Papers

1. **Apriandanu, D. O. B.**, Nakayama, S., Shibata, K. & Amano, F. Ti-doped Fe_2O_3 photoanodes on three-dimensional titanium microfiber felt substrate for photoelectrochemical oxygen evolution reaction. *Electrochim. Acta* 456, (2023), 142434.
2. **Apriandanu, D. O. B.**; Nomura, S.; Nakayama, S.; Tateishi, C.; Amano, F. Effect of Two-Step Annealing on Photoelectrochemical Properties of Hydrothermally Prepared Ti-Doped Fe_2O_3 Films. *Catal. Today*, 411–412, (2023), 113826.
3. **Apriandanu, D. O. B.**, Surya, R. M., Beppu, K. & Amano, F. Anion Exchange Membrane Photoelectrochemical (AEM-PEC) Water Splitting Using Porous Hematite Photoanodes. Submitted. *ACS Applied Energy Materials*.

Presentations

1. **Apriandanu, D. O. B.**, Surya, R. M. & Amano, F., Oral presentation, Anion Exchange Membrane Photoelectrochemical Water Splitting Using Porous Hematite Photoanodes, The 19th Korea-Japan Symposium on Catalysis (19JKSC), May 15-17 2023, Seoul (South Korea).
2. **Apriandanu, D. O. B.**, Beppu, K. & Amano, F., Oral presentation, Ti-doped Fe_2O_3 Photoanodes on Three-Dimensional Titanium Microfiber Felt Substrate for Photoelectrochemical Oxygen Evolution, The 41st Symposium on Solid State and Surface Photochemistry (SSPC), November 15-16 2022, Hachioji (Japan).
3. **Apriandanu, D. O. B.**, Nomura, S., Nakayama, S., Shibata, K. & Amano, F., Oral presentation, Ti-doped Fe_2O_3 Photoanodes on Three-Dimensional Titanium Microfiber

Felt Substrate for Photoelectrochemical Oxygen Evolution, 73rd Annual Meeting of the International Society of Electrochemistry (ISE-73), September 12-16 2022, Virtual.

4. **Apriandanu, D. O. B.**, & Amano, F., Poster presentation, Role of additional annealing in argon on photoelectrochemical properties of Ti-doped Fe_2O_3 electrodes, The 9th Tokyo Conference on Advanced Catalytic Science and Technology (TOCAT9), July 24-29 2022, Hybrids (Fukouka, Japan).

5. **Apriandanu, D. O. B.**, & Amano, F., Oral presentation, Effect of two-step annealing on photoelectrochemical properties of hydrothermally prepared Fe_2O_3 on titanium felt substrates, The 18th Japan-Korea Symposium on Catalysis (18JKSC), November 23-25 2021, Virtual.